Cortis, Michael (2016) Numerical modelling of braided fibres for reinforced concrete. PhD thesis.

http://theses.gla.ac.uk/7763/

Numerical Modelling of Braided Fibres for Reinforced Concrete

Michael Cortis

Infrastructure and Environment Research Division
School of Engineering

Submitted in fulfilment of the requirements for the
Degree of Doctor of Philosophy

at the
UNIVERSITY OF GLASGOW

November 2016

Deceleration

I declare that this thesis is a record of the original work carried out by myself under the supervision of Professor Chris Pearce and Dr. Lukasz Kaczmarczyk in the School Engineering at the University of Glasgow, United Kingdom, during the period of September 2011 to November 2015. The copyright of this thesis belongs to the author under the terms of the United Kingdom Copyright acts. Due acknowledgement must always be made of the use of any material contained in, or derived from, this thesis. The thesis has not been presented elsewhere in consideration for a higher degree.

Michael Cortis

INVESTING IN YOUR FUTURE
EUROPEAN SOCIAL FUND
MALTA2007-2013

The research work disclosed in this publication is partially funded by the Strategic Educational Pathways Scholarship (Malta). This scholarship is part-financed by the European Union – European Social Fund (ESF) under Operational Programme II – Cohesion Policy 2007-2013, “Empowering People for More Jobs and a Better Quality of Life”.

Operational Programme II – Cohesion Policy 2007-2013
Empowering People for More Jobs and a Better Quality of Life
Scholarships part-financed by the European Union
European Social Fund (ESF)
Co-financing rate: 85% EU Funds; 15% National Funds

Investing in your future

Abstract

Fire has been always a major concern for designers of steel and concrete structures. Designing fire-resistant structural elements is not an easy task due to several limitations such as the lack of fire-resistant construction materials. Concrete reinforcement cover and external insulation are the most commonly adopted systems to protect concrete and steel from overheating, while spalling of concrete is minimised by using HPFRC instead of standard concrete. Although these methodologies work very well for low rise concrete structures, this is not the case for high-rise and inaccessible buildings where fire loading is much longer. Fire can permanently damage structures that cost a lot of money. This is unsafe and can lead to loss of life.

In this research, the author proposes a new type of main reinforcement for concrete structures which can provide better fire-resistance than steel or FRP re-bars. This consists of continuous braided fibre rope, generally made from fire-resistant materials such as carbon or glass fibre. These fibres have excellent tensile strengths, sometimes in excess of ten times greater than steel. In addition to fire-resistance, these ropes can produce lighter and corrosive resistant structures. Avoiding the use of expensive resin binders, fibres are easily bound together using braiding techniques, ensuring that tensile stress is evenly distributed throughout the reinforcement. In order to consider braided ropes as a form of reinforcement it is first necessary to establish the mechanical performance at room temperature and investigate the pull-out resistance for both unribbed and ribbed ropes. Ribbing of ropes was achieved by braiding the rope over a series of glass beads. Adhesion between the rope and concrete was drastically improved due to ribbing, and further improved by pre-stressing ropes and reducing the slacked fibres. Two types of material have been considered for the ropes: carbon and aramid.

An implicit finite element approach is proposed to model braided fibres using Total Lagrangian formulation, based on the theory of small strains and large rotations. Modelling tows and strands as elastic transversely isotropic materials was a good assumption when stiff and brittle fibres such as carbon and glass fibres are considered. The rope-to-concrete and strand-to-strand bond interaction/adhesion was numerically simulated using newly proposed hierarchical higher order interface elements. Elastic and linear damage cohesive models were used effectively to simulate non-penetrative 'free' sliding interaction between strands, and the adhesion between ropes and concrete respectively. Numerical simulation showed similar de-bonding features when compared with experimental pull-out results of braided ribbed rope reinforced concrete.

Acknowledgement

I would like to thank my supervisors, Prof Chris Pearce and Dr Lukasz Kaczmarczyk for their continuous support. Thanks also go to my scholarship scheme committee, STEPS, whom awarded me a scholarship, which is 85% funded by the European Social Funds and 15% funded by the Maltese Government. Also, I would like to acknowledge LaTeX texmaker to be able to typeset this report, MoFEM team at Glasgow University and Argonne National Laboratory to be able to used MOAB and PETSc. Last, but not least, a big thanks to my family, whom always supported me to achieve what I aimed for.

Abbreviations

AR	Alkali resistant
BCR	Braided composite rods
CC	Concrete canvas
CFCC	Carbon fibre composite cables
CFRC	Carbon fibre reinforced cement
CFRP	Carbon fibre reinforced polymer
CMC	Ceramic matrix composite
FE	Finite Element
FEM	Finite Element Method
FRC	Fibre reinforced concrete
FRP	Fibre reinforced polymer
GFRP	Glass fibre reinforced polymer
GGBFS	Ground granulated blast furnace slag
GTT	Glass transient temperature
HDPE	High density polyethylene
HESFRC	High early steel fibre reinforced concrete
HO	Higher order
HPC	High-performance cement
HPFRC	High performance fibre reinforced concrete
KSP	Krylov scalable linear equation solver
LCFRC	Long carbon fibre reinforced concrete
NFRCM	Natural fibre reinforced cementitious matrices
PAN	Poly-acrylonitrite-based (carbon fibres)
PE	Polyethylene
PO	Polynomial order
PP	Polypropylene
PVA	Polyvinyl alcohol
RBFR	Ribbed braided fibre reinforcement

SFRC	Steel fibre reinforced concrete
T12	commercial name for a double braid twelve strand round sinnet
TL	Total Lagrangian
TRC	Textile reinforced concrete
UCAS	Unresin carbon-fibres assembly system
UCCF	Unresin continuous carbon fibre
UHP-HFRC	Ultra high performance hybrid fibre reinforced concrete
UHPFRCC	Ultra high performance fibre reinforced cementitious composite

Terminology

braiding	a group strands inter-winded using different pattern and follow a single axis of direction
plait	similar to braid refers to the inter-winding of 3 or more strands
sinnet	braided cordage in flat round or square form made from 3 or more strands
strand	a group straight or twisted yarns
weaving	a group strands inter-winded using different pattern and follow 2 or 3 axis of direction
yarn	a group of straight tows

Cubit Terminology

blockset	a set which contains geometrical entities
edge	a entity representing a path between 2 end nodes and passes through mid-nodes if exists in a FE mesh
meshset	a set which contains a set of tetrahedrons
node	a entity representing a point in a FE mesh
nodeset	a set which contains a set of nodes
sideset	a set which contains a set of triangles

Operators

$\|x\|$	L2 norm of x
$\hat{x}$	normalized vector of x
$\bar{x}$	mean value of x
$\vec{x}$	vector of x
d, ∂, δ	differential operators
Δx	range of x
∇x	gradient of x

Symbols

α	constant variable
β	contribution damage factor between Modes I, II and III
γ, α, β	index notation of corners, edges and faces **DOF**s
ε	six-component strain vector
θ	angle
κ	exponent factor
μ	coefficient of friction
ν_p	Poisson's ratio in the transverse plane of fibres
ν_{pz}	Poisson's ratio between fibre principal axis and transverse plane
ξ, η, ζ	normalized coordinates
ϕ	nominal diameter of reinforcement
σ	six-component stress vector
$\bar{\sigma}_c$	effective ultimate tensile strength
τ_r	bond stress at failure by slipping

ω	Gauss quadrature weights or damage fraction
Φ	shape function matrix
$\mathbf{\Psi}$	potential field

$\vec{a}$	axis of rotation
e	error of solution
$\vec{f}$	fibre directions
$\mathbf{f}_{el}^{int}$	element internal force
f_t	maximum traction force of interface
g_i	displacement of interface damage initialization
$\vec{p}$	principal axis of transverse isotropy
p	polynomial order
$\mathbf{t}_{loc}$	local traction
$\mathbf{u}$	displacement
u_{n,t_1,t_2}	local interface gap displacement in Mode I, II and III
$u_{loc,glob}$	local/global interface gap opening
$\mathbf{v}$	velocity
$\mathbf{x}$	current coordinates

A, $\bar{A}$	area, effective cross sectional area
$\mathbf{C}$	compliance matrix
$\mathbf{D}_{loc}$	local elastic stiffness matrix
$\mathbf{E}$	Green strain tensor
E_o	interface element penalty stiffness
E_p	stiffness in the transverse plane of fibres
E_z	stiffness in the principal axis of fibres
F, $\bar{F}_c$	force, effective critical force
$\mathbf{F}$	deformation gradient tensor
$\mathbf{G}_{f,I}$	Griffth fracture energy in Mode I

G_z	shear modulus between fibre principal axis and transverse plane
$\mathbf{I}$	identity matrix
I, II, III	normal and two tangential modes of fracture
J	Jacobian
$\mathbf{K}_{el}$	element stiffness matrix
L	Legendre Polynomials
N	number of degrees of freedom
N	local shape functions
$\mathbf{R}$	rotation matrix
$\mathbf{S}$	2^nd Piola Kirchhoff stress tensor
$\mathbf{T}_\sigma$, $\mathbf{T}_\varepsilon$	stress/strain transformation matrix
W	virtual work
$\mathbf{X}$	reference coordinates

Contents

List of Figures

List of Tables

Chapter 1

Introduction

1.1 Motivation

Structural stability during fire incidents is extremely important to preserve occupants' lives, reduce the risk to firefighters and reduce financial losses. It is important that the duration of fire is minimised. In cases such as high-rise and confined buildings, the containment of a fire can be very difficult and permanently damages the structure.

A recent example is a fire in Krasnoyarsk (south-western Siberia), involving a newly built 25 storey monolithic concrete high-rise building. A fire was triggered during maintenance work on a balcony and propagated to the above lying balconies[205]. Although the building had appropriate fire access[190], using 16 fire engines, three helicopters and about 100 firefighters, it took approximately 4 hours to get the fire under control. Due to structural fire insulation and compartmentalisation, only the fabric of the building was damaged, but still resulted in an approximate repair bill of £605,000[206]. This case could have been worse if the building was taller and if a fire was initiated further inside the building.

When concrete structures are exposed to elevated temperatures, permanent and large deformation can occur due to excessive yielding of steel reinforcement and loss of bond strength with concrete. Concrete's strength and stiffness is also reduced. Spalling can be mitigated by using propylene fibres in the concrete mix. Propylene fibres melt at around 130°C, thereby forming a series of cavities through which built up water pressure in concrete can be released. Heating of steel reinforcement is normally reduced by providing adequate concrete cover and overall structural insulation. However, these additional measures add extra weight to the structure, while the installation of insulation inflates the overall cost of construction.

1.1.1 Aims and objectives

The principle aim of this research is to find an alternative concrete reinforcement system that could be fire-resistant, and to study its mechanical behaviour and bond adhesion with concrete. The first objective of this research is to develop a new reinforcement system made from heat resistant materials, which provides sufficient adhesion to concrete and can be used as main reinforcement in concrete structures. A pre-stressed ribbed braided fibre reinforcement RBFR system was developed as discussed Section 1.2 and experimentally tested using a pull-out test to determine the overall bond adhesion with concrete. The second objective of this research was to develop a numerical tool based on a parallelised finite element method to simulate and understand the overall mechanical behaviour of RBFR system and its interaction with concrete. This consists of developing a methodology to mesh braided geometries using an efficient algorithms, to model fibrous materials using an elastic transversely isotropic constitutive model, to simplify the bond interaction between braided strands by using interface elements instead of contact mechanics (i.e. reduce computational cost), and to accurately simulate the bond interaction between braided ropes and concrete by developing hierarchical higher order interface elements.

1.2 The motivation for braided fibre reinforcement

Fibre reinforced material has been used for thousands of years. Adobe, which is made from a mixture of natural straws and mud/clay, has been used for centuries by humans to build structures and produce artefacts. Since the Greek and Roman Empires, cementitious materials have been used to produce stronger, water and crack resistant products. By contrast, the use of steel as reinforcement to cementitious products was not invented until the nineteenth century. This has revolutionised the construction industry with stronger buildings in various shapes and forms.

In the late nineteenth and beginning twentieth century, we saw the introduction of asbestos and glass fibres as reinforcement of cementitious products. While it was common to add chopped fibres to concrete to enhance its properties, it was not until a few decades ago that continuous fibre reinforced polymers were introduced to produce an alternative reinforcement for steel, providing corrosion resistant, lighter and stronger structural components. With the introduction of polymer matrices, fire-resistance resurfaced as an issue, since commercially viable polymers have a low glass transition temperature and this directly affects the structural integrity of the whole reinforced system[114;113].

The motivation behind this research was to produce and investigate, both experimentally and numerically, a braided fibre reinforcement system for concrete as an alternative to steel reinforcement that can be further studied for its potential fire endurance. Steel reinforcement in a typical 600×300 mm un-insulated concrete section with 50mm of concrete cover can reach temperatures of 300°C in a 90 minute standard fire (Figure 1-1(b)) with an elastic modulus reduction of 20%-28%[101]. This results in excessive yielding of steel, formation of plastic hinges and permanent deformation beyond the serviceable limit state. Fibrous materials such as carbon and glass fibres were considered in this research as an alternative to steel reinforcement due to their heat and corrosion[i] resistance and high tensile strength.

Fibre reinforced polymer (FRP) rebars, available on the market, are used in marine environments and bridge construction. A case study shows that FRP rebars are 60% more expensive than steel, but the construction of bridge decking was 56% cheaper than conventional steel reinforced decking, with better endurance and less

---

[i] only alkaline resistant glass fibres are suitable in concrete environment

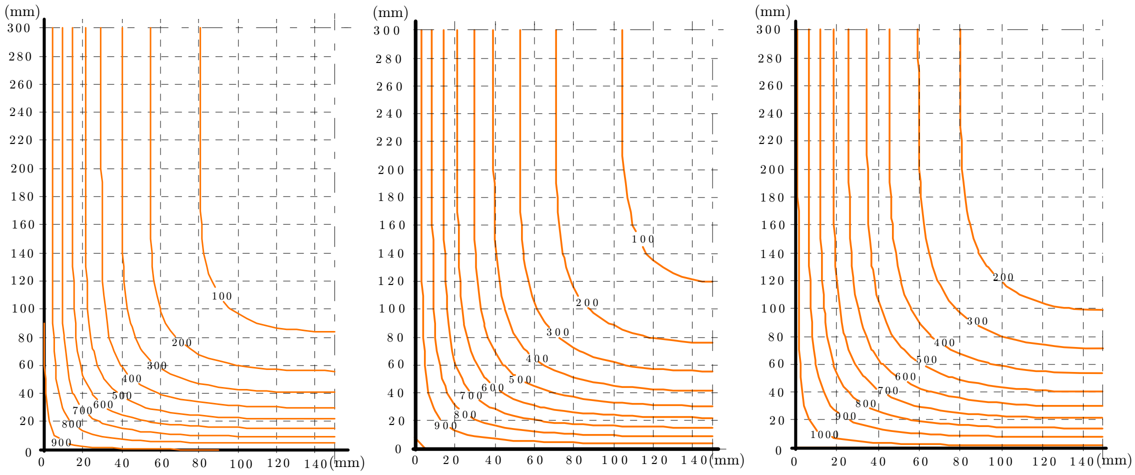

(a) R60 (b) R90 (c) R120

Figure 1-1: Temperature contours lines for a quarter of a 600x300mm concrete section (60, 90 and 120 minutes standard fire exposure)[101]

maintenance, providing long-term benefits and savings[29]. Although such FRP reinforced concrete structures are corrosion resistant, at elevated temperatures the bond strength between FRP bars and concrete is weakened by 80-90% at temperatures around 200°C[114;113] due to the low glass transition temperature (GTT) of the polymeric resins used to produce FRP bars.

Developing heat resistant fibre reinforcement was one of the major challenges of this research. Heat resistant polymeric resins were considered, but due to their manufacturing cost this idea was discarded. Another option was ceramic based matrices, but due to the lack of expertise and necessary equipment and funding, this idea was unworkable and remains open for investigation. Finally, the old art of weaving, stitching, knitting and braiding inspired the mechanical binding of a bundle of fibres to form forming lengths of ropes. This cheap solution led to another challenge in providing a good adhesion between the ropes (used as tensile reinforcement) and concrete, which was provided by braiding the rope over a series of fire-resistant beads forming external ribbing effects. It was important for ropes to be fully embedded and beyond their non-linear elastic stage before they were cast in concrete. Pre-stressing of ropes up to the elastic region was necessary to avoid largely irreversible deformations and, consequently, severe concrete cracking.

Experiments were conducted to examine the feasibility of ribbed braided fibre reinforcement, while a finite element numerical modelling framework was developed to model the mechanical behaviour of braided fibres and their interaction with concrete and other materials.

1.3 Outline of thesis

A general literature review of different types of fibre reinforced concrete will now follow, which later focuses on several types of continuous fibre reinforced concrete and how the idea of un-resin ribbed braided fibre reinforcement emerged. The literature review also provides a general overview of the mechanics of fibres and braided sections, and recent numerical modelling techniques for woven textiles and braided fibres. Physical and numerical experiments were conducted to assess the feasibility of ribbed braided fibre as concrete reinforcement and to develop a numerical tool that simulates the kinematics of solo/cast in concrete braided fibres. Chapter 3 on the experimental work discusses the methodology adopted and presents results of pull-out tests of carbon and aramid fibre ropes (later ribbed with glass beads) embedded in concrete, before making recommendations. The last part of this research was divided into three main chapters. Chapter 4 introduces the use of higher order finite interface elements that are refined hierarchically (increasing computational efficiency) and introduces cohesive damage models for the concrete-fibre interface. Chapter 5 focuses on the methodology adapted to conduct finite element modelling of braided fibres. It starts by explaining how braided geometries were generated and meshed, and how the potential field equation was solved to determine the fibre directions and implement transverse isotropy for individual strands. The discussion continues to focus on how pre-defined interface elements were used to describe the contact behaviour between strands and demonstrates the importance of using geometric non-linearity when modelling braiding fibres. After studying the mechanics of braided geometries at the mesoscale in Chapter 5, the pull-out behaviour of ribbed braided fibre embedded in concrete was simulated. Chapter 6 proposes a simplified version of modelling braided fibres embedded in concrete. This thesis concludes with a summary of the main topics of study, further remarks on the investigation, and suggestions for future work.

Chapter 2

Literature review

Natural evolution has always found solutions to all sorts of mechanical challenges. For millennia, natural fibres have been grown as rigid and flexible matter to resist tensile actions. Mankind exploited natural fibres to manufacture ingenious products such as lashings, ropes, textiles and adobe. Adobe is a mixture of mud and natural fibres and is considered the first manmade composite material, able to resist compressive forces and shrinkage.

Fibre reinforced concrete, similar to adobe, uses fibres to create a rigid composite strong enough to be used as construction material. Invented during the Victorian age by using steel fibres (wires), aggregate and cementitious matrix, reinforced concrete has revolutionised the construction industry. During the twentieth century, new, stronger, lighter, corrosion and heat resistant fibre materials were invented to replace steel reinforcement. Among different types of composites such as fibre reinforced polymers (FRP) and ceramic matrix composites (CMC), fibre reinforced concrete (FRC) was developed to have special material characteristics discussed later in this chapter.

This chapter is divided into three main parts. In the first section short and long fibre reinforced concrete are discussed, and how the idea of ribbed braided fibre rope system was proposed. The second section focuses on the understanding of the bond mechanism between steel reinforcement and concrete, followed by a comprehensive literature review on the numerical modelling of reinforced concrete. Furthermore, it discusses the development of damage modelling in the FEM, highlighting important aspects required to model ribbed braided fibre reinforced RBFR concrete. The last section focuses on the mechanics of fibre composites and braided fibres, including recent developments on the numerical modelling of braided fibres.

2.1 Fibre reinforced concrete

Fibres used to reinforce concrete exist in various forms, materials and profiles. Different types of fibres contribute distinctively to the mechanics of concrete structures. The aim of this section is to highlight the evolution of different types of fibre reinforced concrete structures, and consequently ribbed braided fibre reinforcement.

2.1.1 Different types of fibre reinforcement

Fibres used in reinforced concrete exist in various forms and materials. Strong fibres able to provide good adhesion with cementitious matrices can increase the tensile strength of concrete, while other properties of fibres can enhance other physical properties of concrete.

Fibre reinforced concrete FRC was first invented by Ludwig Hatschek around 1890. After 7 years of experimenting with different mixtures of cellulose, asbestos fibre, cement and water, he optimised the mix. By pressing it through a papermaking machine, he produced a viable fibre cement panel. This invention was later patented under the name of Eternit[133]. Eternit became one of the most important construction materials worldwide and was widely used as roofing and cladding material (Figure 2-1). This material was very well known for its fire-resistance, water tightness, rot resistance, lightness, malleability and ease of installation. Awareness of the danger of asbestos soon emerged during the 1970s, and consequently, PVA fibres have long since replaced asbestos fibres[133].

Figure 2-1: Asbestos cement roof cladding

Figure 2-2: SFRC after exposed to 800°C[199]

While Eternit was invented for non-load bearing components, the introduction of high-performance cement (HPC)(later evolved into high-performance fibre reinforced concrete (HPFRC)) enhanced the material properties of concrete. The first HPC was produced with steel fibres to increase the durability and crack resistance of concrete. This was later used by Romualdi and Batson in the United States around 1988 to construct bridges with longer life expectancy[169]. A few years later Mori proposed an inclusion model to determine the crack arrest in HPC[145]. Meanwhile, in ex-USSR, glass fibre reinforced cement was invented by Mr Biryukovich and his sons[32]. Despite the outstanding properties of glass FRC, it was discovered that ordinary glass fibre was not fit for purpose, as it deteriorates in alkali environments produced by hydrated Portland cement[98]. New attempts to use synthetic fibres such as nylon and polypropylene as a replacement of glass fibres initially failed and produced an inferior HPFRC compared to steel fibre reinforced cement (SFRC)[144;75]. This was later improved by using high tensile strength polypropylene fibres[147] to produce durable concrete, adequate for the manufacture of corrugated roofing, precast flower beds, and water tanks[119].

Steel fibre reinforced concrete

The popularity of steel fibre reinforced concrete (SFRC) rapidly increased among researcher and engineers. The versatility of steel fibres in the market made it possible to produce concrete strong in bending, shear and torsion[138]. At a micro-level, the bond adhesion between individual fibres and concrete was examined, while at a meso-level the overall crack patterns of SFRC were studied[28]. It was discovered that bond strength is influenced by the speed of pull-out testing[15] and has a direct influence on the long-term performance of HPFRC. The bond strength can be doubled by optimising the sand ratio in mortar[95]. On similar criteria, optimising the right amount of steel fibre in concrete can produce C35 concrete after just 24 hours of curing time, commercially denoted as high early-strength steel fibre reinforced concrete HESFRC[148]. This is of great advantage when high strength concrete is required at an early stage of the construction. When HPFRC is fully cured, compressive strength can reach up to 90-115MPa with just 1% fibres by volume in normal and lightweight concrete[14]. Moreover, fibre orientation influences the anisotropy of the concrete and the post-cracking process of ultra high-performance fibre reinforced cementitious composite UHPFRCC[112]. Using a cocktail of micro (8μm and macro (12-31μm) steel fibres (having different shapes and geometries) it is possible to produce a hybrid UHPFRCC (UHP-HFRC) that has the advantage of multiple cracking behaviours and strain hardening[158]. Some theoretical studies on the energy changes in concrete contributed to the improvement of the tensile strain capacity of HPFRC[207].

Various studies were conducted to examine the mechanical behaviour of SFRC when exposed to fire or high/extreme temperatures. Early studies have shown that the compressive strength of both plain and steel fibre reinforced concrete weakens drastically at temperatures of around 800°C (Figure 2-2)[162;64]. Corrugated and deformed steel fibres SFRC are more resilient at temperatures of around 1000°C[125] than plain fibres. Although the addition of polypropylene (PP) fibres to the SFRC did not improve the strength of concrete[115;199], it was beneficial in preventing explosive spalling generated from water pressure build up in concrete. As temperature rises, PP fibres dissolve, leaving micro pores from which water pressure can be released[9;191]. PP is one example of fibres being used to improve the performance of concrete at elevated temperatures. The same spalling resistance was observed in concrete columns containing PP fibres and suggested that steel reinforcement can be reduced[168], providing cheaper, lighter and fire-resistant concrete components. Fire-resistant fibre reinforced concrete can be achieved by adding ground granulated blast furnace slag (GGBFS) to concrete[71] and produces commercially viable concrete products.

One of the main disadvantages of SFRC is the corrosion of the fibres. Corrosion can be prevented by adding inhibitor admixtures[148], using the protection system[27] or by galvanizing or coating steel fibres with corrosion resistant material[160]. In the meantime, steel fibres are beneficial as they produce a passive corrosion resistance to the main reinforcement[39]. In certain cases, steel fibres can be replaced by polyethene fibres PE which are ideal for repairing exterior damages of concrete structures due to their inertness[118].

Carbon fibre reinforced concrete

Carbon fibres are stronger, lighter, heat resistant and more cheaper than steel (comparing strength to volume). After initial studies of carbon fibre reinforced concrete (CFRC)[7], it became increasingly popular and commercially viable towards the end of the twentieth century. This brought radical improvement in CFRC material properties by using a water reducer and accelerating admixture[221]. The addition of a latex solution and use of hot water in the curing process enhanced the flexural resistance of concrete by 40% and its toughness by 100%[124]. Moreover, the addition of silica fumes increased the abrasion resistance of CFRC[187].

The introduction of poly-acrylonitrile-based (PAN) carbon fibres in CFRC was revolutionary, able to provide better tensile/flexural strength[209] and higher damping ratio[73] to concrete. Longer chopped carbon fibres (around 100mm) were also used to produce reinforced concrete panels LCFRC and increase its blast spalling resistance[201]. The performance of CFRC at elevated temperatures was also studied. Reductions of 60%

in compressive strength and 30% in flexural strength were observed when subjected to temperatures of around 800°C[202]. Unfortunately, the literature is quite limited and further research is therefore highly recommended on this topic.

In the following section, the possibility of using continuous fibres to reinforce, and eventually replace steel rebars in concrete structures is discussed.

Figure 2-3: Scattered carbon fibres for CFRC

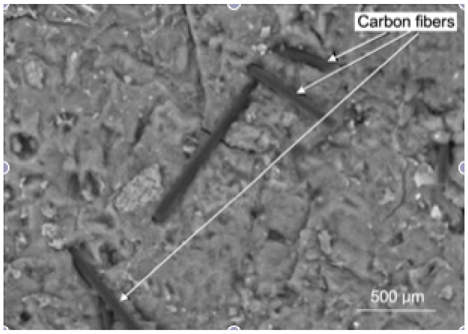

Figure 2-4: Scattered carbon fibres embedded in concrete[202]

2.1.2 Continuous fibre reinforcement

While the purpose of short fibres is to improve the mechanical and non-mechanical properties of concrete, long continuous fibres are mainly used to mechanically reinforce concrete structures in tension and shear. This represents an alternative solution for steel reinforcement that benefits from the advantageous properties of fibre products, such as weight to strength ratio, flexibility and thermal resistance (specific types of fibres).

Continuous fibres exist in various forms. The most common type of continuous fibre reinforcement is fibre reinforced polymer (FRP) rebars, usually used as a substitute for steel reinforcement. They provide lighter, corrosion resistant concrete structures. Similarly, carbon fibre composite cables are used as a pre-stress reinforcement in concrete structures. A less popular type is braided FRP rods, studied as an alternative reinforcement to continuous FRP rods. While all of these make use of polymeric resin binders, the use of un-resin (carbon) continuous fibre (UCCF) and textile reinforced concrete (TRC) was studied by researchers as a possible reinforcement for concrete structures. The main disadvantage of this kind of reinforcement is the brittleness of commonly used materials such as carbon, glass and Kevlar fibres. Concrete structures will fail without any visible warning to the building users. It is thought that un-resin braided fibre reinforcement as proposed in this thesis can absorb more energy than the existing systems. A hybrid of carbon/glass/Kevlar fibres and steel wires may solve this problem and is worth investigating further.

Carbon fibre composite cables and rods

Carbon fibre composite cables (CFCC) manufactured by Tokyo Rope Company Ltd were the first type of continuous fibre reinforcement invented[1]. This was an early form of FRP rods, which are corrosion resistant, able to withstand marine and salty environments, and therefore ideal for use in bridges and other long-life structures. CFCC were first used as pre-stressing tendons (Figure 2-5), requiring the bond strength between the cables and concrete[135] to design pre-stressed concrete structures. Later work showed how similarly carbon fibre reinforced polymer (CFRP) rebars can be used as pre-stressed tendons. This was made possible by improving the the bond adhesion using sand-covered and spiral glued modified FRP bars[47]. The same research identified that the bond failure was very brittle and challenged manufactures to produce better FRP rebars.

Although commercial FRP rods provide sufficient bond strength at room temperature, this is not the case for elevated temperatures. Research shows that the bond strength can be reduced by 80-90% at around 250°C[114]. Due to the low glass transition temperature (GTT) of the polymer binder[69], the matrix liquefies and the structural integrity of the fibres and bond adhesion is quickly lost[113].

Braided composite rods

As an alternative to CFCC and FRP rods, braided FRP rods were developed with the aim of providing better pull-out strength when embedded in concrete. Studies showed that partial pre-tensioned braided FRP achieved a better modulus of elasticity and bond strength[154] compared to continuous FRP rods. Like braided ropes (see 2.3.1.3), the mechanical properties of braided composite rods (BCR) also depend on the type and dimensions of the braiding profile itself. Research shows that the braiding angle is the second most important parameter that determines the overall strength and modulus of BCR[195]. As a matter of fact, BCR with an optimised braiding angle made from 77% E-glass and 23% carbon fibre yields higher tensile strengths than 100% carbon BCR (Figure 2-6)[76;78;77]. Although straight carbon fibres are stronger than E-glass, the justification behind this is that carbon fibres are more brittle, especially when embedded in a brittle matrix. Due to lack of research, BCR are not yet available on the market until further research is conducted to determine the commercial and mechanical viability of such a product.

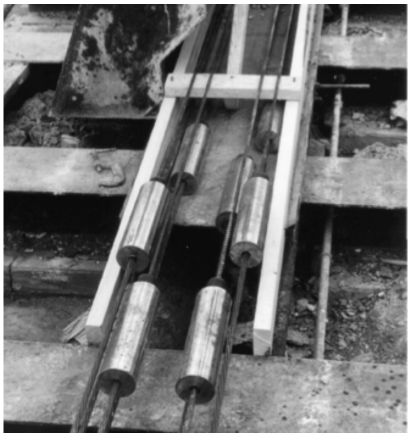

Figure 2-5: CFCC and typical anchorage for pre-stressing[197]

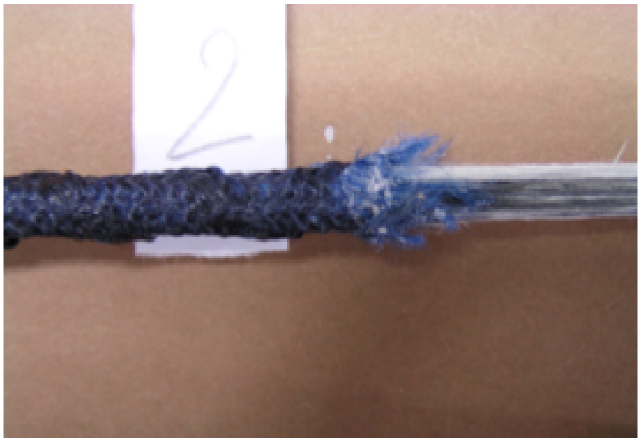

Figure 2-6: Continuous braided rods, 77% E-glass and 23% carbon fibre[76]

Un-resin continuous carbon fibres

In order to circumvent the poor performance of polymers used in FRPs at elevated temperatures, one can use un-resin continuous carbon fibres (UCCF) as invented by researchers at Kyushu University, Japan. UCCF are easy to anchor and shape, and are more cheaply produced than FRP rods. Using UCCF reinforcement, studies have shown that concrete beams can achieve up to 80% of the flexural strength compared to an equivalent steel reinforced beam. One of the main reasons for this is that only 50% of the carbon fibres were contributing to flexural resistance[57] and reducing the slackness of fibres increased this contribution up to 67%[153].

Another drawback was the lack of good adhesion to concrete. A grid skeleton system (UCAS) was proposed to mitigate this problem. This consisted of gluing UCCF cables to a steel rib cage using polymeric resins[152], which ultimately improved the bond strength by ten times compared to a non-grid system and provided enough flexural resistance to be a substitute for steel reinforcement[56;184]. Unfortunately, the performance of UCAS at elevated temperature is not yet known and thus requires further investigation.

The following literature review focuses on the bond behaviour of carbon fibres embedded in concrete. The bond interaction between fibres and concrete can be studied at both micro and meso-level. Several attempts were made to improve the lack of microscopic adhesion with concrete and carbon fibres. Two successful methodologies were to treat the carbon fibre's surface (known as silane-treatment) and/or add silica fume/organic polymer to the cementitious matrix[12]. Another possibility was the use of air entraining concrete to create cavities which act as interlocking mechanisms on the fibres[108].

It is important to note that advanced studies, such as the micro-mechanical analysis and the development of design models, started to appear few years after the invention of the FRC by Biryukovich and sons[32], and was later evolved by Briggs et. al.[33]. One of the most important findings was that FRC with 3-5% unidirectional carbon fibre CFRC can increase its relative tensile strength up to 7.8 - 13.7MPa[3]. There is less research done on the micro-thermo-mechanical bond behaviour of carbon fibres embedded in concrete.

Textile reinforced concrete

Another type of continuous fibre reinforcement is textile reinforced concrete TRC. The practical use of TRC was highlighted by the invention of Concrete Canvas (CC), which is a flexible form of cement-impregnated fabric, capable of hardening into any given shape and forming a thin durable waterproof fire-resistant concrete shell. This could be used to produce inflatable emergency shelters (Figure 2-7) that are easily transported and erected in a short period of time[80]. Understanding the mechanical behaviour of TRC composites is important to the development and construction of TRC structures.

TRC is considered to be a heterogeneous composite material with a complex microstructural layout and, similarly to CFRC, it suffers from a lack of adhesion between concrete and fibres. Models describing the micro/mesoscopic mechanics of the bond adhesion[165] were useful in determining the bond strength between single filaments and concrete[86]. These models were used in a finite element parametric study of a TRC in direct tension and were able to predict the stress distribution in the composite and determine the ultimate mean stress and strains of TRC[85]. It was also determined that bond strength remains constant during ageing of TRC[36], preserving durability and structural integrity. Another advantage of TRC was its resistance to impact loading compared to HPFRC[122] and being able to produce impact-resistant concrete panels[159].

Box girders can also be constructed by gluing TRC panels, braided with fibres throughout (Figure 2-8) and coated with cementitious matrix. These box girders have good flexural resistance, but are weak in shear[161]. A better form of TRC panels can be made from a hybrid composite of GFRP and TRC providing 3.75 times more tensile strength than mono TRC panels[70]. CC, which is a form of TRC, can be also made by 3D spacer fabric which yields better tensile strength than conventional TRC CC[84]. TRC can also be used to reinforce concrete structures in bending[179], and more effectively as wrapping system to enhance the shear capacity of concrete columns[156] and beams[189]. However this is not as good as external CFRP plate flexural reinforcement system[188].

TRC can also be manufactured using alkali-resistant (AR) glass fibres[36] or natural fibres such as flax, hemp, jute, sisal, and coir fibres which are 100% organic and

Figure 2-7: Concrete canvas CC shelter[80]

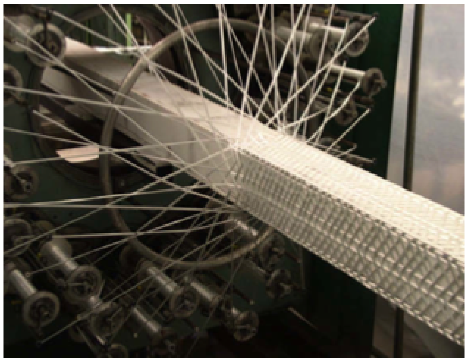

Figure 2-8: 3D braid over a beam girder made from TRC panels[161]

biodegradable. Natural fibre reinforced cementitious matrices (NFRCM) can gain tensile strengths of up to 60MPa, but with a relatively low modulus of elasticity[46].

This literature review demonstrates that raw continuous fibres are a potential substitute for steel reinforcement in the manufacture of corrosion and fire-resistant concrete structures. Based on existing knowledge, this thesis proposes a new ribbed braided fibre rope system which was studied both numerically and experimentally. Hence it was necessary to obtain a good level of knowledge of the fibres and braiding mechanics as discussed in the following section.

2.2 Steel reinforced concrete

While fibre reinforced concrete is becoming more popular in the construction industry, steel reinforced concrete has remained the most popular construction material since its invention. Studying the mechanical interaction between steel reinforcement and concrete, and thereby gain an understanding of how stresses are transferred from one material to another, is important to investigate and optimise the mechanical behaviour of the (RBFR) system proposed in this thesis. A review of various numerical techniques adopted to simulate the bond behaviour between steel and concrete was therefore carried out. The final part of this section is dedicated to the understanding of fracture mechanics, how the fracture is modelled in the FEM, and how interface elements are enhanced and enriched to accurately simulate fracture and de-bonding.

2.2.1 Bond mechanism between steel and concrete

Steel reinforced concrete is a cheap composite material heavily used in the construction industry. It is able to sustain and transfer tensile and compressive stresses through the structure. Like other composites, stresses are transferred between the concrete and steel reinforcement through a suitable interface. The introduction of steel rebars was a significant invention in the improvement of this bond adhesion[42] through lateral and inclined lugs which are formed on the surface of cold or hot rolled steel bars. Studies have shown that the bond strength is proportional to the lug height and lug frequency ratio[194]; the bond failure can change from concrete splitting to bond slipping as the lug height is reduced and lug frequency is increased. In the same study, it was recommended that the minimum height of the lugs is 0.03 × bar diameter, while the spacing of the lugs should be about 0.3 × bar diameter. Additionally, increasing the lug inclination to the bar axis results in minor improvement to the bond characteristic, but significant increase in the bendability of the steel bar[194].

Concrete confinement is the first major contributor to the pull-out strength of rebars embedded in concrete[134]. Goto[79] shows that concrete experience internal, secondary and longitudinal cracks during the pull-out of embedded steel reinforcement. During pull-out, zones of compressive and tensile stresses concentrate on the front and back of every lug respectively, where internal cracks propagate without reaching the concrete surface. Eventually, concrete around the reinforcement deforms and tightens in the form of a comb-like teeth patterns which increase the frictional resistance between steel and concrete (see Figure 2-9). At frequent intervals along the concrete, internal primary transversal cracks are propagated along the concrete and up to its surface.

Monotonically loaded pull-out tests conducted by Rehm were insufficient to discover at which stage fracture in concrete is initiated with irreversible pull-out deformation[164]. Instead, cyclic pull-out loading with limited reversal loading was introduced by Giuriani[74] to study the bond mechanism in terms of micro-cracking and concrete

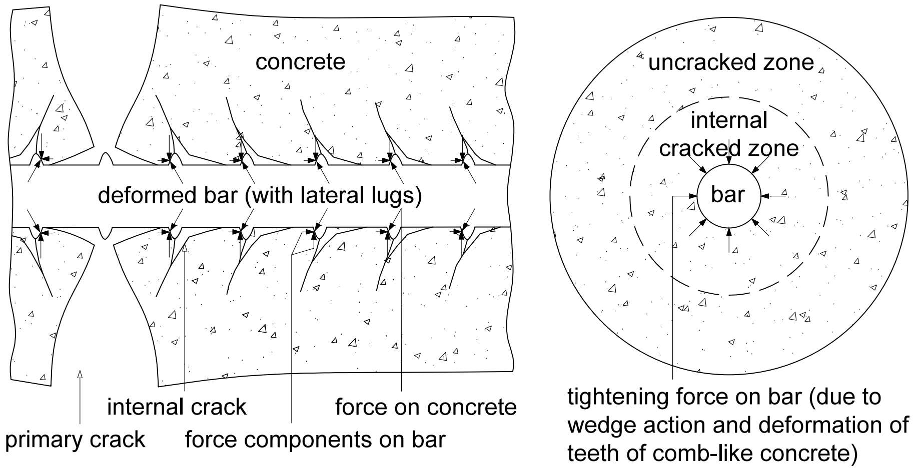

Figure 2-9: Schematic diagram of fracture in concrete during pullout of steel rebar[79]

crushing. Various parameters such as concrete strength, concrete cover, bar spacing and confinement utilising stirrups have been used to study their influence on the pull-out bond strength of reinforcement from concrete[141], while empirical models were proposed to compute the bond stresses during bond cracking, design stage and ultimate loading condition[117;130].

The understanding of the bond mechanism between steel and concrete is essential in numerical modelling of reinforced concrete. The first review of the existing knowledge on the bond behaviour between steel and concrete was reported by the American Concrete Institute Committee number 408 in the year 1966[67]. This report defines the bond stress as either the stress per unit area of the nominal surface of the steel bar, or by the rate of change of stress in the steel bar. The discussion now turns to the bond failure of plain and ribbed bars. For plain bars, bond adhesion is provided by chemical adhesion which concrete provides onto the bar's surface. If we consider a pull-out of a plain bar from concrete (Figure 2-10(a)), at first, the top part of the bar does not contribute to the pull-out resistance (Figure 2-10(b-d)). As pull-out progresses, adhesion resistance moves toward the top part of the bar (Figure 2-10(e)) until it is lost, leaving only frictional resistance against the pull-out action (Figure 2-10(f-h))[146]. Unlike hot rolled bars, cold rolled plain steel bars tend to have smoother surfaces and pull easily without splitting the concrete longitudinally.

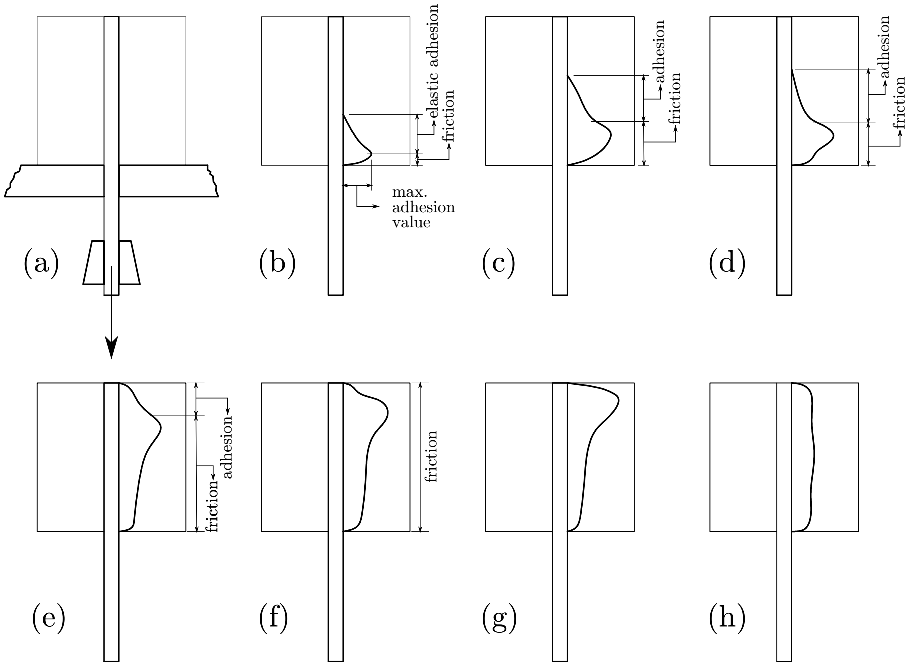

Figure 2-10: Bond stress variation during pull-out of a plain bar[146]

In deformed bars, the main contribution to the bond strength is due to the load bearing of the lugs onto the concrete, and consequently the shear and compressive strength of concrete between the lugs. The major failure mode is when the lugs create a wedge action and split the concrete (see Figure 2-9). A secondary failure consists in the shearing of concrete around the lugs, especially when reinforced concrete is made from well confined small rebars or by using lightweight concrete. Bond stress distribution along the bar under different force loading levels f_A (and equivalent strains ϵ_A) is given in Figure 2-11. While such curves were idealised due to the large errors in the experimental data, some physical observations were made as follows: (i) excellent bond stress transfer on the compression side was observed due to good concrete confinement and the Poisson's effect; (ii) bond stress transfer is much higher towards the tensile end and reduces further down the embedment; (iii) at higher loads, bond stress reduces towards the tensile end and increases further down the bond interface[31;48]. The bond-slip measurement was later improved to an accuracy of $\pm 2.54 \mu$m by measuring the resistance of a coil around the steel bar during pull-out action[123].

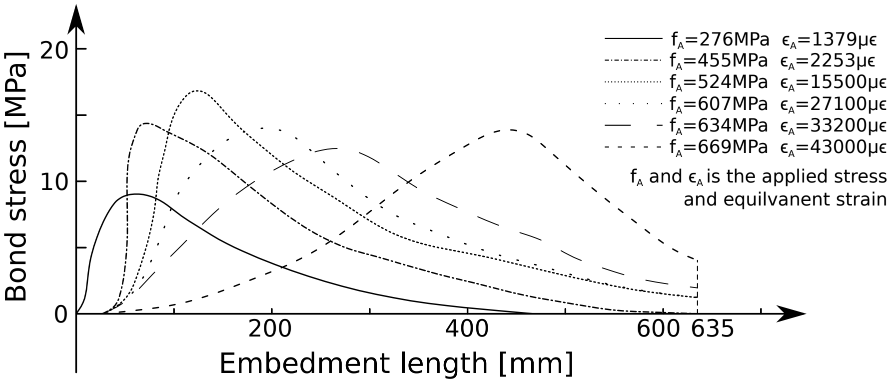

Figure 2-11: Bond stress distribution along an #8 bar at different loading levels[31]

Anchorage of steel reinforcement in concrete can provide stronger pullout resistance. Experimental results showed that the bond strength can increase by 72% and 14% when plain and deformed bars are anchored respectively using half around hook. Although a significant increase in pull-out strength was observed in anchored plain and deformed bars, this was due to the hanging effect especially in the plain bars, while a small increase in the bond strength was observed in the deformed bars[136]. This means that high compressive or shear stress exists in concrete nearby the anchorage zone of plain hooked bars and that the design of anchorages can be considerably problematic in concrete frame joints[109]. As this is similar to un-bonded pre/post-tensioned concrete structures, this aim of this research is to develop a replacement for steel rebars that can be used in smaller concrete building components.

Having gained an understanding of the bond behaviour between the steel reinforcement and concrete, it is necessary to study the mechanical behaviour of reinforced concrete as a composite material and to be able to predict the overall structural behaviour by using numerical techniques such as the finite element analysis. The following section comprises in an extensive literature review to understand the process of modelling reinforced concrete and how this could be applied to model the RBFR system.

2.2.2 Numerical modelling of reinforced concrete

Numerical modelling of steel reinforced concrete structures is a mathematical approach to evaluate their behaviour and determine their maximum deformation and load bearing capacity. Developing such numerical tools will allow structural engineers to design reinforced concrete structures such as frames, embankments, foundations and shell structures.

Several important works are reviewed here to highlight the important aspects required to build a numerical tool which is able to efficiently determine the true behaviour of reinforced concrete subjected to different types of loading.

2.2.2.1 Bond Models for Steel-Reinforced Concrete

Several attempts to derive an analytical model describing the bond behaviour between steel rebars and concrete has been made to predict the pull-out behaviour of rebars from concrete[149;151]. A more general analytical model that describes the bond behaviour of steel rebar in well-confined concrete[214] was presented to determine the pull-out response of steel rebars under cyclic loadings[40;41]. The nonlinear response in the bond-slip relationship[193] led to the introduction of plasticity bond models, such as Mohr-Coulomb[34], for the interface between rebar and concrete. Concrete interaction using empirical data for monotonic loading condition[49] and further for both monotonic and cyclic loading conditions[63;90]. A simple tri-linear bond stress-slip model (Figure 2-12) can be used for low levels of bond slip under monotonic loading[120]. The level of confinement that concrete gives to the embedded steel reinforcement is essential to its bond adhesion and a bond model was developed considering such confinement[55]. A more precise time-dependent bond model was presented by Lowes et al.[132] which includes the contribution of the mechanical interaction (due to bearing of steel lugs on concrete), residual friction (frictional bond strength after bond-zone damage) and virgin friction (initial friction until maximum bond strength is achieved) to the overall bond behaviour (see Figure 2-13). A complete model based on experimental data produced by Eligenhausen et al. and Malvar[63;137;131], was presented by Ožbolt et al.[157;127] which classify the parameters into two part. The basic model parameters such as the bond strength, the shape of the stress-slip curves and the loading-unloading-reloading rules. The second set of parameters depends on the geometry and on the strain state of the reinforcement bar and concrete in the vicinity of the bar.

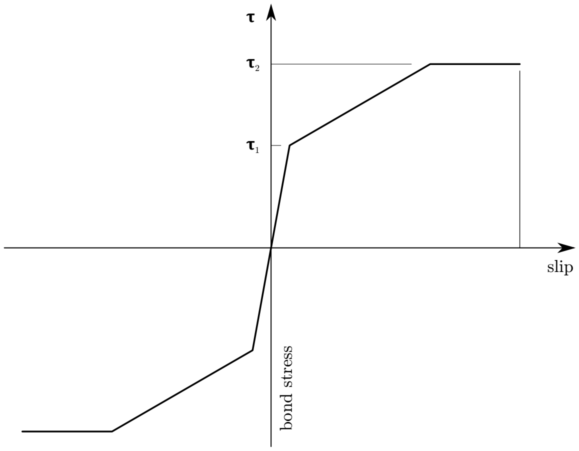

Figure 2-12: Trilinear bond stress-slip model[120]

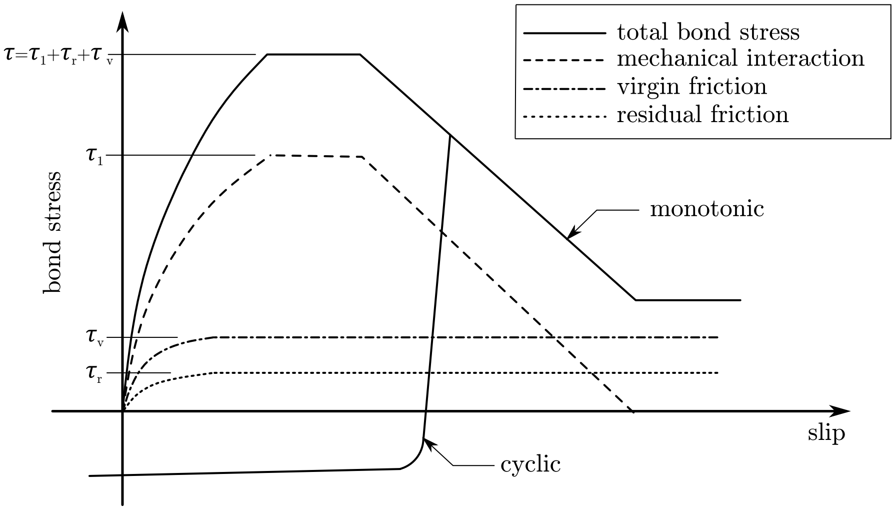

Figure 2-13: Bond stress-slip model for monotonic and cyclic loading[132]

2.2.2.2 Finite Element Modelling of Reinforced Concrete

According to Meyer: "It is the responsibility of the structural engineer to ensure that all structures are accurately analysed and designed to safely withstand the anticipated load"[142]. Numerical techniques are generally used to predict the behaviour of concrete structures subjected to different types of loadings. Seven years after the introduction of the finite element method FEM for civil engineering applications[43;44;45], Scordelis and Ngo made the first attempt to model reinforced concrete by using 2D plane stress elements to represent concrete and steel reinforcement. Concrete crack propagation was achieved by splitting the nodes to enabling crack formation between the finite elements[149]. Another approach to model fracture in reinforced concrete was to adjust the stiffness of the individual finite elements governed by a stress/strain crack criterion[163]. A further enhancement was the addition of bond-slip and material non-linearity response[150]. At an early stage some researchers adopted a linear elastic approach to model reinforced concrete due to lack of experimental work that defines the nonlinear response of concrete due to multiaxial stress states, bond stress-slip, aggregate interlocking, and effective dowel length[182]. Eventually, a new attempt to capture the non-linearity response of concrete was made by using a generalised Mohr-Coulomb yield criterion to predict the yielding point and failure of concrete under combined stress[37] followed by the use of Drucker-Prager yield criterion to achieve numerical stability[123]. A better representation of reinforced concrete behaviour under shear and compressive stress, which accounts for aggregate interlocking, was demonstrated in several FE examples and validated against experimental data[38;180].

As more experimental data emerged to describe the inelasticity, inelastic dilatancy, strain softening and hardening, hysteretic behaviour, degradation of elastic moduli, rate dependency and ageing of concrete, a more unified material model for concrete was developed by Bazant[22;23;21]. Adding other effects such as the dowel action mechanism, a complete FE model to analyse reinforced concrete was presented by Bergan[30] and Grootenboer[82]. Subsequently, Scordelis presented a unified to perform geometric and material nonlinear analysis of standard and pre-stressed reinforced concrete structures. This takes into account time-dependent effects due to load and temperature history, ageing of concrete and the relaxation of the pre-stressing steel[181]. Eventually, this led to the development of commercial software to accurately model the behaviour of reinforced concrete[16;17]. Furthermore, dynamic analysis of reinforced concrete was introduced to understand the structure response under cyclic loading such as seismic, wind, ocean and blast waves and impacts[142]. A new attempt to accurately model the bond slip between steel and concrete introduced a finite layer between these two materials, and between the internal cracks of concrete[123]. By introducing of new bond models as discussed in Section 2.2.2.1, the bond slip between steel and concrete was modelled more accurately under cyclic loading to produce a high-resolution finite element model of reinforced concrete structures[127].

2.2.3 Damage modelling in Finite Element Method

The modelling of the damage mechanisms such as de-bonding and cracking is essential to determine the overall response of reinforced concrete. This section will focus on the modelling of damage in the FEM, starting with a short introduction to fracture mechanics, followed by a discussion of the advantages and disadvantages of smeared and discrete crack modelling. The focus then shifts to cohesive-zone models as a discrete approach, followed by a review of different types of enhanced and enriched methods.

2.2.3.1 Introduction to Damage and Fracture Mechanics

Damage mechanics is the science explaining damage in materials. Damage such as cracking is when a material or matrix breaks apart, and de-bonding is the separation of a weak interface between two materials. The initial process of cracking or de-bonding occurs when micro-stresses accumulate around weak points in the materials or composite and form microvoids. Eventually, microvoids coalesce into bigger voids in which the cracks propagate at a mesoscale level[129].

The coupling between linear damage and elastic strains can be directly obtained by reducing the elastic material modulus E using a damage parameter D which varies from zero (no damage) to one (fully damaged). Therefore the new damaged elastic material modulus is defined as $\tilde{E} = E(1-D)$. In plasticity, damage reduces the yield stress (σ_y), the isotropic strain hardening stress R and the back stress (X). Therefore the reduction in stress is defined as $\sigma = (\sigma_y + R + X)(1-D)$[129]. The rupture criterion is defined as the initiation of cracking at a critical damage value D_c. D_c is defined as $D_c \simeq 1 - \frac{\sigma}{\sigma_u}$ (σ_u is the ultimate stress the material can resist) and in theory this varies between $D_c \simeq 0$ for brittle damage to $D_c \simeq 1$ for ductile damage, but is more likely to be in the region between 0.2 and 0.5[129].

Linear fracture mechanics is sometimes used to model the structural response of very large concrete structures. Depending on the crack/notch/hole geometry, Inglis[96] was able to determine the magnitude of the stress concentration by deriving a stress concentration factor κ especially at an infinitely sharp crack tip[107]. As a general rule, the sharper the crack or notch, or the smaller the hole, the higher the stress concentration. While the size effect was not considered in the stress concentration factor, Griffith later understood that cracks in large specimens tend to propagate when subject to a smaller force (i.e. smaller is stronger) and therefore he proposed an energy balance criterion[81], where the rate of strain energy release per unit of crack extension must be equal to the rate of surface energy released at the crack front[68]. Later we see the introduction of the stress intensity factor K_1, which tells us the magnitude of stress around an infinitely sharp crack tip . In combination with the Griffith energy (G) balance criterion, one can determine the fracture propagation in concrete[93] and other brittle materials.

2.2.3.2 Smeared vs Discrete Modelling

Smeared and discrete crack modelling are the two most common ways of modelling cracks in concrete. The introduction of smeared cracking in concrete goes back to 1968, when Rashid proposed a way of nucleating micro cracks into a dominant crack, and can capture deterioration in heterogeneous materials such as concrete[163]. On the other hand, a discrete crack model was proposed by Ngo and Scordelis to model the initiation and propagation of dominant cracks[149].

In smeared cracking approach, the crack opening gap in the finite element is represented by a crack strain and therefore the behaviour of concrete fracturing can be modelled by a stress-strain relationship[163]. In this approach, the cracking of concrete occurs when the principal tensile stress exceeds the ultimate tensile strength of concrete, and therefore the elastic modulus of concrete is reduced to zero orthogonal to the principal tensile stress direction[198]. Further work by Rots shows how smeared cracking can realistically predict the local fracture when taking into account the tensile strain-softening effect due to progressive micro-cracking and crack closing[170;171;172;175]. The size effect was introduced into the strain-softening formulation and adjusted to the chosen finite elements size leading to a mesh independent material fracture properties defined by the fracture energy, uni-axial strength limit and the width of the crack[18;19;18;24]. The introduction of fracture energy and crack band are two regularisation techniques that prevent ill-conditioning of the problem due to strain localisation[25]. In non-linear fracture mechanics, the size effect regularisation technique can also be used to determine the nonlinear fracture properties[20]. Further work shows the introduction of non-orthogonal smeared cracking with non-linear plasticity, creep, thermal effect and shrinkage[52]. A mixed-mode smeared crack model was proposed to cover the tension (mode I) and shear (mode II) softening, allowing unloading and reloading, and multiple crack formation[174;173].

In the discrete crack approach, crack propagation is resolved by node splitting to accommodating the crack propagation between the finite elements[149;53]. This means that crack length and direction is dependent on the FE mesh and re-meshing is necessary to reduce this dependency[97] (as cited in[53]). Interface elements are used to represent the mechanical link between the finite elements and consequently represent discontinuities in the FEM. Interface elements can be of two classes: continuous or nodal (identical to spring elements used in[149]) interface elements[178]. The discussion of interface elements and cohesive-zone models continues in the following three sections.

2.2.3.3 Modelling of reinforced concrete using cohesive-zone models

The use of interface elements between finite elements dates back to 1967 when Ngo and Scordelis modelled concrete crack propagation between finite elements[149]. Brown[34] adopts link elements (interface elements) in the FEM to simulate the bond adhesion between steel reinforcement and concrete while Lowes[132] uses zero thickness bond elements (cohesive elements) in 2D to investigate a new steel-concrete bond model. The mechanical description of the interface elements can be governed by the energy balance function proposed by Hillerborg[93], where a crack gap appears between the finite elements, and full damage is obtained as the fracture energy is fully dissipated (see Section 2.2.3.1). Interface elements can be used to model the bond behaviour of steel reinforcement and concrete[149;173], discrete cracking in concrete[173] and aggregate interlocking[149]. While traditional cohesive-zone models are used to model the bond interaction between steel and concrete[173] described in Section 2.2.1, new models can model friction[6] and interlocking effect[185] by using interface elements between steel rebars and concrete[186].

2.2.3.4 Enhancing methodologies for the interface elements

Interface elements are easily used in the FEM to represent discontinuities in and between materials. One of the interface element parameters is an initial penalty stiffness required to sustain the loading before damage is initiated. If this penalty stiffness is very large, spurious oscillations in the stress field can be observed when the Gauss integration rule is used to evaluate the interface stiffness matrix[173;72] (see Section 4.2.4). These oscillations can be reduced by using Newton-Cote or Lobatto integration schemes for linear interface elements, and by using a nodal lumping scheme for quadratic interface elements[178]. Other instabilities are associated with de-lamination of composite materials, especially when the laminates are very thin.

Therefore snap-through/snap-back behaviour can be observed[4] which can be controlled by a new arc-length method[88] and a double-line-search method proposed for interface elements[5].

2.2.3.5 Techniques in fracture modelling: application to interface elements

The modelling of fracture has evolved from a finite element mesh dependent technique[149] to adaptive mesh refinement[200] to capture the crack propagation. The introduction of embedded displacement jumps within the solid finite elements help the crack propagation to be determined independently of the finite element mesh. One method is done by regularising the discontinuous displacement field where the strains are bounded everywhere[62;155]. Another method that allows embedded displacement jumps makes use of the partition of unity method[140] as the finite element shape functions to allows the modelling of crack propagation through the solid finite element[143;26;216]. Later, level set method (LSM) has been introduced in X-FEM to represent the crack and the location of the crack tip[196].

While the above methodologies focus on the enrichment of the field, other works focus on the enrichment of the interface element in de-lamination where crack direction is known a priori. H-, p- and hp-refinement in the finite element method were introduced by Babuska to provide a better approximation of the field through the individual finite elements. Such refinement could be adaptive and based on an a priori or a posteriori error criterion that determines the level of h, p or hp-refinement required to achieve an accurate solution of the FE problem[10]. An adaptive hierarchical enrichment for the de-cohesive zone model introduced hierarchical polynomial functions around the softening process zone[50]. The idea of adaptive hierarchical enrichment is further developed in this thesis to conduct adaptive hierarchical p-refinement at the interface using the same approach adopted for the tetrahedron finite elements[2]. This type of enrichment was used in Section 4.2.4 to study the traction oscillation problem discussed in the previous Section 2.2.3.4, and throughout the thesis to model the de-bonding behaviour of fibre and concrete.

2.3 Appraisal of fibre mechanics

Fibre materials are identified as long and thin matter and characterised with distinct material properties. They have high tension and relative flexibility, making them suitable for a wide range of applications. Understanding the individual and composite mechanical behaviour of fibres is necessary to study the feasibility and mechanics of braided fibres in reinforcing concrete structures. This is done in various physical spatial approximation scales. At a micro level, the behaviour of every single filament is studied, while at a mesolevel, the behaviour of a bundle of fibres is studied. At a macro level, the collective mechanical behaviour of twisted/braided/composite fibres is studied.

In this section, some basic fibre and composite mechanics are given at different physical scales. It concludes with a literature review of the numerical modelling of woven/braided fibres and a brief discussion of how this approach was simplified to perform computationally efficient modelling of braided fibres.

2.3.1 Mechanics of fibres

The mechanics of fibres depend not only on the constituent material properties but, more importantly, on their physical characteristics. Fibres are defined as thin and elongated matter with different surface textures. While natural/organic fibres are more likely to have curved shapes with rough or uneven surfaces, synthetic fibres, such as carbon, glass and plastic fibres, are characterized more by straight geometry and smoother surfaces. The type of surface texture of fibres can have a significant influence on its material properties: mostly on mechanical interaction with other fibres and between fibres and other materials. Fibres are astonishingly resilient to tension and relatively flexible, capable of being shaped in a wide range of geometries.

Due to these advantages, fibres are used to manufacture braided ropes with high tension and with great potential for main concrete reinforcement.

2.3.1.1 Physical properties

Tows/strands and braided geometries have relatively low stiffness in the transverse plane (cross-section of fibre), compared to the stiffness along the fibre directions (principal stiffness) and considered as transversely isotropic and described by five material parameters (stiffness and Poisson's ratio in the transverse plane, stiffness in the principle axis, Poisson's ratio and shear modulus between the transverse plane and principle stiffness). Due to their brittle nature, in this research, it is considered sufficient to model fibres such as carbon, glass or aramid fibres as elastic up to rupture. Plastic constitutive models are necessary to model synthetic fibres such as high-density polyethene (HDPE) material.

Tows and strands, which are made from a collection of filaments oriented evenly in the same direction, are measured per thousand filaments; for instance, 3K is equivalent to 3000 filaments. They can be also be measured as a linear weight in the units of *tex*, where one *tex* is equivalent to a gramme of fibres per thousand metres ($1\ tex = 1g\ /\ 1000m$), which depends on the effective fibre density $\bar{\rho}$. A bundle of fibres is made up of both solids and voids. The effective fibre density $\bar{\rho}$ is equal to the weight per unit solid volume (V_s). The solid volume V_s is equal to the effective solid cross-sectional area ($\bar{A}$) multiplied by the length of the fibres, assuming that the filaments are continuous and that the same amount of fibres exist through the length of the tow. $\bar{A}$ can also be used to compute the effective tensile strength $\bar{\sigma} = \frac{F_c}{\bar{A}}$, where F_c is the maximum critical force to break the fibres. The tensile strength of glass fibres ranges between 800 and 1700 MPa, while that of carbon fibres ranges from 2000 to 5650 MPa[219].

Ageing of fibres, mainly in terms of deterioration and mechanical fatigue, is an important factor determined by the material properties of fibres and the surrounding environment. Deterioration can take the form of rotting (dry and wet process), insect and chemical attacks, exposure to corrosive environments, thermal degradation and other non-mechanical induced damage. Two typical examples are the exposure of common glass fibres to alkali environments and the oxidisation of carbon fibres at high temperatures. Modifying the chemical formula of the fibre material can be done by adding Zirconia (ZrO_2) to glass fibre or providing an adequate environment to the fibres, such as oxygen-free enclosure to carbon fibre. These are two ways of protecting the fibres and reducing the degradation process. Moisture absorption in fibres and composites is another degradation process, which results in swelling and directly influences the fibre-fibre and fibre-matrix adhesion. A secondary damaging process is induced by the exposure of composite containing moisture absorption to freezing or heating fluctuations that can damage the structural integrity of the composites.

2.3.1.2 Mechanics of fibre composites

The purpose of this section is to revisit the mechanics of fibre composites and braided fibres. Composite materials are usually made from reinforcement and matrix. Reinforcement takes the form of high tensile resistant fibres, while organic, cementitious, polymeric or metallic matter is used as a matrix to bind fibres together. Voids are also common in composites and minimises using appropriate impregnation techniques which eventually improve the properties of composite material. Composite materials are mostly considered heterogeneous materials, while homogenization techniques are conducted to provide computationally efficient numerical multi-scale modelling[210]. Heterogeneity depends on the configuration of the fibres, which can be scattered, unidirectional or multi-directional (weaving/braiding) in orientation. As a general rule, weaving is a 2D form of braiding, while knitting or sinnet is a 3D form of braiding. An essential material property of composites is the fibre-matrix bond behaviour, which influences their overall mechanical properties.

Fibres and matrix material properties, fibre distribution (see Section 2.3.1.3) and bind properties are essential in producing a good composite material. This combination makes it possible to distribute tensile stresses evenly among all fibres, and increase its compressive strength. Most importantly, though, this provides abrasion protection to the fibres. Tensile strength distribution depends on various factors such as the fibre-matrix bond strength, fibre-matrix volume ratio, fibre distribution, cracking patterns of the matrix, and material properties of both fibres and matrix. These properties also reflect the ways in and means by which a composite can fail.

In a unidirectionally reinforced composite, a common failure mechanism is when the matrix cracks and fibres break along the transversal plane of the fibres. Another failure mechanism is the cracking of the matrix, followed by a progressive fibre-matrix de-bonding failure[89]. Understanding the mechanics of composites can help to identify similar mechanical behaviour and failure patterns observed in fibre reinforced concrete.

2.3.1.3 Mechanics of twisting, braiding and weaving

For centuries, fibres were accumulated not only by using matrices but also by twisting, weaving, braiding and knitting. Capable of producing several products, fibre technology was and still is an essential science in various applications. Ropes have been manufactured using the same principles for centuries with very little technological improvement over recent decades. This art of combining bundles of filaments has produced ropes and cords which withstand tensile loading and are flexible enough to work with.

It is important to note that the total tensile strength of a tow is not equivalent to the sum of every individual filament's tensile strength. The total tensile strength is influenced by factors such as: filament length; distribution of fibres along the tow; thickness and surface texture of filaments; the overall thickness of the strand; and the type of twisting/braiding adopted to keep the fibres together[211]. A major weakness of twisted/braided fibres is the stress concentration of a particular region of the tow/strand. This is caused by lack of filament bedding-in after twisting/braiding, mishandling of tows/strands causing pulled filaments, and by excessive bending of fibres. The angle of twisting/braiding must be optimized to improve frictional adhesion between filaments and maximise the overall tensile strength of strands and ropes[139]. Optimisation depends directly on filament material, geometry, surface texture and strand size in comparison to braiding geometry. If, for example, filaments are made of a brittle material, excessive bending angles in the braiding geometry should be avoided, but should not hinder the frictional resistance between filaments that holds them together.

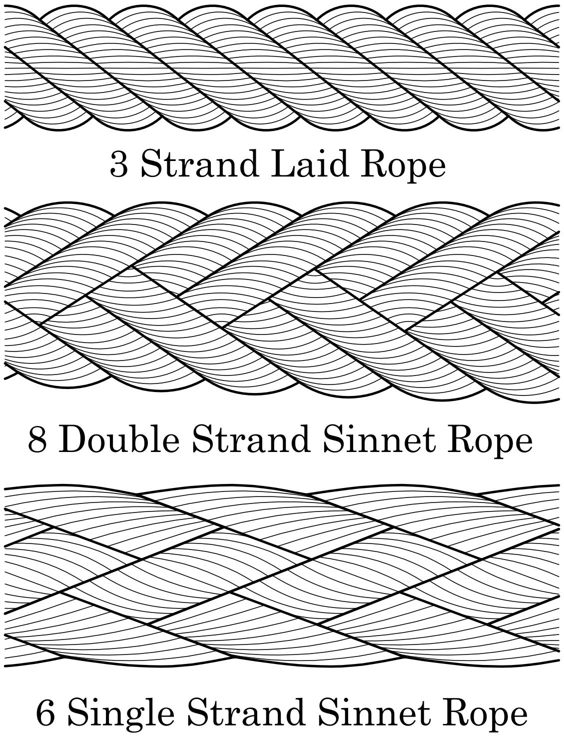

Figure 2-14: Three most common ropes

In general practice, an important property of ropes is their ability to absorb and restore energy during loading/unloading. This is dependent on both material and braiding type. The higher the braiding angle (angle between the principle axis and strand orientation), the more energy absorption is observed during elongation. Such elongation can be temporary or permanent, where permanent elongation is due to permanent absorption of energy and, to a certain extent, renders the rope unfit for use. A hysteresis effect is also observed during cycles of loading/unloading, where energy is lost and transformed into heat[139].

Abrasion constitutes another type of damage and can significantly damage fibres, especially brittle ones. Abrasion damage depends on two main factors: the fibres' surface texture and the extent or duration of this abrasion process. Other factors such as moisture content and temperature, among other conditions around the interface, can significantly influence the overall abrasion damage. Mitigation, such as embedding and pre-stressing of fibres, in addition to forming a rigid fibre-concrete bond interface, minimises this kind of damage. Due to lack of research in this topic, further study is necessary to determine the extent of damage when fibres are pulled-out from concrete.

2.3.1.4 Existing research on the numerical modelling of braided fibres

Numerical modelling of braided fibres is a relatively new topic with very few worldwide experts. Laboratoire Mécanique des Sols, Structures et Matériaux (MSSMat) led by Professor Durville in collaboration with Ecole Centrale (Paris), has been conducting experimental and numerical work to understand the mechanism of rope under various circumstances. The numerical investigation was adopted using finite element technology. Beam elements were used to represent fibres and contact mechanics to predefine (Figure 2-15) and retain the braiding geometry during the numerical simulation as shown in Figure 2-16[60]. This approach is computationally expensive and suffers when conducting large-scale problems. A new contact algorithm for beam elements was devised by Durville[61] to improve computational efficiency. This was later used to model multilayer braided scaffold to repair anterior cruciate ligaments[126]. Similarly, the mechanical response of braided fibres bending over sheave was examined for offshore application[215]. By conducting a numerical parametric study and experimental investigation, the scale effect was determined as the rope size increases and the life duration of similar ropes can be evaluated[51].

Durville et al demonstrate the use of beam elements representing individual fibres and a contact algorithm to model braided fibres that experience large relative movements. Alternatively, when the relative movement between the individual fibres and between two or more strands is relatively small, strands can be modelled as a single homogeneous material, while interaction between strands can be modelled using cohesive elements as described in Section 5.4, which is considered to be computationally cheaper than contact mechanics.

A similar area of research is the numerical modelling of woven composites. Woven composites are made from several layers of woven fibres glued with polymeric or ceramic resins. These types of composites are mostly used to construct lightweight cars, aeroplanes, marine vessels, wind turbine blades and other components requiring extreme strength, as well as light and corrosion resistance. The numerical modelling of woven composites using the FEM has boomed in the last few years and the industry is growing exponentially. Several mesh generators such as TexGen[128], WiseTex[212] and ScotWeave[91] exist to create woven geometries. However no mesh generators exist to create the sinnet braided geometries used in this thesis as an alternative concrete reinforcement. The mechanical modelling of woven composites is usually performed using a unit cell approach[177]. A homogenisation technique is then used to replicate the micro-mechanical behaviour at a meso/macro scale[218;217]. In sinnet braided profiles, it is thought that homogenisation can be simplified by an equivalent elastic transversely isotropic material exhibiting large deformations, as discussed in Section 5.6.2. Elastic transversely isotropic material was also used to represent the material properties of the woven yarns as described in Section 2.3.1.1, whereby the fibre directions are usually computed either from an expression defining the weaving geometry[58] or from a pre-defined yarn profile line embedded within the woven geometry[59]. While the first option can lead to complicated expressions to define arbitrary twisted yarns, the second option is only suitable to model yarns with constant cross-sections. This thesis proposes a new way to obtain the fibre directions of arbitrary twisted yarns with non-uniform cross-sections in Section 5.2.

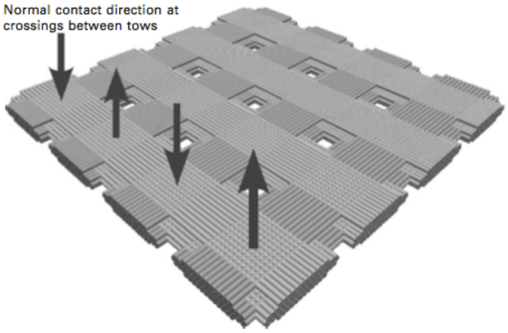

Figure 2-15: Initial configuration of microscoptic textile model[60]

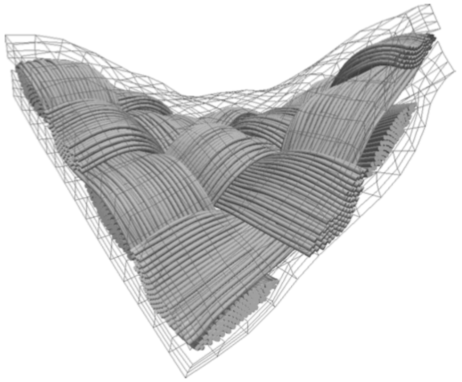

Figure 2-16: Mechanical deformation of plain weave composite[60]

2.4 Conclusion

This chapter has shown how small fibres contribute to the mechanical and thermal properties of concrete, producing high-performance fibre reinforced concrete HPFRC. HPFRC is characterised by high compressive strength and spalling resistant concrete when exposed to fire. This contributes to the fire-resistance of concrete structures, where the concrete cover is retained and main reinforcement is better protected from overheating. Other than providing fire insulation to the concrete structure, very little has been done to improve the fire-resistance of the main reinforcement. Research shows that steel and FRP rebars are not adequate as reinforcement if concrete structures overheat. While steel softens, FRP loses its composite integrity and, consequently, the bond adhesion between the reinforcement and concrete.

An appraisal of current studies of continuous fibre reinforcement, such as braided composite rods (BCR), carbon fibre composite cables (CFCC), un-resin continuous carbon fibre (UCCF), un-resin carbon-fibres assembly system (UCAS) and textile reinforced concrete (TRC), indicates that TRC can only be fire-resistant if produced using thermal resistant fibres and high-performance concrete. Further studies are necessary to prove this hypothesis. Understanding that UCCF can be used as main reinforcement for concrete by improving the mechanical properties of continuous fibres by braiding them into ropes similar to BCR and omitting the use of resins, this thesis proposes a new reinforcement system. It consists of strands of fibres braided over a string of glass beads to form ribbed braided ropes. While braiding replaces the use of matrices to merge all fibres together, glass beads produce a ribbing effect similar to rebars and adhere to concrete in pull-out action. This feature was studied in Chapter 3 by conducting pull-out experiments of RBFR embedded in concrete to determine the bond adhesion.

Very little is known about the mechanics of braided fibres when used in particular circumstances such as RBFR. In this thesis a numerical tool has therefore been developed to investigate the mechanical behaviour of braided geometries in various forms and conditions. To introduce this, the mechanics of fibres and braided fibres were described in brief. This chapter concludes by highlighting an existing numerical tool capable of simulating the woven/braided textiles. It also explains how this inspired a concern with producing a similar but more efficient numerical tool using finite element technology.

Chapter 3

Experimental Investigation

The long-term objective of this work was to design an alternative to steel reinforcement that improves the durability and fire-resistance of concrete structures. Braided fibre ropes were considered as a new type of reinforcement. It was however necessary to determine the mechanical performance and feasibility of the new reinforcement at room temperature. This chapter investigates the pull-out resistance for both normal and ribbed ropes, where ribbing was achieved by introducing glass beads inside the rope. Two types of material were considered for the ropes: carbon and aramid.

3.1 Introduction to the ribbed braided fibre reinforcement system

There are several benefits of using fibre reinforcement in the design of concrete structures. While steel reinforcement corrodes and its stiffness is reduced by 10% every 100°C increase above 150°C[102], fibrous materials such as carbon, Kevlar and glass can resist high temperature and, on average, their strength to weight ratio is five times greater than steel's. Although carbon and Kevlar are corrosion resistant (un-reactive and inert), a wide range of glass fibres such as concrete corrode in alkali environments. Therefore only alkali resistant (AR) glass fibres are suitable. Designing fibre reinforced concrete which adheres to Euro Code EN 1991 or other equivalent codes is thought to be a great challenge.

Continuous fibres are normally used in FRP rebars and as a substitute to concrete steel reinforcement, providing a lighter, corrosive resistant and magnetic induction proof concrete structures. FRP rebars can be manufactured either by continuous or braided fibres impregnated with resin. While continuous FRP rebars have to be machined and textured to provide suitable adhesion to concrete, braided FRP rods can provide bond strengths equivalent to those of steel rebars[154] at ambient temperatures.

However, the bond strength of continuous/braided FRP rebar is very weak at elevated temperatures[114] due to softening of the polymeric matrix and loss of composite. To circumvent this problem this thesis proposes a new system made from thermal resistant fibres, braided over a chain of glass beads to form ribbed braided fibre ropes (RBFR system). Both ribbing and braiding act as a mechanical binder and have several advantages compared to the chemical binders (resins) used in FRPs. Resins are expensive and do not biodegrade, whereas braiding is a relatively inexpensive process and does not make use of any harmful materials. RBFR ropes can be a cheap and environmental friendly concrete reinforcement substitute for steel reinforcement. The lack of resin and the use of fire-resistant materials is more likely to form a fire-resistant RBFR system compared to FRP and steel re-bars.

This chapter describes a series of pull-out tests at an ambient temperature of RBFR embedded in concrete that were conducted to determine its feasibility. This was compared with similar specimens using plain braided ropes (no ribbing) that depend on their surface texture to adhere to concrete. Only two adequate and cheap fire-resistant braided ropes were found on the market. The first was aramid ropes (Marlow T12 make), made from twelve strands of double-braided sinnet and supplied with a polyurethane coat that acts as an abrasion resistant layer. This coat was omitted when adopting such ropes to produce RBFR system and hence reduce the risk of weakening bonds at elevated temperature. Technora (a type of aramid fibre produced by Teijin Limited) T12 was used for both plain and ribbed system. The second option was Siltex carbon fibre rope manufactured from eight strands of single-braided sinnet, produced as fire insulation sealant. Due to the compactness of the braid and surface texture roughness (2mm variation in diameter), Siltex carbon fibre ropes were used to reinforce plain braided fibre ropes. Table 3.1 shows the specifications for both ropes used in these pull-out experiments, while Table 3.2 highlight some material properties of PAN carbon fibres used to manufacture Siltex carbon fibre ropes, and Technora T12 Marlow ropes.

Rope	Manufacturer	Diameter [mm]	Breaking Load [kN]	Elongation [%]
Carbon Cord	SILTEX GmbH	8	7.189 [ii]	14.1[ii]
Technora T12	Marlow Ropes Ltd	10	75.047 [iii]	2.7 [iii]

Table 3.1: Specifications of ropes in use

Fibre Material	Young's Modulus [GPa]	Tensile Strength [MPa]	Elongation [%]	Density [g/cm^3]	Decomposition Temperature [°C]
PAN Carbon	230	3530	1.5	1.76	500[65]
Aramid	78	3400	4.6	1.44	500

Table 3.2: Material Properties of Carbon and Technora Fibres

3.2 Pull-out experimental set-up

After proposing a RBFR system, it was necessary to determine its feasibility by examining a set of pull-out experiments of plain and ribbed rope reinforcement embedded in concrete and determine the ultimate bond stress that eventually can be used to design concrete structures.

[ii] data based of preliminary tensile tests.

[iii] manufacturer's data.

Standards norms to determine the bond strength of concrete reinforcement

Bond strength of steel reinforcement embedded in concrete can be determined by using the beam test methodology according to CEB/RILEM[100;166], or similarly by conducting pull-out experiments of steel rebars embedded in a beam-end specimen according to ASTM A944-09[106]. Bond strength for FRP can be determined in a similar fashion by pulling out the reinforcement from a vertical, beam-end, simple beam, hinged beam-end, splice or other types of specimens in compliance to ACI 440.3R-04[99]. The vertical bond pull-out test described in ACI 440.3R-04 was partially adopted to determine the pull-out strength for both plain and ribbed braided fibres reinforcement, as described later in this section.

Description of ropes used as reinforcement

Two types of ropes were used for the pull-out investigation: a 10mm twelve strand double braided sinnet Technora T12 Marlow rope and an 8mm eight strand single braided sinnet Siltex carbon fibre rope, as highlighted in Table 3.1. The Siltex carbon fibre rope diameter varies between 8 to 10mm (when the rope is not loaded) and is thought to provide good adhesion without the need of ribbing. The surface texture of Technora T12 Marlow rope is very smooth and hence this was investigated with a plain and ribbed surface during pull-out testing. To create ribbing, oval glass beads were inserted into the braided rope. The profile of the oval glass beads was 8mm in diameter and 12mm in length with a 1mm hole throughout the longitudinal length. Only one bead was used in the designated bonded area (Figure 3-1) in accordance with ACI 440.3R-04.

Description of concrete for pull-out specimens

In accordance with ACI 440.3R-04, concrete used for pull-out specimens has to be produced from Portland cement and aggregate of no more than 25mm in size, with a slump of 100 ± 20mm, and a compressive strength of 30 ± 3MPa at 28 days of

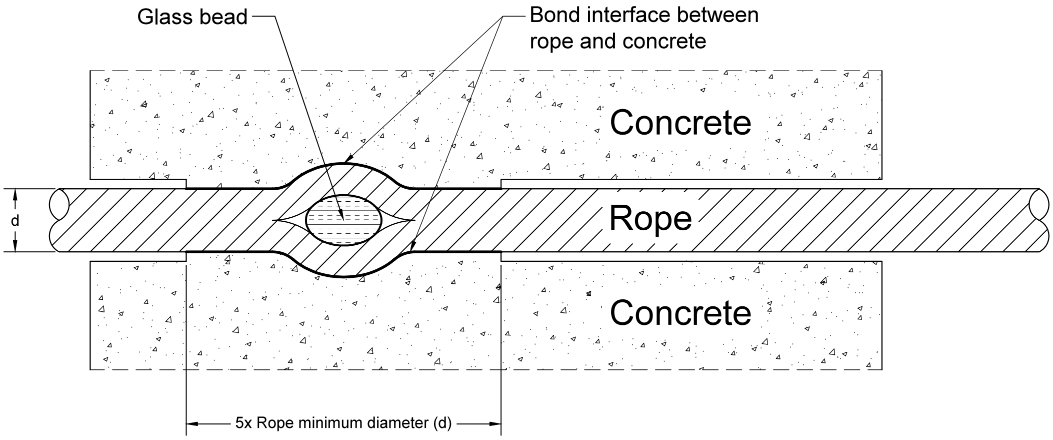

Figure 3-1: Ilustration of a designated bonding area between rope and concrete using a single bead ribbing

standard curing in compliance with BS EN 12390-2:2009[104]. A 1 : 2.56 : 2.56 (cement : fine aggregate : coarse aggregate) concrete mix with a 0.5 free water to cement ratio was designed using a 20mm maximum coarse aggregate, and fine aggregate of which 30% passed through the 600 μm sieve. Compressive strength was determined according to BS EN 12390-3:2009[105] standard.

Preparation of samples

Vertical pull-out specimens were prepared using cylindrical moulds rather than cube moulds, as proposed in ACI 440.3R-04. The assembly consisted of a cylindrical cast iron mould, measuring 150mm in diameter and 300mm in height, fixed on a wooden base with a hole in the centre through which the reinforcement was passed and anchored to the bottom side. On top of the mould, a bottle screw tensioning mechanism was designed to anchor and pre-tension the reinforcement as shown in Figure 3-2. The designated bonded area located at the base of the sample is required to have a length of five times the diameter of the rope and is prepared by retaining the area exposed to concrete while covering the rest of the rope using PVC tape, preventing adhesion to concrete as shown in Figure 3-2. The Siltex carbon fibre ropes were pre-tensioned up to 1000N and the Technora T12 ropes were pre-tensioned up to 2000N at a speed rate of 1.3mm/min on a tensile machine. Soon after, the mould was cast up to 200mm in height following standard procedures described in BS EN 12390-2:2009[104]. Six standard concrete control cubes were cast and tested in accordance with BS EN 12390-3:2009[105] and repeated for the three sets of pull-out experiments summarised in Table 3.3.

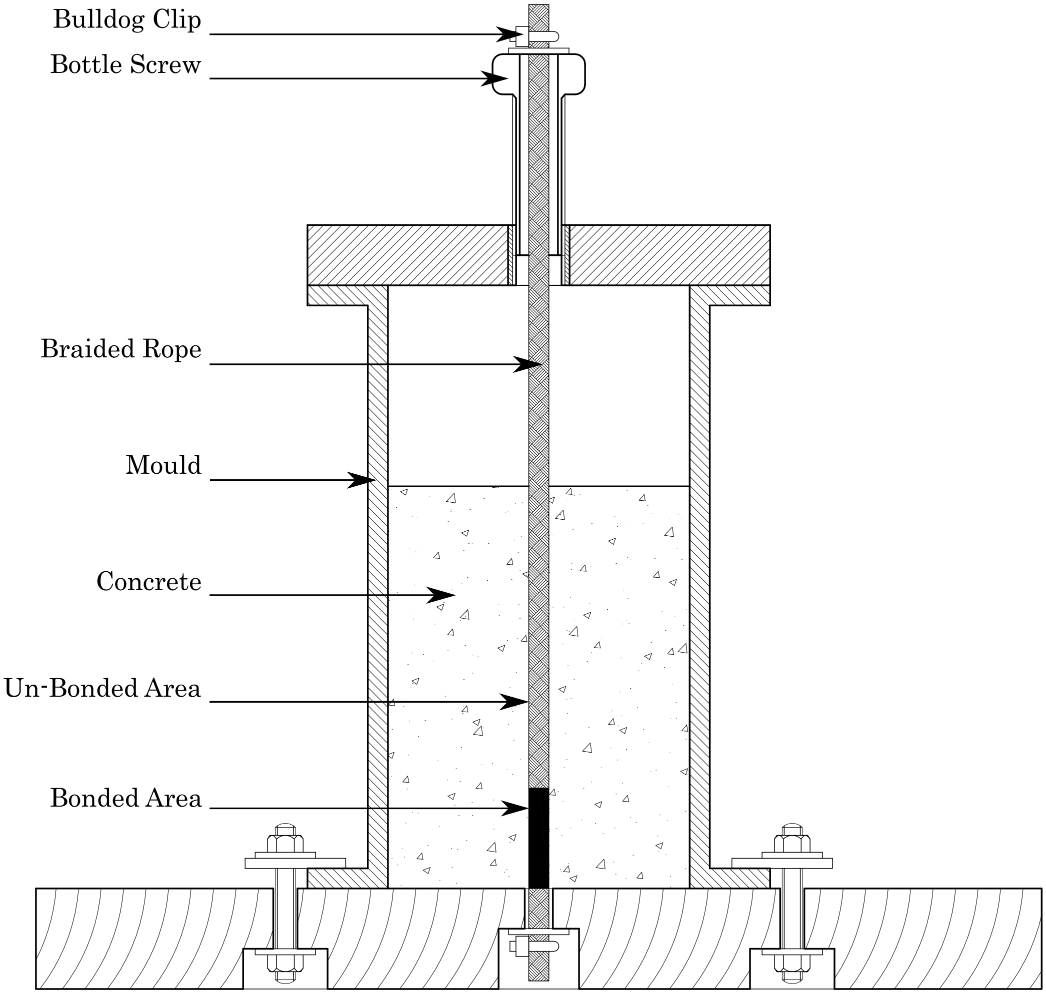

Figure 3-2: Mould Setup Assembly

Specimens were covered with a polyethene sheet for 48 hours to prevent dehydration. The moulds were disassembled and all samples, plus the concrete control cubes, fully submerged in a water tank at a temperature of $23°C$ for 28 days to conform with BS EN 12390-2:2009[104]. After curing, specimens were dried in a draft-free environment at standard temperature for 24 hours before the pull-out experiments were conducted.

Six pull-out specimens were produced for both plain Siltex carbon fibre and plain Technora T12 ropes. Another six pull-out specimens were produced for ribbed Technora T12 ropes. All samples are summarised in Table 3.3.

Sample ID	Rope	Concrete	Ribbing
CP8-1 to CP8-6	8mm Carbon - 8 strands	C30	None
TP10-1 to TP10-6	10mm Technora - 12 strands	C30	None
TR10-1 to TR10-6	10mm Technora -12 strands	C30	Ribbed

Table 3.3: Summary of Samples

Pull-out testing procedure

Pull-out tests were conducted on a 250kN Zwick Roell tensile machine, calibrated up to ±1% load precision. A pull-out assembly was designed, made from a 15 x 300 x 300mm steel plate used to clamp down specimens on the tensile machine base using four M16 threads bars, as shown in Figure 3-3. Between the steel plate and the specimens a rubber sheet was used as a cushion to prevent load concentration from uneven concrete surface, as this could result in unwanted cracking. A hole in the middle of the steel plate was drilled to allow the rope reinforcement passed through and clamped with the machine head's pin using a bulldog clip as shown in Figure 3-3. The pull-out action was performed at a speed rate of 1.3mm/min and readings of the pull-out force and displacement of tensile machine head were taken at a frequency of no less than 1Hz.

Recording and report pull-out experiments

During and after the pull-out tests, samples were under continuous observation to record various behaviours. At the end of the pull-out experiments, samples were split into halves to measure the length and position of the bonded area using a standard metric ruler. Afterwards, logged pull-out force and displacement data was plotted as the load-displacement curves and studied for both common and unusual patterns. Remarks and recommendations on the attained results were given, highlighting gaps

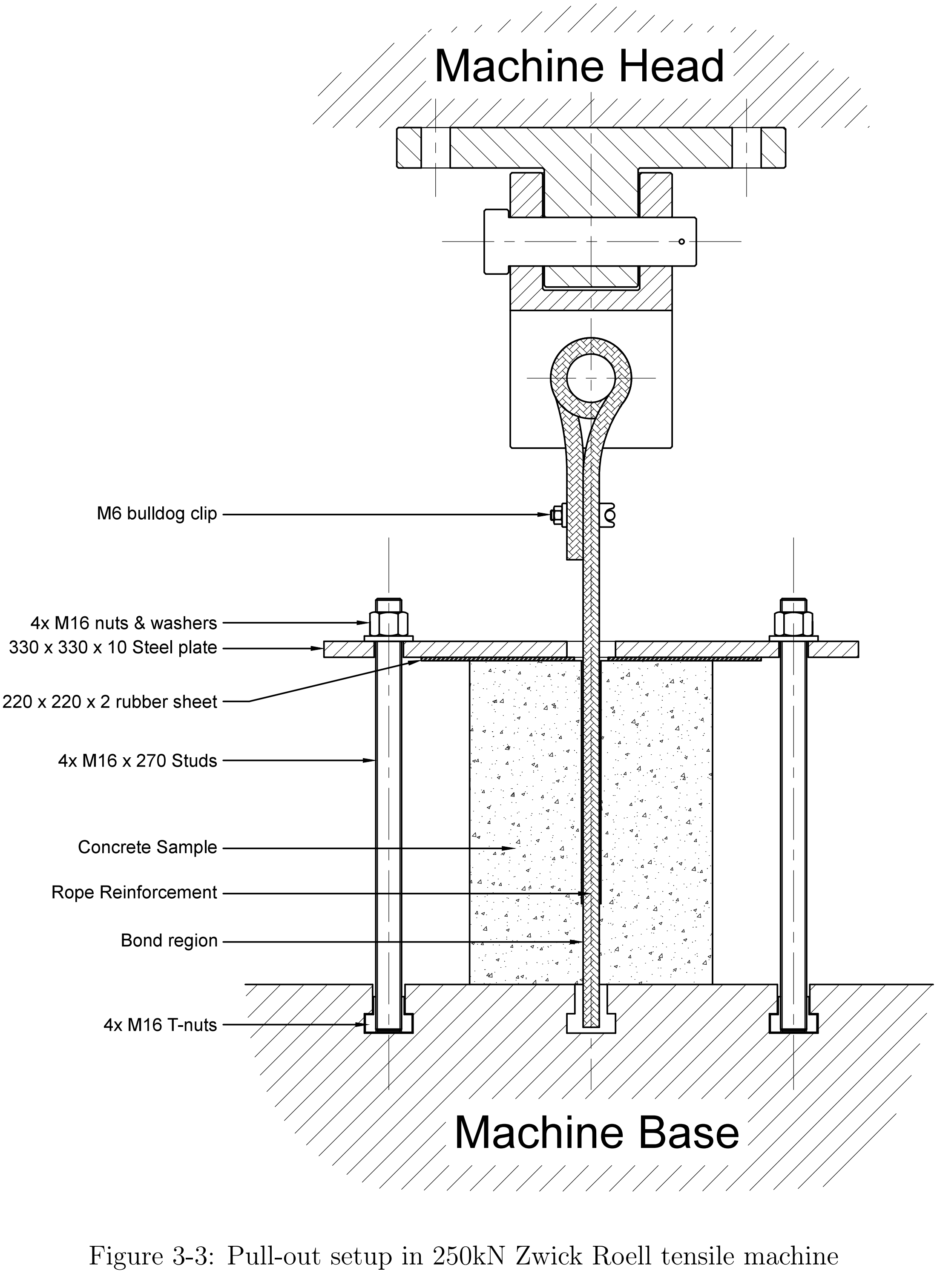

Figure 3-3: Pull-out setup in 250kN Zwick Roell tensile machine

in research for further investigation. The bond stress at failure by slipping τ_r was computed according to equation D.1 in[103].

3.3 Results

The aim of these pull-out experiments was to determine the ultimate bond stress τ_u provided by braided fibre rope reinforcement embedded in concrete. This is an important measurement to determine the feasibility of the proposed system as concrete reinforcement by comparing τ_u with the maximum bond stress recommended for concrete reinforcement expressed as $\tau_r \geq 0.098(130 - 1.9\phi)$[100], where ϕ is the nominal diameter of the reinforcement. The elongation percentage of the reinforcement and its elastoplastic behaviour are two important properties that determine whether the reinforcement is suitable for concrete structures. Due to lack of experimental resources and a short time frame for experiments, these two properties were not investigated but this is recommended for future research.

3.3.1 Regular braided carbon fibre reinforced concrete - CP8

Bond adhesion of braided carbon fibre ropes was examined. The 8mm Siltex carbon cords consisted of a very compact single braided sinnet with an uneven surface texture, initially thought to provide a good bond adhesion without the need of ribbing as proposed in the RBFR system. Pull-out experiments were conducted for plain 8mm Siltex carbon cords, where bond strength was determined and reported in this section.

Concrete quality

Concrete mixture was designed in accordance with Section 3.2. The ultimate compressive strength was determined at 34 days and found to be 43.2MPa on average, as shown in Table 3.4. Extrapolation from a compressive strength gain graph[220] shows that the concrete strength was around 40MPa at 28 days. This exceeds the design value of 30 ± 3MPa and hence the cement to water ratio was increased to 0.64 for the other pull-out experiments.

Cube ID	Age of curing (days)	Weight (kg)	Density (kg/m^3)	Compressive Stress (MPa)
C-CP8-1	7	2.39	2390	26.3
C-CP8-2	7	2.37	2370	23.8
C-CP8-3	7	2.38	2380	25.3
Average at	**7 days**			**25.1 MPa**
C-CP8-4	34	2.36	2360	43.5
C-CP8-5	34	2.36	2360	41.5
C-CP8-6	34	2.38	2380	44.6
Average at	**34 days**			**43.2 MPa**

Table 3.4: Compressive testing of concrete control cubes for CP8 specimen

Pull-out observations and results

The clamping system adopted for this first batch of samples consisted of an 8mm Siltex rope length attached at one end to the tensile machine head pin. The other end was clamped with the rope's end of the pull-out samples using two bulldog clips to form a straight overlap configuration (Figure 3-4). This clamping system was seen to fail as the rope stretches and narrows its cross-section (Figure 3-5), and therefore further re-tightening was necessary at around 500N and 1000N of pull-out force. This process disturbed the load cell readings as observed in the load-displacement curves (Figure 3-6). While samples CP8-4,5 and 6 experienced debonding failure, reinforcement for samples CP8-2 and 3 experienced tensile failure, where CP8-2 is thought to have experienced interlocking due to a loose aggregate in the unbounded region. A summary of the results is given in Table 3.5. The overall pull-out behaviour can be interpreted as comprising three main parts. The initial part consists of the stretching and embedding of the rope while under tension. The second part is characterised by the elastic stiffening of the bond, and the third part is characterised by a sharp loss of stiffness (debonding failure). Some additional pull-out resistance was observed (Figure 3-6) due to extra frictional resistance, induced from the rough concrete surface acting on the rest of the rope during the pull-out action.

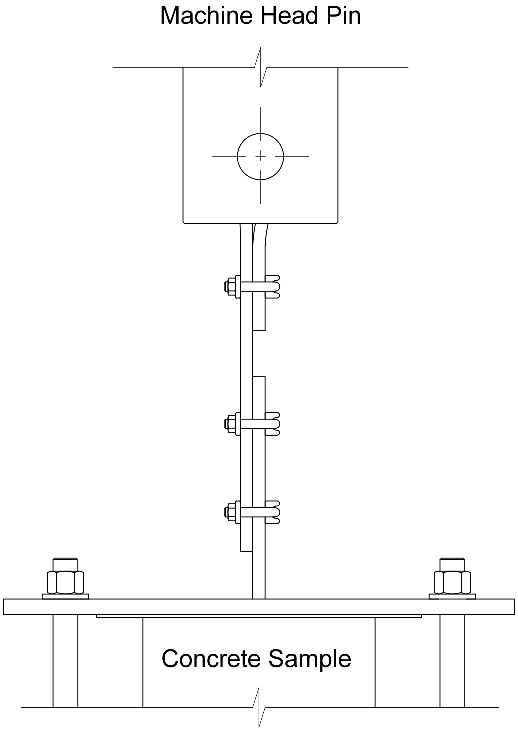

Figure 3-4: Clamp system of CP8 samples

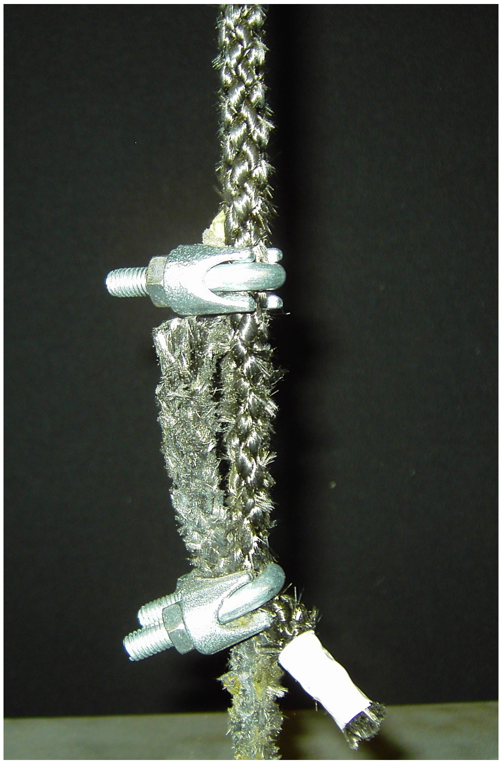

Figure 3-5: Failure in the CP8 clamp system

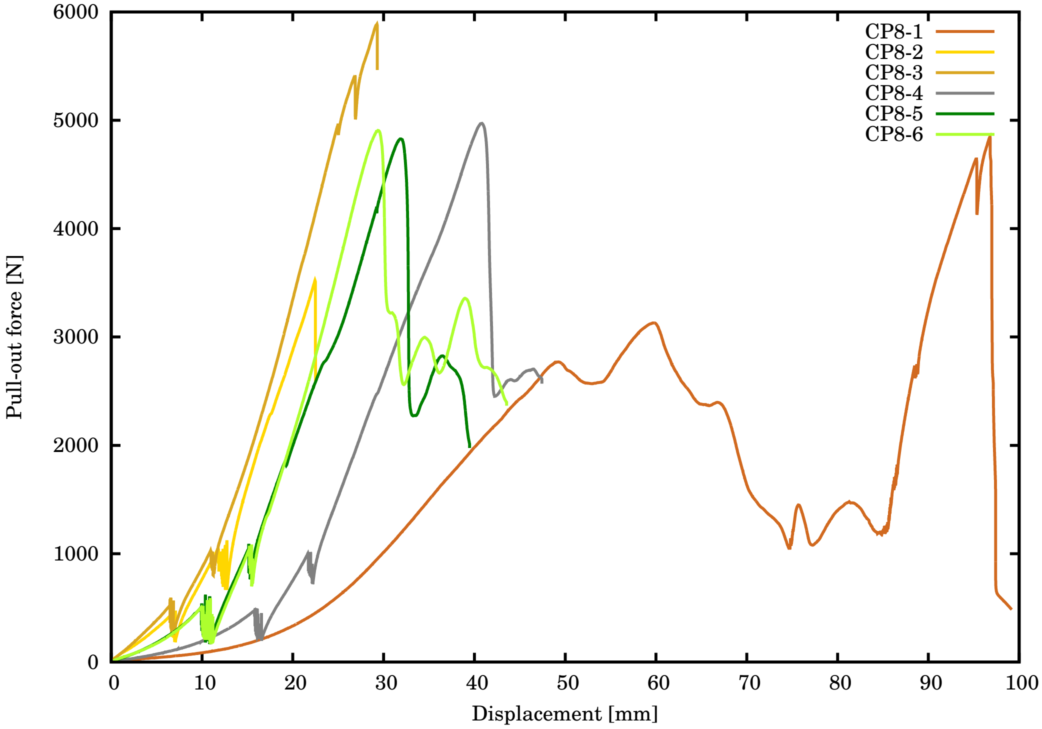

Figure 3-6: CP8 Load-Displacement graph

Samples CP8-4, 5 and 6 show consistent load-displacement behaviour, having approximately the same pull-out strength but with different elongations. This suggests anchorage slippage was present but not visible to the naked eye. Samples CP8-1,4, 5 and 6 were used to determine the bond stress from the maximum pull-out force and bond area, where the bond area was equal to the bond length times circumference of the 8mm rope. The average bond stress of 4.17MPa was achieved as shown in Table 3.5. This is equivalent to 37% of the bond stress of an 8mm steel rebar (equal to 11.25MPa) according to BS EN 1992-1-1:2004[100].

Specimen ID	Failure mode description	Ultimate failure load (N)	Bond length (mm)	Bond Stress (MPa)
CP8-1	Slip from anchorage proceeded with de-bonding failure	4849.82	53	4.16
CP8-2	Tensile failure of rope	3533.48	58	n/a
CP8-3	Tensile failure of rope	5887.09	64	n/a
CP8-4	De-bonding failure	4971.85	58	3.90
CP8-5	De-bonding failure	4828.26	50	4.39
CP8-6	De-bonding failure	4906.18	53	4.21
			Average	**4.17 MPa**

Table 3.5: Pull-out test results for CP8

Although the unbonded area was covered with PVC tape to prevent adhesion, a frictionless condition was not guaranteed due to uneven concrete surface adjacent to the reinforcement as shown in Figure 3-9, and might have contributed to the overall pull-out strength. A better approach was to dress the rope with a loose fit pipe to ensure it was free and not in contact with concrete in this region.

A major problem was the tensile resistance of these carbon fibre ropes, due to their very low pitch/diameter ratio. Tensile failure before de-bonding is not recommended as it can result in an instant collapse of concrete structures at the ultimate limit state, and is not for this reason permitted by EN 1992-1-1[100]. Preliminary tensile tests on Siltex carbon fibre ropes proved that they are very weak in tension (low breaking load is shown in Table 3.1). This prompted discussion with Siltex's representatives to improve the tensile strength of these carbon fibre ropes, but an agreement was never reached and no further studies were undertaken using carbon fibre ropes with a low pitch to diameter ratio.

In the following set of experimental results, stronger un-coated fire-resistant 10mm Technora T12 Marlow ropes were used as braided rope reinforcement. Their surface texture is very smooth and a RBFR system was therefore adopted. A glass bead in the bonded area was used to create a single rib and eventually enhance the bond strength that was compared to the plain reinforcement system of the same kind of ropes.

3.3.2 Regular braided technora fibre reinforced concrete - TP10

This set of experiments was designed to measure the percentage of bond enhancement between plain and ribbed ropes embedded in concrete. The setup was similar to the one used above, described in Section 3.3.1, but with a better anchorage system and an adjusted concrete mix as discussed below. As already noted in Section 3.2, pre-tensioning of ropes was increased from 1000N to 2000N for Technora T12 ropes to maximise the compactness of the rope's cross-section, meaning fewer loose fibres increase the rope's friction. This has improved the bedding-in of strands and compactness of fibres and consequently enhances the bond strength with concrete.

Concrete quality

Due to an increase in the free-water to cement ratio, an average of 36.4MPa compressive strength was achieved at 28 days of standard curing. It is thought that stronger concrete produces better bond adhesion with reinforcement, especially when ribbed reinforcement is used. Unfortunately this could not be observed in this set of experiments and further experiments are required to determine the relationship between concrete strength and reinforcement bond strength. Moreover, the moisture content of concrete is thought to influence the bond strength of concrete and, similarly, further studies are required.

Cube ID	Age of curing (days)	Weight (kg)	Density (kg/m^3)	Compressive Stress (MPa)
C-TP10-1	7	2.27	2270	22.3
C-TP10-2	7	2.34	2340	20.2
C-TP10-3	7	2.38	2380	23.8
Average at 7 days				**22.1 MPa**
C-TP10-4	28	2.35	2350	36.2
C-TP10-5	28	2.36	2360	37.3
C-TP10-6	28	2.38	2380	35.6
Average at 28 days				**36.4 MPa**

Table 3.6: Compressive testing of concrete control cubes for TP10 specimen

Pull-out observations and results

The pull-out behaviour of the TP10 samples shown in the load-displacement curves in Figure 3-7 can be classified into two parts: the initial phase is when the rope loses its adhesion from concrete and de-bonds, while the second phase consists of a continuous cyclic frictional pull-out resistance. While the initial phase has a predominantly gradient friction reflecting the fibre-concrete chemical adhesion, the second phase has a predominantly cyclic friction governed by the surface texture of the rope. The amplitude is thought to be governed by the amount of pre-stressing onto the rope. It was also observed that prolonged frictional abrasion caused some damage to the fibre. The maximum pull-out force was not attained after the initial stiffening, but rather at random places during the pull-out process.

The bond stress was determined by the maximum pull-out force per unit in the bond area, where the bond area was equal to the bond length times the circumference of the 10mm rope. The average bond stress was found to be 1.31MPa, which was significantly weak compared to the CP8 sample, and only 12% of the bond stress of a 10mm steel rebar (equal to 10.88MPa) according to BS EN 1992-1-1:2004[100].

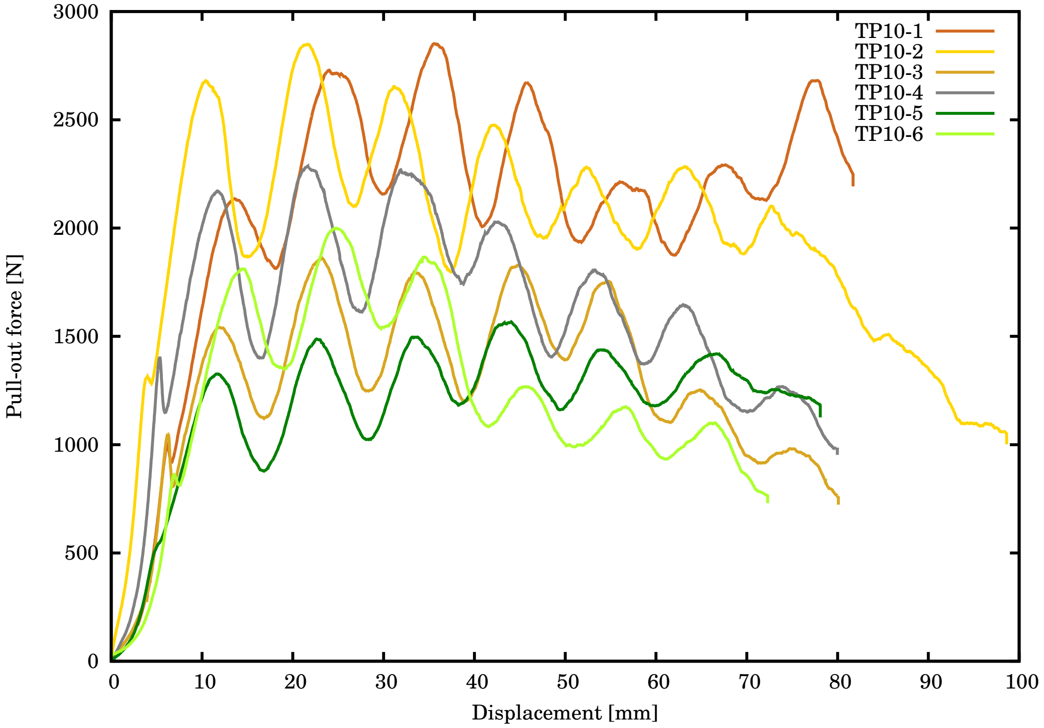

Figure 3-7: TP10 Load-Displacement graph

Specimen ID	Ultimate failure load (N)	Bond length (mm)	Bond Stress (MPa)
TP10-1	2851.47	55	1.65
TP10-2	2848.72	55	1.65
TP10-3	1861.55	53	1.12
TP10-4	2285.51	54	1.35
TP10-5	1999.78	54	1.18
TP10-6	1567.68	57	0.88
		Average	**1.31 MPa**

Table 3.7: Pull-out test results for TP10

The results suggest that the designated bonding area does not provide an adequately rigid bond with concrete. Therefore the plain Technora T12 reinforcement system is not suitable as concrete reinforcement and results were only used to be compared with the RBFR system.

3.3.3 Ribbed braided technora fibre reinforced concrete - TR10

Bond strength enhancement for Technora T12 ropes was necessary and made possible by adopting the proposed RBFR system. Glass beads formed the ribbing surface texture to the ropes that enhances the pull-out strength when embedded in concrete. This set of pull-out experiments examines the bond strength of ribbed braided Technora ropes embedded in concrete, using a glass bead to form a single rib located in the designated bond area as discussed in Section 3.2.

Concrete quality

Although the concrete mix ratio was the same as that used in Section 3.3.2, an average compressive strength of 40.2MPa was achieved at 28 days of standard curing. This may be due to a technical error leading to incorrect water to cement ratio, which eventually reduced the slump significantly. As discussed in Section 3.3.2, this is thought to have contributed to the extra bond strength reported in this section.

Cube ID	Age of curing (days)	Weight (kg)	Density (kg/m^3)	Compressive Stress (MPa)
C-TR10-1	7	2.37	2370	21.3
C-TR10-2	7	2.36	2360	21.0
C-TR10-3	7	2.38	2380	23.9
Average at 7 days				**22.0 MPa**
C-TR10-4	28	2.37	2370	41.1
C-TR10-5	28	2.36	2360	39.6
C-TR10-6	28	2.37	2370	39.8
Average at 28 days				**40.2 MPa**

Table 3.8: Compressive testing of concrete control cubes for TR10 specimen

Pull-out observations and results

The pull-out load/displacement curves were plotted in Figure 3-8. The initial loading stage was very similar to that of TP10 and CP10 samples, where embedding of strands/fibres was observed during the initiation of loading. This was followed by a rapid increase in bond stiffness until the debonding mechanism was initiated. Then a sharp loss of stiffness, representing a major debonding, was observed with some residual bond strength due to extra friction with the concrete. Concrete cracking was observed (Figure 3-10) due to tensile stresses induced by the rib onto the concrete and, in some cases, the crushing of the glass bead. Rupture of fibres was observed among all samples in various magnitudes of damage. It was unable to determine the percentage of fibre rupture during different stages of the pull-out process. The hypothesis suggests that very few fibres were damaged up to the maximum pull-out force, and most of the damage happened afterwards when exposed to further concrete abrasion resistance. Further studies are necessary to determine the rate of fibre rupture in proportion to the extent of the pull-out.

Similarly to Section 3.3.2 the bond stress was determined as shown in Table 3.8, resulting in an average bond stress of 7.22MPa: 5.5 times the average bond stress of TP10 samples. This is equivalent to 66% of the bond strength required by a 10mm steel re-bar in accordance with BS EN 1992-1-1:2004[100].

Specimen ID	Ultimate failure load (N)	Bond length (mm)	Bond Stress (MPa)
TR10-1	12425.1	51	7.75
TR10-2	12266.4	50	7.81
TR10-3	11388.7	54	6.71
TR10-4	9896.0	50	6.30
TR10-5	12562.5	55	7.27
TR10-6	11731.7	50	7.47
		Average	**7.22 MPa**

Table 3.9: Pull-out test results for TR10

As a general note, it is recommended that these experiments be repeated using differ-

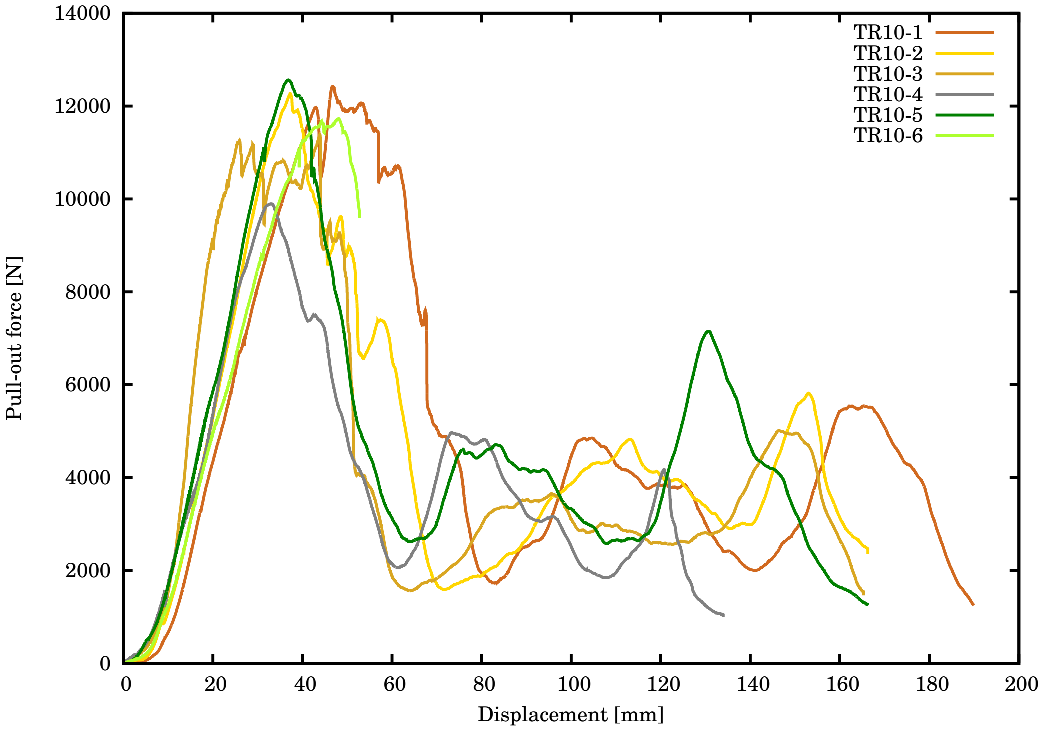

Figure 3-8: TR10 Load-Displacement graph

Figure 3-9: Specimen section of CP8

Figure 3-10: Concrete cracking marked in black for TR10 sample

ent concrete strengths, moisture contents, sizes of beads and different types of braids made from fire-resistant fibres.

3.4 Discussion

Pull-out experiments of ropes embedded in concrete have delivered various challenges due to its novelty and lack of experience. This section summarises main observations and achievements, followed by a discussion of how the RBFR system can be improved. It also highlights gaps in research and recommends further work.

During this set of experiments, it was found that plain 8mm Siltex carbon fibre rope (CP8 samples) was not suitable for concrete reinforcement because they are very weak in tension and do not provide sufficient bond strength. Further studies are required to improve the tensile strength of carbon fibre ropes while adopting the RBFR system to improve the bond strength between the reinforcement and concrete, as these could be used as concrete reinforcement and conform with EN1992-1-1[100]. Similarly, plain 10 mm Technora rope (TP10 samples) only provided frictional resistance during pull-out testing due to its smooth surface, and does not take the advantage of concrete confinement as discussed in Section 2.2.1 when ribs are present on the surface of the reinforcement. Pull-out experiments of RBFR made from 10mm Technora rope ribbed with an 8×12mm glass bead (TR10 samples) obtained 66% of bond strength compared to a 10mm steel re-bar. This verifies that the RBFR system can be a feasible main concrete reinforcement if optimised, by modifying the size, geometry, material and frequency of the beads. The RBFR system provided an enhancement of 5.5 times the bond strength compared to plain Technora reinforcement (TP10).

Concrete confinement plays an important role in the overall bond strength, as discussed in Section 2.2.1. It is necessary that this confinement is enough to withstand the tensile stresses exerted by the ribs on the concrete. During de-bonding of the RBFR system, it was observed that concrete confinement was insufficient during the appearance of longitudinal cracks in concrete, but sufficient when glass beads were crushed instead of concrete cracking. As the pull-out experiments were standardised with pre-defined concrete strength and sample dimensions, the ribbing height can be reduced to mitigate longitudinal cracking. Likewise, increasing the frequency of the ribs (glass beads) could achieve a similar or better pull-out strength. De-bonding was followed by progressive fibre rupture damage due to the friction contribution between the reinforcement and concrete. Pre-tensioning of the RBFR system can significantly contribute to the friction of the bond strength due to an increase in fibre compactness, therefore providing a better and rigid bond with the concrete. This was validated by observing the elastic stiffening behaviour of the bond during the pull-out action.

It is necessary that such experiments are repeated for different concrete strengths and moisture content to determine their influence on the bond strength of the RBFR system. Other variants, such as the fine to coarse aggregate ratio and curing process, need further investigation into how they influence the bond strength and behaviour. It is also worth investigating a different type of braid, since it was identified that low pitch to diameter ratio provides better bond adhesion (comparing CP8 to TP10), although it also weakens the tensile strength of the rope.

Experimental work has shown that the RBFR system can be used to reinforce concrete structures and possibly increase fire-resistance. Another gap in the research is the need for numerically modelled braided fibres to show how they behave when bonded with other materials. The following three chapters will discuss the methodologies developed in this thesis to model braided fibres and their interaction with other materials. It uses hierarchical higher order interface elements and replicates numerically the pull-out experiments discussed in these chapters.

Chapter 4

Hierarchical higher order approximations for interface elements

Having determined the feasibility of ribbed braided fibre reinforcement (RBFR) systems for concrete reinforcement in the previous Chapter 3, this thesis develops a computational modelling framework to simulate and investigate bond behaviour between RBFR ropes (reinforcement) and concrete. Within the context of the Finite Element Method, attention is focused on the modelling of the interface between the concrete and RBFR using cohesive elements and hierarchical higher order (HO) approximations. Hierarchical higher order interface elements are required to provide an accurate approximation of the interface if material and geometrical non-linearities exist. It will be shown that local p-refinement on the interface is possible and the rate of convergence can be improved to reduce the computational cost without mitigating the accuracy of the solution.

4.0.1 Overview

This chapter aims to discuss hierarchical higher order approximations and their use within cohesive elements. The need for various types of refinements is explained, as well why higher order polynomials are preferred within different contexts. Next the construction, properties and numerical implementation of hierarchical piecewise polynomial basis functions are discussed. The focus then switches to how hierarchical higher order approximation techniques are used for cohesive elements and illustrated with two examples: first, a de-lamination problem for which uniform and localised h, p and hp-refinement were used; second, an investigation into the use of localised p-refinement to solve the traction oscillation problem induced at notches.

4.0.2 Higher order elements versus hierarchical higher order elements

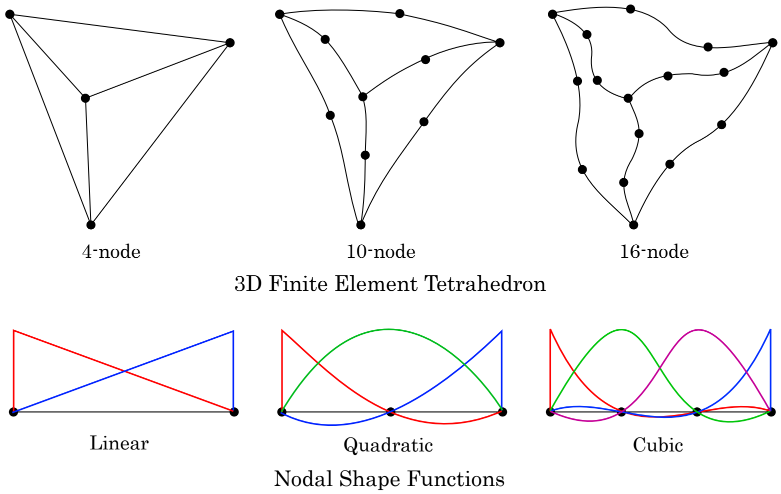

Figure 4-1: Higher order tetrahedron and their nodal shape functions

This section highlights the difference between higher order elements and hierarchical higher order elements. Like higher order interface elements, higher order finite elements (Figure 4-1(top)) are used to approximate fields such as displacement using higher order polynomial shape functions (Figure 4-1(bottom)) and to represent curved domains in the discretised finite element problem. The main disadvantage of this is that the finite element type determines the polynomial order of approximation. Varying the polynomial order within a finite element domain requires the use of serendipity elements and special re-meshing techniques, at a severe computational cost.

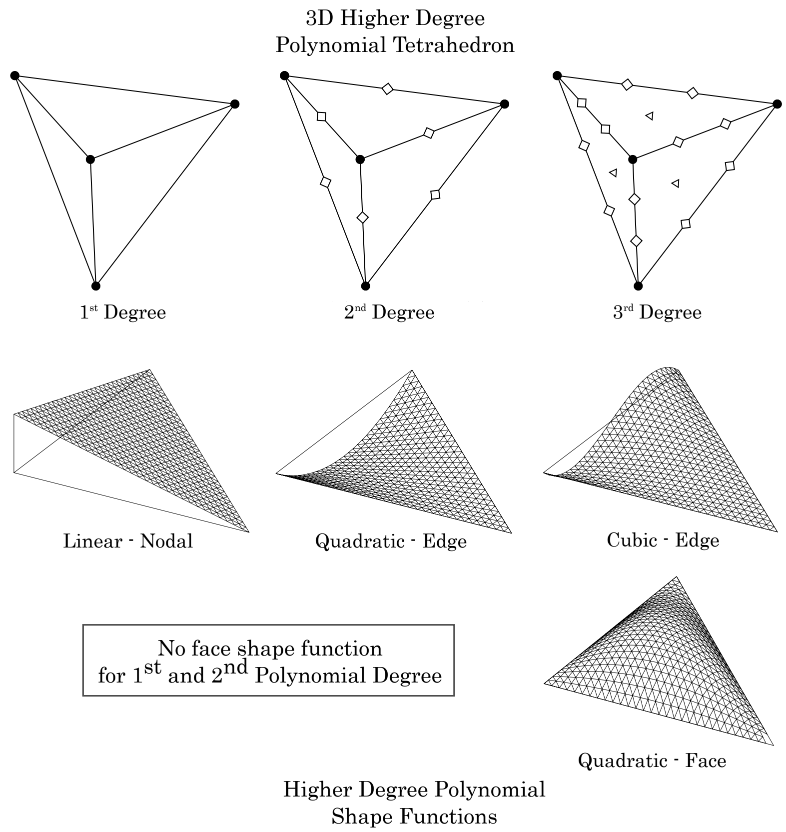

Figure 4-2: Linear tetrahedron with HO polynomial DOF and their nodal, edge and face shape functions[192]

On the other hand, hierarchical higher order elements consist of linear finite elements, with additional virtual degrees of freedom (DOF) assigned to edges, faces and volumes (Figure 4-2(top)), to approximate fields using HO basis functions (Figure 4-2(bottom)). This system is called hierarchical because every entity of a finite element can have a different polynomial order as necessary. However, it is worth noting that curved domains cannot be represented using hierarchical higher order finite elements. Additionally, complex data structures are required to store the polynomial order and orientation of every entity of a finite element, as discussed later in this chapter.

4.0.3 Different types of refinement

h-refinement is a simple approach whereby the element size h is increased or decreased without changing the finite element type. h-refinement can be achieved by subdividing existing elements (Figure 4-3c) or by re-meshing the domain of interest. Although h-refinement is easily adopted in the FEM, problems such as mesh quality (skewness of elements and large variation in area/volume ratio) and weak convergence are very common.

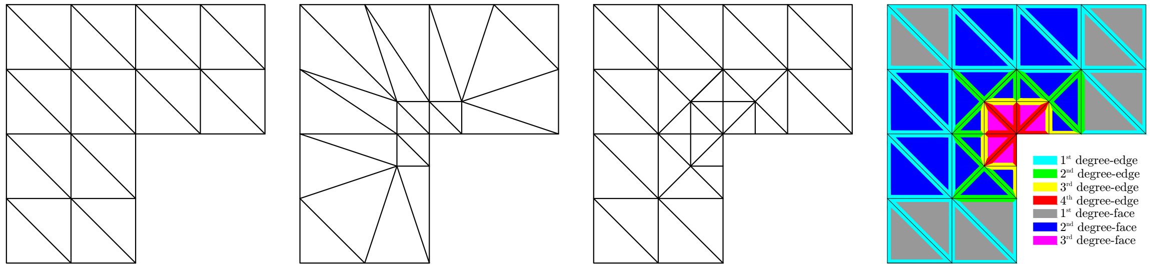

(a) no refinement (b) r-refinement (c) h-refinement (d) hp-refinement

Figure 4-3: Different types of refinement

r-refinement is a useful alternative to h-refinement, where the number of DOF is maintained and the mesh nodes are concentrated in zones that requires improved approximation (Figure 4-3b)), but the number of elements, DOFs or connectivity is not changed. This method could however be inappropriate where the mesh is already too coarse and/or the area or volume ratio of elements is very large.

p-refinement provides higher order approximation by increasing the order of approximation. In the traditional FEM, this is achieved by using higher order elements. Typically, the mesh does not change but physical nodes are added, e.g. a three node triangle becomes a six node triangle, or a four node tetrahedron becomes a ten node tetrahedron. As discussed in Section 2.2.3.5, enrichment methods to improve the approximation variable fields on the interface have been developed to accurately capture the de-bonding mechanism. In this thesis, a hierarchical higher order approximation technique will be used to perform localised p-refinement on both the FEs and interface elements.

hp-refinement is a mixture of non/-uniform h and p-refinement as shown in Figure 4-3d. Babuska and Guo[10] showed that hp-refinement provides an exponential rate of convergence $e^{-\kappa\sqrt{(\alpha-1/2)N}}$, where N is the total number of DOFs, α is a constant and κ is the exponent factor which can range from 1.24 for a uniform p-refinement and optimal geometrical mesh to 1.76 for an optimal non-uniform mesh. If an exponential rate of convergence is obtained, the problem is solved accurately using the minimum number of degrees of freedom and minimum computational power.

4.0.4 Localised hierarchical refinement

Localised refinement reduces the total number of degrees of freedom (DOFs) without diminishing the accuracy of the numerical solution. This is performed by decreasing or increasing the number of DOFs on various zones in the FE mesh (Figure 4-3(d)), depending on whether the level of approximation is sufficient to achieve a prescribed numerical accuracy in the entire model. The decrease/increase of DOFs is performed by pre-defining or adaptively localising refinement (such as h- or p-refinement) throughout the model. Error estimators are used in determining the order of approximation required for every entity in the finite element mesh and provide sufficiently accurate results.

While h-refinement is easily implemented, it is not efficient in improving the solution accuracy. P-refinement is more flexible and adaptable to different degree of non-linearity. However, using higher order elements can be complex and typical elements with a third order of approximation or higher are not implemented in finite element codes; hence, hierarchical HO p-refinement may be more effective when different approximation orders are required.

4.1 Hierarchical p-approximation

This section provides a step by step explanation of how hierarchical higher order approximation is implemented in a FE context where cohesive elements are used. The construction of the hierarchical HO shape functions will be explained for tetrahedral/triangular elements based on the work of Ainsworth and Coyle[2]. The implementation of hierarchical HO shape functions satisfies a priori conformity of shape functions, explained in Subsection 4.1.2. This is followed by a description of the efficient and flexible numerical integration procedure proposed in this work, explained in Subsection 4.1.3 and implemented in MoFEM.

4.1.1 Construction of shape functions

In standard FE approximation, degrees of freedom are associated with physical nodes on the vertex, edge and face. To increase the order of approximation, the old nodes need to be removed and new nodes added in the appropriate position. This does not permit hierarchical approximation functions to be constructed. For hierarchical HO elements, degrees of freedom are associated with both physical vertex nodes and with entities such as edges, faces and volumes. This enables us to construct the hierarchical approximation basis. This also allows for a convenient construction of a heterogeneous order of approximation where the order can be defined independently for each entity. Following the work of Ainsworth and Cole[2], the hierarchical approximations are provided by the Legendre polynomials for a reference interval $l = [-1; 1]$, are expressed as

$$L_0(s) = 1; \quad L_1(s) = s; \quad L_{l+1}(s) = \frac{2l+1}{l+1} s L_l(s) - \frac{l}{l+1} L_{l-1}(s), \quad l = 1, 2, \cdots \tag{4.1}$$

where L_l is the Legendre polynomial of degree l. Legendre polynomials are a special case of the Gegenbauer polynomials as a case of the generalised Humbert polynomials[94].

For a 1D edge, the linear shape functions are given as

$$N_o = 1 - \xi \quad N_i = \xi \tag{4.2}$$

For a 2D triangular face they are

$$N_o = 1 - \xi - \eta \quad N_i = \xi \quad N_j = \eta \tag{4.3}$$

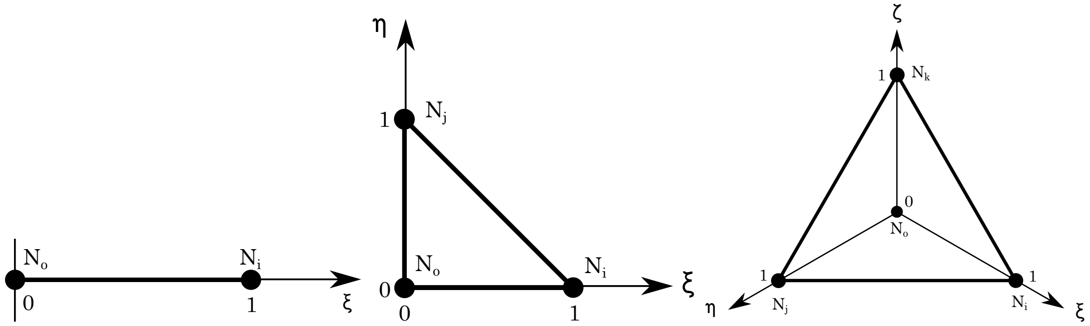

Figure 4-4: 1D edge / 2D triangle / 3D tetrahedron Isoparametric Elements

For a 3D tetrahedron volume they are

$$N_o = 1 - \xi - \eta - \zeta \quad N_i = \xi \quad N_j = \eta \quad N_k = \zeta \tag{4.4}$$

where ξ, η and ζ are the local coordinates.

Once the linear edge shape functions (Equations 4.2-4.4) and the Legendre polynomials 4.1 are determined, the shape functions for the extra DOFs can be computed as shown in Figure 4-5.

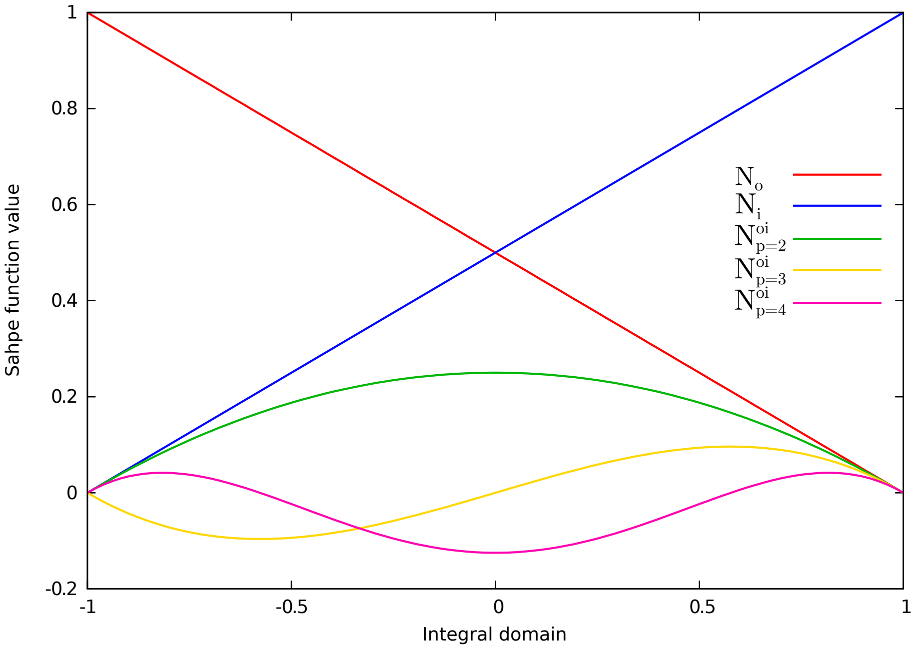

Figure 4-5: Nodal and higher order shape functions for an edge

Edge hierarchical higher order shape functions are:

$$N_l^{oi} = \beta_{oi} L_l(s_{oi}), \qquad 0 \le l \le p-2 \tag{4.5}$$

Face hierarchical higher order shape functions are:

$$N_{lm}^{oij} = \beta_{oij} L_l(s_{oi}) L_m(s_{oj}), \qquad 0 \le l, m, l+m \le p-2 \tag{4.6}$$

Tetrahedron hierarchical higher order shape functions are:

$$N_{lmn}^{oijk} = \beta_{oijk} L_l(s_{oi}) L_m(s_{oj}) L_n(s_{ok}), \qquad 0 \le l, m, n, l+m+n \le p-4 \tag{4.7}$$

where $\beta_{oi} = N_o N_i$, $\beta_{oij} = N_o N_i N_i$, etc., and $s_{oi} = N_i - N - o$, $s_{oj} = N_j - N_o$, etc., and l, m, n are the polynomial degree, and p is the polynomial order.

The quantity of DOFs generated for a certain polynomial order p for edges, faces and tetrahedrons is as follows:

$$\mathrm{DOF}_{edge} = p-1 \qquad \mathrm{DOF}_{face} = (p-2)(p-1)/2 \qquad \mathrm{DOF}_{tet} = (p-3)(p-2)(p-1)/6 \tag{4.8}$$

As shown in Figure 4-6, hierarchical HO shape function for edges and faces should conform with the neighbouring entities. Hence, when computing β and s, the indices o, i, j should respect the orientation sense of the entity derived from the canonical order of connectivity of the finite elements[203].

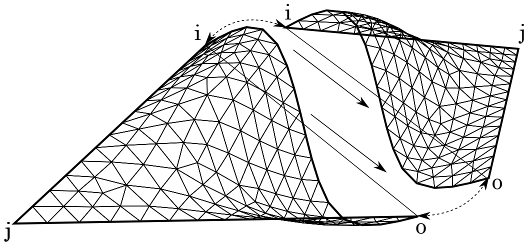

Figure 4-6: Conforming face shape function

Examples of linear (polynomial order p=1), quadratic (p=1) and cubic (p=2) edge shape functions are shown in Figures 4-7, 4-8 and 4-9 respectively. Quartic (p=3) and cubic (p=4) face shape functions are shown Figure 4-10.

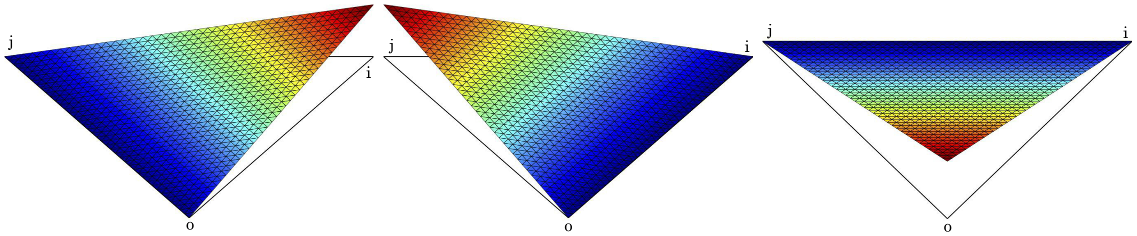

Figure 4-7: Linear edge shape functions: $0 \leq N_{p=1}^{oi,ij,jo} \leq 1$

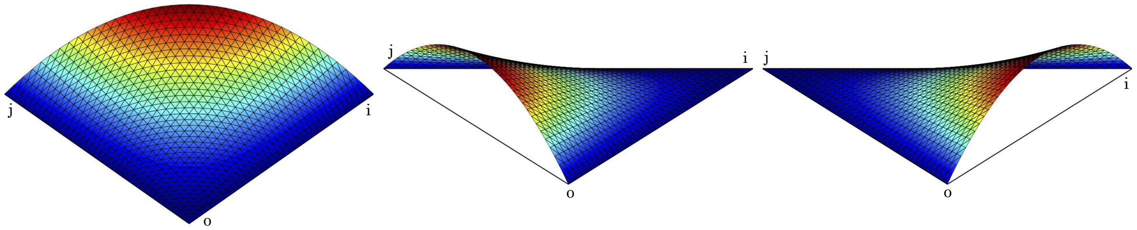

Figure 4-8: Quadratic edge shape functions: $0 \leq N_{p=2}^{ij,jo,oi} \leq 0.25$

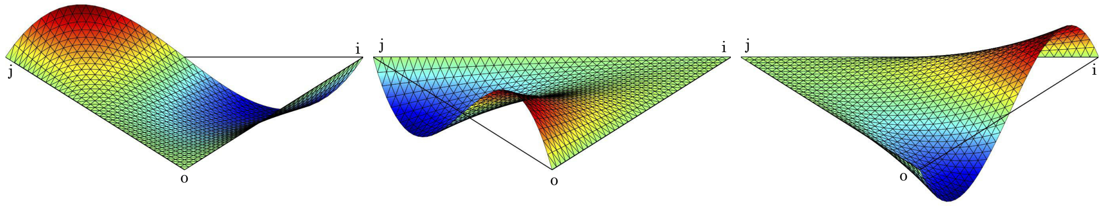

Figure 4-9: Cubic edge shape functions: $0 \leq N_{p=3}^{ij,jo,oi} \leq 0.125$

4.1.2 Enforcing conformity in 2D/3D hierarchical higher order p-approximation

The main advantage of using hierarchical higher order shape functions is the ability to locally enhance the order of approximation to achieve accurate results with the minimum computational cost. This implies that a different number of higher order

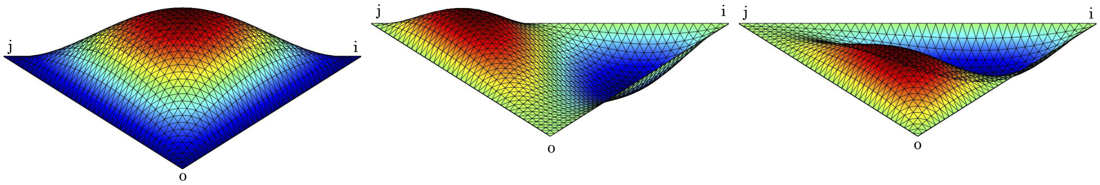

Figure 4-10: Left: Quadratic ($N^{oij}_{p=3}$); middle and right ($N^{ioj,ijo}_{p=4}$) face shape functions

DOF are assigned to every mesh entity, and there is consequently different order of approximation for every entity.

Enforcing conformity of shape functions and having adequate numerical integration are two essential conditions when using hierarchical HO p-approximation. The latter topic will be discussed in Section 4.1.3, but enforcing conformity of HO shape function in 2D and 3D will be discussed in this section. Conformity is ensured by using same approximation order (Figure 4-11) and same node ordering (Figure 4-12) for edges and faces when shared between two more than finite elements[2].

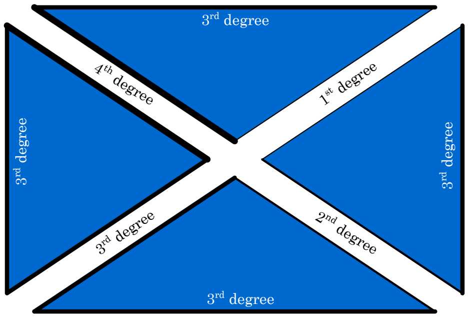

Figure 4-11: Matching of degree of polynomial in 2D (localised p-refinement)

For example, evaluating the edge shape functions for two neighbouring triangles should obtain same values for that shared edge as shown in Figure 4-13(right). If a correct approximation order is used, but with a different node ordering, non-conforming shape functions are generated with mismatched values as shown in Figure 4-13(left).

The key to practical implementation of the hierarchical HO element is the use of a database which retains information about the polynomial degree and orientation of each entity. This was made possible by the Mesh-Oriented database (MOAB) library, which stores and retrieves information of every mesh entity.

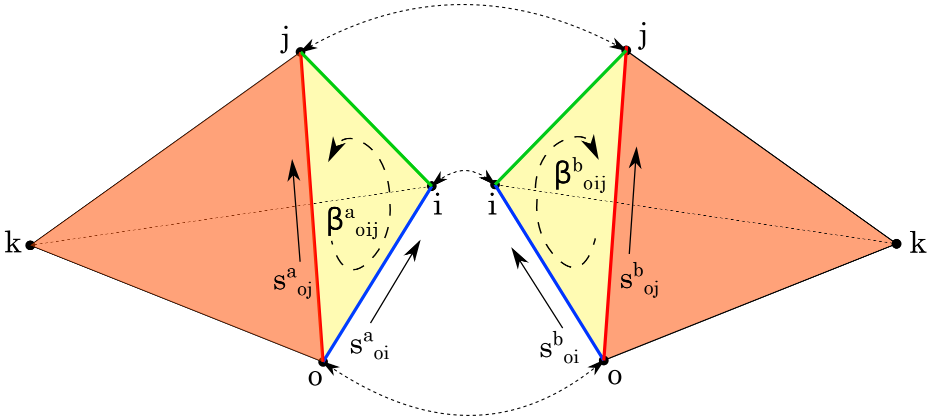

Figure 4-12: Conforming node ordering for a shared face

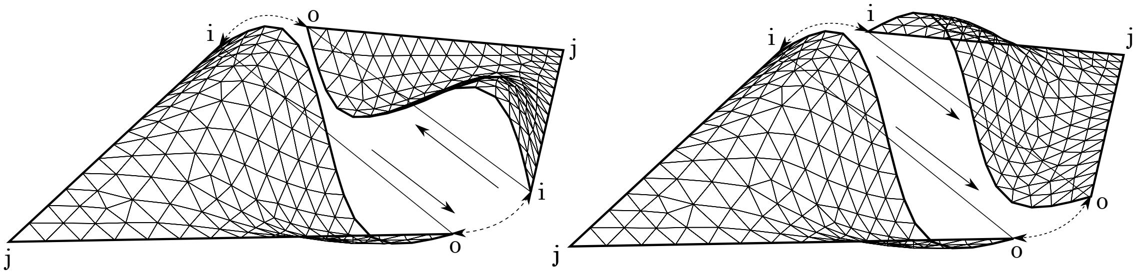

Figure 4-13: 2D Conformity
Left: mismatch shape function values (non-conforming geometrical sense)
Right: matching of shape function values (conforming geometrical sense)[2]

It is worth noting that node ordering may vary if retrieved from the finite element connectivity. An additional parameter is used to determine the sense of direction of an entity when queried for different finite elements. Consider the two triangles in Figure 4-13(left), where their connectivities are o, i and j respectively. If we compute the HO shape functions for edge oi for the left and right triangles, obtaining $N_p^{oi(left)}$ and $N_p^{oi(right)}$ respectively, we can conclude that $N_p^{oi(left)} \neq N_p^{oi(right)}$, on the other hand, $N_p^{oi(left)} = N_p^{io(right)}$ for $p > 2$. If we assign a positive and negative unit value to this edge when considered for the left and right triangle respectively, we can identify whether we have to reverse the node ordering or not when computing the HO shape functions.

4.1.3 Numerical Integration for hierarchical higher order approximations

Standard Gauss quadrature given as

$$\int_{-1}^{1} f(x)dx \approx \sum_{i=1}^{N} w_i f(x_i) \tag{4.9}$$

where $f(x)$ is the weak form function, w_i are the weight functions, x_i are the Gauss points and the number of Gauss points N is computed as

$$N = \frac{n!}{l! * (n-l)!} \tag{4.10}$$

It is possible to obtain an accurate integral with the correct number and position of Gauss points. An external library[35] based on the Grundmann and Moller integration rule[83] was used in MoFEM to dynamically compute the Gauss points and weight functions for any polynomial degree to increase computational efficiency. The number of Gauss points required is determined from Equation 4.10, where $n = d + l + 1$ (d is the dimensional space (1,2 or 3) and l is the polynomial degree).

4.2 Hierarchical higher order interface elements

The interaction modelling between the strands of the braided ropes and the rope and the surrounding concrete requires the use of interface elements. However, interface elements may require HO approximation due to localised deformations induced by large deformations and/or damage on the interface. Localised h- and p-refinement are generally used to achieve an accurate solution with the minimum number of DOFs. P-refinement (Figure 4-14) based on hierarchical HO approximation is an efficient process where additional HO DOFs are added to the system of equations without re-meshing or inserting physical HO nodes in the interface elements. Hence the polynomial order can be easily increased in areas of localised deformation, retaining a low polynomial order elsewhere.

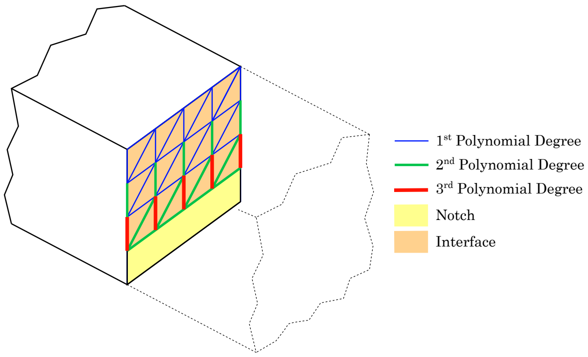

Figure 4-14: Localised p-refinement of edges on the interface

A well-known problem with interface elements[178] is the presence of spurious traction oscillations, commonly thought to be the result of incompatibility between the traction distribution along the interface and the stress distribution in the volume of the neighbouring elements. This Chapter investigates this phenomenon and proposes a solution.

4.2.1 Formulation of hierarchical higher order interface elements

A similar interface element formulation as that used by[183] was adopted to formulate hierarchical HO interface elements and is discussed in this Section. Unlike 6-noded or other HO interface elements, hierarchical HO interface elements can be used to perform localised p-refinement at the interface. Consequently, computational efficiency improves during de-lamination/fracturing problems.

An interface element is formed between solids (similar to Figure 4-15) by duplicating the nodes of the common surface, separating the solids into two parts and creating two independent surfaces. For notation purpose, one side is referred to as ‘positive’ and the other as ‘negative’ as shown in Figure 4-16. This means that any DOFs on the original common surface must be duplicated. Consider $\mathbf{X}$ and $\mathbf{x}$ to be the reference and current coordinates of the interface element with a displacement vector of $\mathbf{d}$, hence $\mathbf{x} = \mathbf{X} + \mathbf{d}$. Every interface element is composed of nodal and HO DOFs. For example, vector $\mathbf{x}$ is constructed from the nodal DOFs for the positive and negative sides of the interface and denoted by $^{[+/-]\gamma}$ respectively, then by the edges HO DOFs, denoted by $^{[+/-][1/2/3]\alpha}$ for the positive and negative sides and for the first, second and third edge respectively and ends with the face HO DOFs, denoted by $^{[+/-]\beta}$ as shown in Equation 4.11, where p is the polynomial order of the DOF.

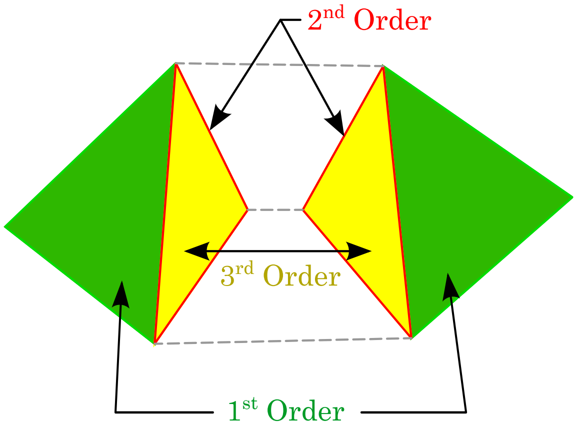

Figure 4-15: Localised p-refinement of interface and adjacent solid

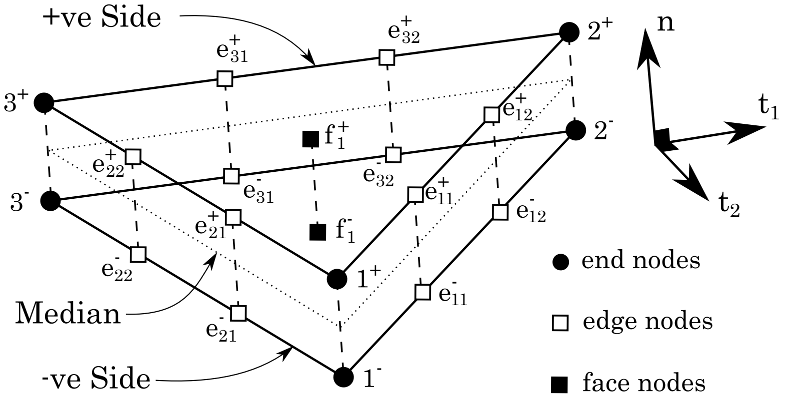

Figure 4-16: Cohesive elements represented with prisms in FE mesh

$$
\mathbf{x} = \begin{pmatrix}
x_x^{+\gamma}\ x_y^{+\gamma}\ x_z^{+\gamma}\ \ldots \\
(x_x^{+1\alpha}\ x_y^{+1\alpha}\ x_z^{+1\alpha})_p\ (x_x^{+2\alpha}\ x_y^{+2\alpha}\ x_z^{+2\alpha})_p\ (x_x^{+3\alpha}\ x_y^{+3\alpha}\ x_z^{+3\alpha})_p\ \ldots \\
(x_x^{+\beta}\ x_y^{+\beta}\ x_z^{+\beta})_p\ \ldots \\
x_x^{-\gamma}\ x_y^{-\gamma}\ x_z^{-\gamma}\ \ldots \\
(x_x^{-1\alpha}\ x_y^{-1\alpha}\ x_z^{-1\alpha})_p\ (x_x^{-2\alpha}\ x_y^{-2\alpha}\ x_z^{-2\alpha})_p\ (x_x^{-3\alpha}\ x_y^{-3\alpha}\ x_z^{-3\alpha})_p\ \ldots \\
(x_x^{-\beta}\ x_y^{-\beta}\ x_z^{1\beta})_p
\end{pmatrix} \tag{4.11}
$$

The traction resistance between interface elements is governed by their respective local stiffness matrix $\mathbf{D}_{loc}$. For an elastic interface element this is defined as

$$
\mathbf{D}_{loc} = \begin{bmatrix} D_n & & \\ & D_{t_1} & \\ & & D_{t_2} \end{bmatrix} \tag{4.12}
$$

- D_n - Normal Mode 1 stiffness
- D_{t1} - Tangential Mode 2 stiffness
- D_{t2} - Tangential Mode 3 stiffness

while for damage cohesive interface elements, the tangential operator $\mathbf{D}_{loc}$ is defined as the rate of traction with respect to the local relative gap opening $\Delta\mathbf{u}_{loc}$ given as

$$
\mathbf{D}_{loc} = \frac{\partial \mathbf{t}_{loc}}{\partial \Delta \mathbf{u}_{loc}} \tag{4.13}
$$

$$
and\ \ \mathbf{t}_{loc} = \begin{bmatrix} \frac{\partial \psi}{\partial \Delta u_n} \\ \frac{\partial \psi}{\partial \Delta u_{t_1}} \\ \frac{\partial \psi}{\partial \Delta u_{t_2}} \end{bmatrix} \tag{4.14}
$$

for cohesive interface elements (described in the following section). t_{loc} is the local traction computed from the respective damage energy function $\psi(\Delta u_n, \Delta u_{t1}, \Delta u_{t2})$. Δu_n, Δu_{t1} and Δu_{t2} are the relative gap openings of the interface in the normal and tangential components as discussed in Section 4.2.2. The damage energy function is governed by a traction-separation cohesive law as discussed in Section 4.2.2 and selected to represent the mechanical behaviour of a particular type of interface between two materials, such as the interface between steel reinforcement and concrete as addressed in Section 2.2.2.1. The local relative gap opening $\Delta\mathbf{u}_{loc}$ is determined from the global relative gap opening $\Delta\mathbf{u}_{glob}$ as

$$\Delta\mathbf{u}_{loc} = \mathbf{R}\Delta\mathbf{u}_{glob} \tag{4.15}$$

where $\mathbf{R}$ is the rotation matrix which transforms the interface element between the global and local coordinates, as described later in this section, and $\Delta\mathbf{u}_{glob}$ at every integration point is determined by

$$\Delta\mathbf{u}_{glob} = \mathbf{\Phi}\mathbf{d} \tag{4.16}$$

where $\mathbf{d}$ is the displacement at all the DOFs of the interface element and $\mathbf{\Phi} = \mathbf{N}(\mathbf{I}_{3\gamma+(9\alpha+3\beta)p} \mid -\mathbf{I}_{3\gamma+(9\alpha+3\beta)p})$, where $\mathbf{I}$ is an identity matrix with a variable size of $3\gamma + (9\alpha + 3\beta)p$, depending on the hierarchical HO approximation order, and consequently on the number of DOFs for a particular interface. $\mathbf{N}$ is the shape function matrix defined as follows and composed of nodal shape functions (Equations 4.3) and the higher order edges $(1 - 3\alpha)$ and face (β) shape functions (Equations 4.5 and 4.6 respectively).

$$\mathbf{N}_{3\times(3\gamma+(9\alpha+3\beta)p)} = \Big(N_{\gamma}\mathbf{I}_{3\times3} \mid N_{1\alpha p}\mathbf{I}_{3\times3} \mid N_{2\alpha p}\mathbf{I}_{3\times3} \mid N_{3\alpha p}\mathbf{I}_{3\times3} \mid N_{\beta p}\mathbf{I}_{3\times3} \Big) \tag{4.17}$$

Similar to the local and global relative displacements ($\Delta\mathbf{u}_{loc}$ and $\Delta\mathbf{u}_{glob}$), $\mathbf{D}_{loc}$ defined in the local coordinate system has to be rotated in the global coordinate system, such as

$$\mathbf{D}_{glob} = \mathbf{R}^T\mathbf{D}_{loc}\mathbf{R} \tag{4.18}$$

and therefore the global stiffness matrix of the interface element can be computed as

$$\mathbf{K}_{el} = \int \left(\mathbf{\Phi}^T \left[\mathbf{R}^T\mathbf{D}_{loc}\mathbf{R}\right] \mathbf{\Phi}\right) dA = \sum_{i}^{n}\sum_{j}^{n} \omega_i\omega_j \left(\mathbf{\Phi}^T \left[\mathbf{R}^T\mathbf{D}_{loc}\mathbf{R}\right] \mathbf{\Phi}\right) J \tag{4.19}$$

and the internal force vector of the interface element can be computed as

$$\mathbf{f}_{el}^{int} = \int \boldsymbol{\Phi}^T \left[\mathbf{R}^T \mathbf{t}_{loc}\right] dA = \sum_{i}^{n} \sum_{j}^{n} \omega_i \omega_j \boldsymbol{\Phi}^T \left[\mathbf{R}^T \mathbf{t}_{loc}\right] J \tag{4.20}$$

In Equations 4.19 and 4.20, J is the determinant of the Jacobian and equivalent to the area of the interface when three nodes exist on each side of the interface.

When adaptive p-refinement is undertaken as shown in Figures 4-14 and 4-15, the order of approximation of every entity (edges and face) is stored and $\mathbf{N}$ can be formulated accordingly. It is important that conformity is ensured between any pair of entities (a pair of edges or face on the $+ve$ and $-ve$ side), similar to the description given in Section 4.1.2.

The rotational matrix $\mathbf{R}$ is made from the normalised normal vector ($\hat{\mathbf{n}} = \hat{\mathbf{t}}_1 \times \hat{\mathbf{t}}_2$) and the two tangential vectors ($\hat{\mathbf{t}}_1$ and $\hat{\mathbf{t}}_2$)(Equations 4.22-4.23) of the median surface as shown in Figure 4-16. The coordinates of the median surface which is the average of the nodal coordinates of both sides (+ve and -ve sides) is $\bar{\mathbf{x}} = \frac{1}{2}[\mathbf{x}^{+\gamma} - \mathbf{x}^{-\gamma}]$. In a large displacement formulation (see Section 5.5), $\mathbf{R}$ has to be updated at every load increment w.r.t. the current configuration. $\frac{\partial \bar{\mathbf{x}}}{\partial \xi}$ and $\frac{\partial \bar{\mathbf{x}}}{\partial \eta}$ can be computed using Equation 4.24 and 4.25.

$$\mathbf{R} = \begin{bmatrix} \hat{\mathbf{n}} \\ \hat{\mathbf{t}}_1 \\ \hat{\mathbf{t}}_2 \end{bmatrix} \tag{4.21}$$

$$\hat{\mathbf{t}}_1 = \frac{1}{\|\frac{\partial \bar{\mathbf{x}}}{\partial \xi}\|} \frac{\partial \bar{\mathbf{x}}}{\partial \xi} \tag{4.22}$$

$$\hat{\mathbf{t}}_1 = \frac{1}{\|\frac{\partial \bar{\mathbf{x}}}{\partial \eta}\|} \frac{\partial \bar{\mathbf{x}}}{\partial \eta} \tag{4.23}$$

$$\frac{\partial \bar{\mathbf{x}}}{\partial \xi} = \frac{\partial \mathbf{N}}{\partial \xi} \bar{\mathbf{x}} \tag{4.24}$$

$$\frac{\partial \bar{\mathbf{x}}}{\partial \eta} = \frac{\partial \mathbf{N}}{\partial \eta} \bar{\mathbf{x}} \tag{4.25}$$

Linearisation of the interface element formulation was necessary for cohesive damage laws (explained in the next section). The internal force of the current load increment $i+1$ is computed as:

$$\mathbf{f}_{i+1}^{int} = \mathbf{f}_{i}^{int} + \frac{\partial \mathbf{f}_{i}^{int}}{\partial \Delta \mathbf{u}_{loc}} \delta x \tag{4.26}$$

where the tangent stiffness matrix $\mathbf{K}_T$ is

$$\mathbf{K}_T = \frac{\partial \mathbf{f}_{i}^{int}}{\partial \Delta \mathbf{u}_{loc}} = \frac{\partial}{\partial \Delta \mathbf{u}_{loc}} \int \mathbf{\Phi}^T \left[\mathbf{R}^T \mathbf{t}_{loc} \right] dA \tag{4.27}$$

and can be expanded as

$$\mathbf{K}_T = \int \mathbf{\Phi}^T \left[\frac{\partial \mathbf{R}}{\partial \Delta \mathbf{u}_{loc}} \right]^T \left[\mathbf{t}_{loc} \right] dA + \int \mathbf{\Phi}^T \mathbf{R}^T \left[\frac{\partial \mathbf{t}_{loc}}{\partial \Delta \mathbf{u}_{loc}} \right] dA \tag{4.28}$$

If the interface experiences small rotations, we can simplify $\mathbf{K}_T$ as

$$\mathbf{K}_T = \int \mathbf{\Phi}^T \mathbf{R}^T \left[\frac{\partial \mathbf{t}_{loc}}{\partial \Delta \mathbf{u}_{loc}} \right] dA \tag{4.29}$$

where $\frac{\partial \mathbf{t}_{loc}}{\partial \Delta \mathbf{u}_{loc}}$ is the tangent operator $\mathbf{D}_{loc}$ defined earlier in Equation 4.13. Assuming that the interface experiences small rotations, $\mathbf{K}_T$ expressed in Equation 4.29 was in this thesis. The residual $\mathbf{F}_{res}$ then can be computed as $-\mathbf{F}_{res}(x) = \mathbf{K}_T \delta x$, and used in a Newton-Raphson algorithm to solve the non-linear problem. Newton-Raphson was controlled using arc-length method, where the incremental load was controlled by the gap opening of the crack front as proposed by[5].

4.2.2 Cohesive elements

This section discusses cohesive elements used to modelled de-bonding between fibres and concrete (see Chapter 6). Cohesive elements are interface elements governed by a traction/separation law, also referred to as a cohesive law.

Consider a model made from two laminates bound with a layer of glue (Figure 4-17). During de-lamination, the model experiences a mechanical resistance governed by a cohesive law. Cohesive laws vary from elastic models, providing uniform stiffness across the interface without any damage (Figure 4-18(a)), to models that lose stiffness as the gap increases between the interface (damaging) (Figure 4-18(b-d)). Gap opening of the interface is classified into three modes: normal opening (Δu_n), in plane shear (Δu_{t_1}), and out of plane shear (Δu_{t_2}) as shown in Figure 4-19(a-c)[129]. The combination of gap openings governs the cohesive law, as will later be discussed. For example, the de-lamination problem (Figure 4-17) is mainly governed by Mode I gap opening, while fracturing of concrete can be governed by all modes of separation.

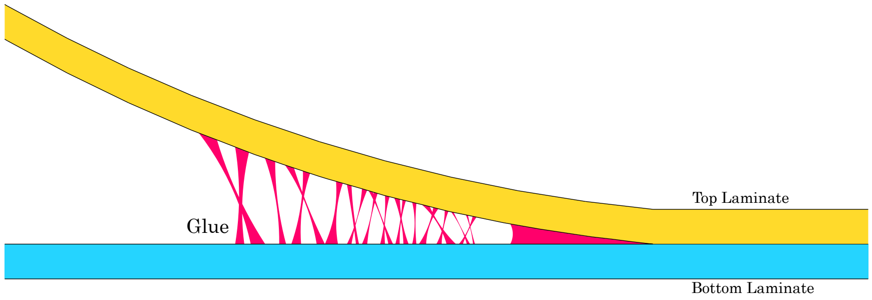

Figure 4-17: Fibrous glue (cohesive zone) between two laminates

In this thesis, de-bonding between fibres and concrete was assumed to damage linearly and can therefore be represented by a linear cohesive model. The implementation of the linear cohesive model is explained in this section.

A cohesive law governing the mechanics of an interface element is divided into four main parts as shown in Figure 4-20. The first loading stage of the interface is where

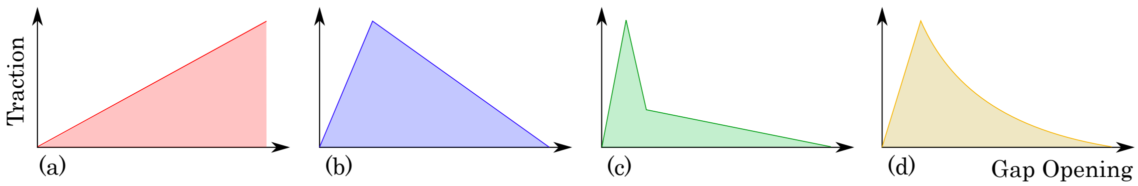

Figure 4-18: Cohesive Laws: (a) Elastic (no damage); (b) Linear damage; (c) Bi-linear damage; (d) Exponential damage

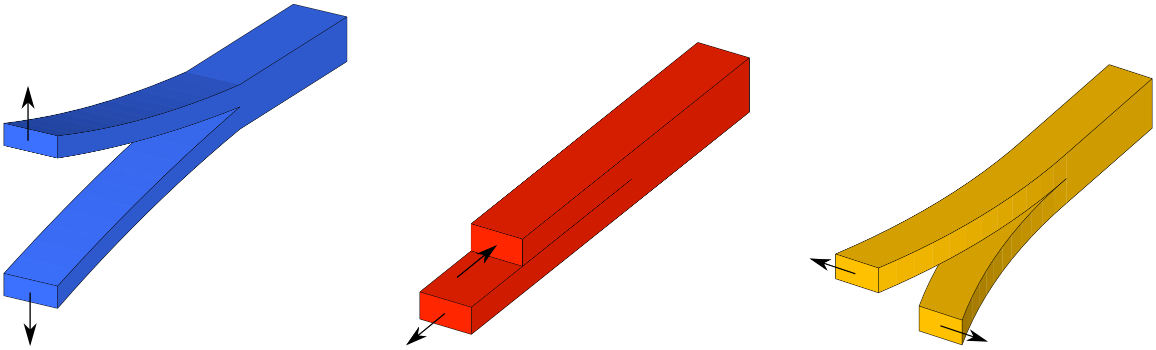

(a) Mode I - Normal opening

(b) Mode II - In plane shear

(c) Mode III - Out of plane shear

Figure 4-19: Modes of cohesive elements

a penalty stiffness E_o across the interface is used to incrementally determine the maximum internal forces of the interface. Once the maximum traction f_t is obtained, the damaging phase is initiated. Traction resistance is governed by the gap opening $\kappa = max(\kappa, g - g_o)$, where g is the mixed-mode gap opening as discussed later in this section, and $g_o = \frac{f_t}{E_o}$. The damage parameter ω is equal to zero if $\kappa = 0$ and is equal to one if $\kappa = \kappa_1$ ($g = g_{max}$) and the damage energy G_f is fully dissipated. G_f, also known as Griffith energy, is equal to the area under the damaging phase of the cohesive law (Figure 4-20). While g reduces during unloading, κ remains unchanged and g_o is updated to the point at which the unloading was initiated. The third part of a cohesive law is the re-loading of the interface element using the updated stiffness computed from the new g_o and damaging will be continued as the maximum traction at the new g_o is achieved. Once full damage is achieved ($\omega = 1$), that is $\kappa = \kappa_1$, and $\kappa_i = \frac{2G_f}{f_t}$, the fourth stage is initiated where full damage is obtained and no gap recovery is possible. Post damage friction can be obtained by introducing a cohesive-frictional interface law that considers a constant frictional stress when $\kappa \geq \kappa_1$. However, the influence of confinement on the bond stress-slip response is not taken into account by this approach. Therefore, a unilateral contact can be obtained by introducing high penalty stiffness in mode I[6].

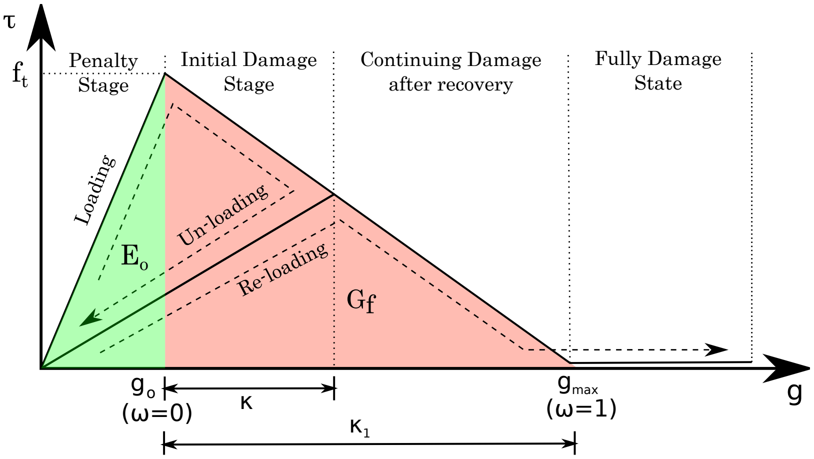

Figure 4-20: Linear damage model with full recovery during un-loading/re-loading

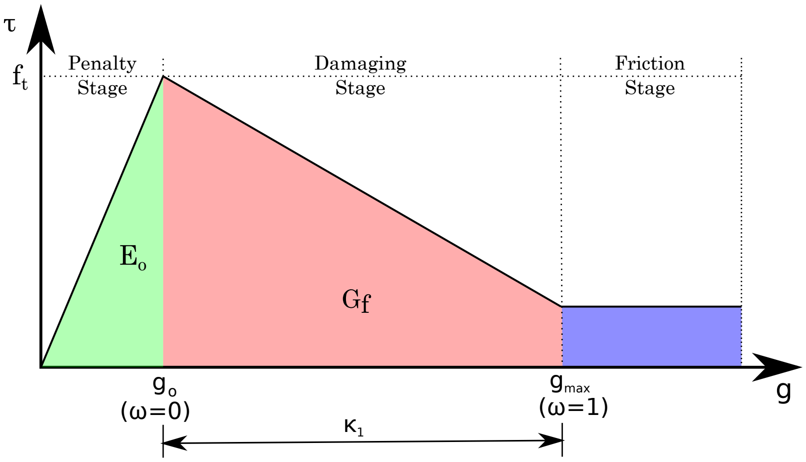

Figure 4-21: Linear damage model with friction

The traction resistance of the interface τ can be expressed as

$$\boldsymbol{\tau} = \begin{cases} \mathbf{E}_o\mathbf{g} & \kappa = 0 \qquad (4.30) \\ (1-\omega)\mathbf{E}_o\Delta\mathbf{u} & 0 < \kappa \leq \kappa_1, \qquad (4.31) \end{cases}$$

where ω is given as

$$\omega = \frac{(2G_f E_o + f_t^2)\kappa}{2G_f(f_t + \kappa E_o)} \tag{4.32}$$

As discussed in Section 4.2.1, the energy damage function depends on a combination of normal, in plane shear and out of plane gap opening (Δu_n, Δu_{t_1} and Δu_{t_2} respectively). In this thesis g, which governs the damage law, was expressed as

$$g = \sqrt{(\Delta u_n)^2 + \beta((\Delta u_{t_1})^2 + (\Delta u_{t_2})^2)} \tag{4.33}$$

where β determines whether modes II and III will contribute to the damage model. Unlike the de-bonding discussed in Section 2.2.1 where the bond-slip model for steel reinforced concrete is mainly governed by the slip along the reinforcement, in braided fibre reinforced concrete, the fibre cross-section reduces significantly and therefore mixed-mode dislocation is considered. In the examples given in Chapter 6, it was assumed that the de-bonding between fibres and concrete during pull-out is governed by the normal and shear dislocation. Therefore Mode II and III were fully activated by setting β equal to one (β can range from zero to one, depending on the contribution of tangential slip to the damage model).

Hierarchical higher order cohesive elements were implemented in MoFEM and these are represented by zero thickness prism elements that can be inserted between tetrahedron elements where fissures are pre-determined. Hierarchical higher order cohesive elements ensure that non-linearity are approximated accurately within every interface element.

In the following Section 4.2.3, de-lamination of a 3D laminate model identical to the experimental model investigated by Robinson and Song[167] and an equivalent 2D finite element model analysed by Alfano and Crisfield[5] is studied using uniform h and p-refinement, along with localised p-refinement at the interface using the formulation for p-refinement discussed in this section. This was utilised to investigate traction oscillations generated nearby notches using a four-point bending test of a 3D notched beam equivalent to the 2D beam used by Schellekens and deBorst[178] to investigate the same problem.

4.2.3 Beam de-lamination problem

This section investigates implementation in a typical problem, consisting of a mechanical de-lamination of two plies glued together. In Robinson and Song[167], a conventional laminate with fibres oriented in the longitudinal direction with material properties given in Table 4.1 and a bond area of $30 \times 100mm$ was experimentally investigated where the fracture energy G_f in Mode I ($G_{f,I}$) was determined. Alfano and Crisfield[5] analysed this problem via a 2D finite element approach, using the same dimensions given in Figure 4-22 and same material parameters given in Table 4.1, but with different penalty stiffness E_o as described later in this section.

In this thesis, the same problem is presented in a 3D finite element model using the proposed hierarchical higher order interface elements. It investigates the difference between h and p-refinements. To reduce the problem size, a quarter strip of this laminate was investigated (Figure 4-22). Linear damage cohesive elements (parameters given in Table 4.1) between the laminates were also used. The loading was controlled by Newton-Raphson method and governed by arc-length, controlled by the gap opening of the crack front[5]. The specimen was clamped at one end and, similar to the experimental and 2D numerical model, a $30mm$ zero thickness notch was introduced to the other end. The specimen was discretised with a structured tetrahedral mesh. Interface elements were also structured and aligned in parallel with the loading edges. This improved the non-linear convergence due to uniform damaging of the interface with minimal damage oscillation effects. The same boundary conditions were used as those in the experimental and 2D numerical investigations.

The penalty stiffness $E_o = \frac{f_t}{g_i}$ was reduced from that used by Alfano and Crisfield[5] to improve the rate of convergence as damaging phase is initiated. The effect of E_o was only on the linear loading part of the load-displacement graph, as shown in Figure

Composite Laminate Material

$E_p = 7.5GPa$	$E_z = 126GPa$	$G_{zp} = 49.88GPa$	$\nu_p = \nu_{pz} = 0.263$

Interface

$G_{f,I} = 0.281kJ/m^2$	$g_i = 2.047e-3mm$	$f_t = 57MPa$

Table 4.1: Laminate material and interface parameters

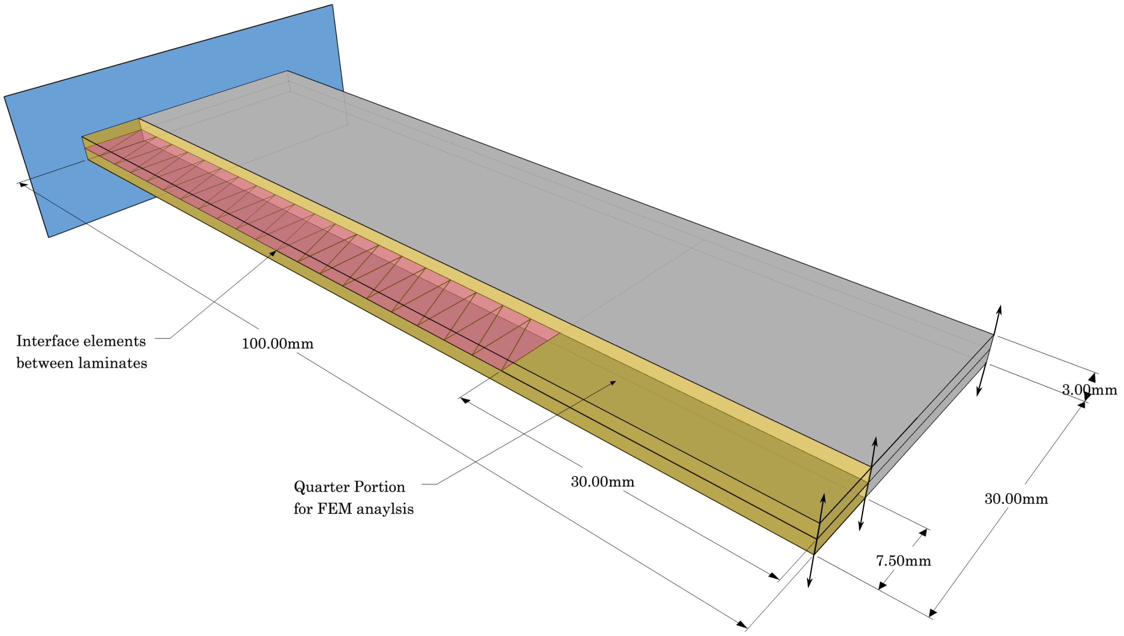

Figure 4-22: Diagram of de-lamination beam model

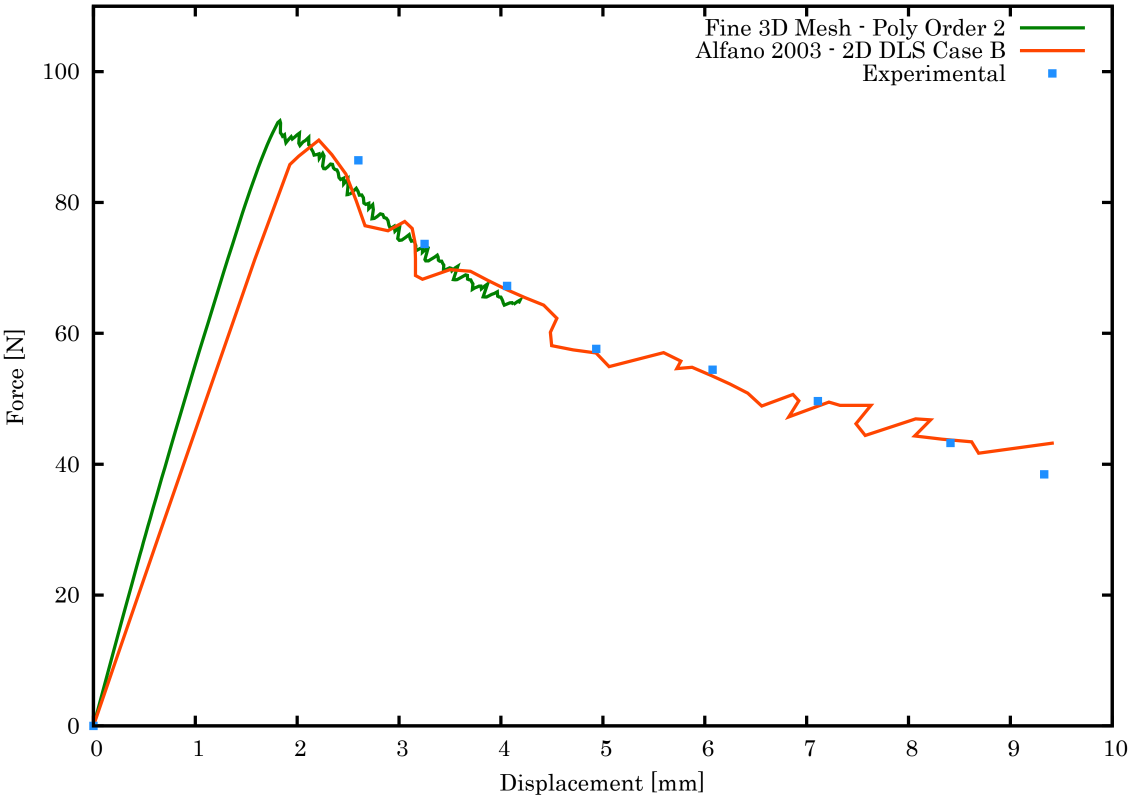

Figure 4-23: Comparison of 2D[5], 3D FEM solutions and experimental results[167]

4-23. This graph demonstrates good agreement between the 2D numerical results[5], the 3D numerical investigation using quadratic polynomial approximations and the experimental results[167]. In the 3D model, Newton-Raphson was controlled by the arc-length method where the load increment was dependent on the gap opening of the crack front of the de-lamination[5]. This ensures a good rate of convergence throughout the delamination process. Loading oscillations during de-lamination of the triangular interface elements were observed. This was due to a non-uniform damaging along the crack width front of the de-lamination. Due to these oscillations, the rate of convergence was reduced and a significant number of load steps were required to achieve a 4mm de-lamination as shown in Figure 4-23.

The aim of this part of thesis was to investigate the use of hierarchical higher order approximation for both the interfaces and solids. A series of tests were conducted, these included uniform h and p-refinement for both interfaces and solids, and localised p-refinement at the interface only. The advantages of these types of refinements in modelling de-lamination problems were studied. The smallest problem with a linear approximation in the solids and interface had 901 DOFs, while the largest problem with a quadratic approximation in the solids and quintic approximation at the interface had 13,789 DOFs.

Mesh (h-) refinement was conducted in three stages: coarse, medium and fine densities, having 40, 60 and 80 interface elements respectively. Up to cubic (3^{rd} order) polynomial approximation was used. Figure 4-24 shows the results of delamination process subjected to h-refinement. While interface damage oscillation was reduced as the mesh was refined, convergence to the exact solution is very slow. This was due to linear finite elements which experience shear locking and therefore extra bending stiffness. At least quadratic polynomial approximation on a medium mesh (6,211 DOFs) was required to converge to the accurate solution. It can be observed that cubic approximation on a coarse mesh (12,265 DOFs) is not as good as a 2^{nd} PO medium mesh (6,211 DOFs) although it has twice as many DOFs. This is clear evidence that a combination of h and p-refinement gives the most accurate solution with the least number of DOFs. Error estimators such as the hp-interpolation error estimator[54] can be used to determine the optimal hp-refinement. The theory suggests that an exponential convergence should be achieved if adaptive hp-refinement is used[11;54]. In similar cases, where the geometrical aspect ratio is large due to the thickness of the laminate, mesh quality constrains the possibilities of localised h-refinement at the interface[116].

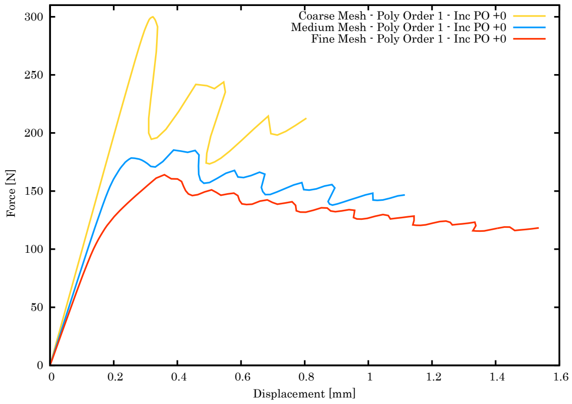

Figure 4-24: h-refinement 1^{st} PO approximation

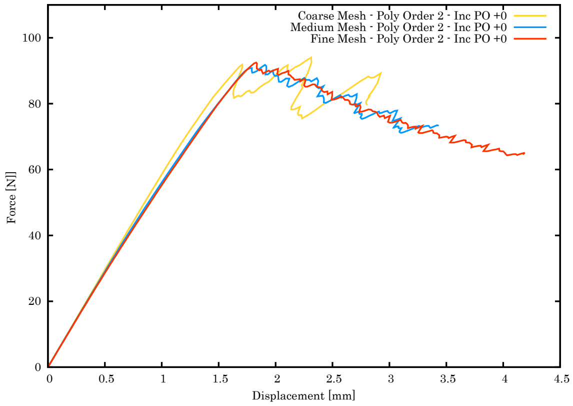

Figure 4-25: h-refinement of 2^{nd} PO approximation

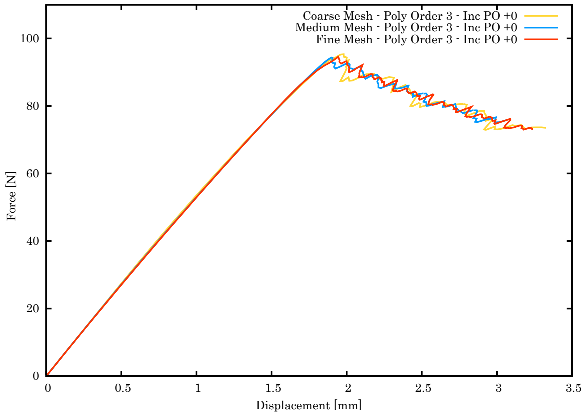

Figure 4-26: h-refinement of 3^{rd} PO approximation

Another approach would be to perform localised p-refinement at the interface as shown in the following study. A series of tests of the de-lamination problem with three levels of h-refinement and four levels of p-refinement at this interface were conducted. Localised p-refinement has to meet the conformity condition, discussed in Section 4.1.2, where the same polynomial order on both sides of the interface has to be used to achieve matching shape functions.

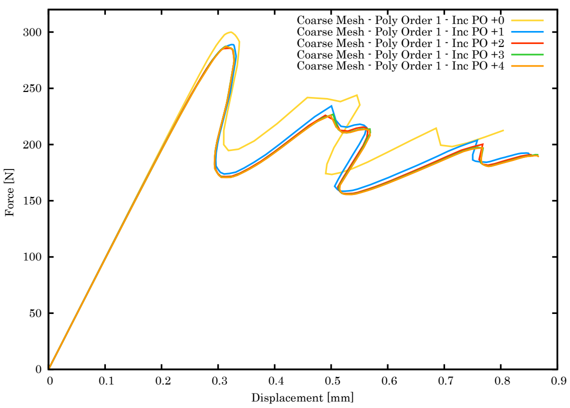

Figure 4-27: 1^{st} PO approx. of solids elements in coarse mesh

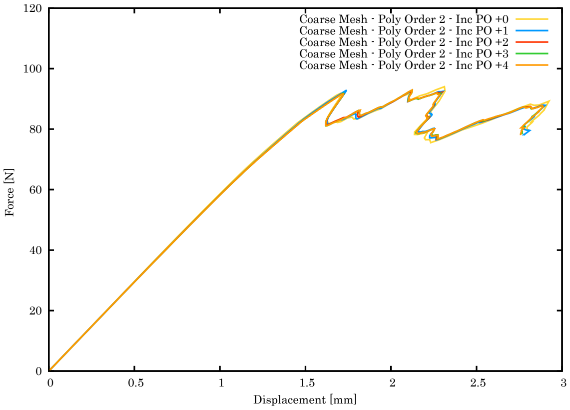

Figure 4-28: 2^{nd} PO approx. of solids elements in coarse mesh

By observing localised p-refinement on a coarse mesh (Figures 4-29, 4-30), quadratic approximation in the solid was required to prevent shear locking, while an increase of p at the interface had a small difference on the overall result, especially when 2^{nd} PO was used for the interface. This is a quick and good preliminary test to determine whether localised p-refinement at the interface improves the solution or not. After this test, the next option to improve the numerical solution is to rely on hp-refinement. While h-refinement alone is not enough (Figure 4-29), in combination with p-refinement (Figure 4-30), a good approximation of the solution can be obtained. On the other hand, as has been previously discussed, further localised p-refinement on the interface of the medium dense mesh was redundant and is not recommended for problems similar to this one. Further h-refinement (fine mesh) improved the solution when 2^{nd} PO was used for the finite and interface elements (Figure 4-32(b)). Although results become smoother when h-refinement is conducted on a model with linear polynomial approximation (Figure 4-27, 4-29 and 4-32(a)), the solution was far from converged.

This study shows how hierarchical higher order approximation can be used not only to perform uniform p-refinement, but also to conduct localised p-refinement on a set of entities. This section has shown that this methodology can be used to perform localised p-refinement on the interface elements, although results shows that uniform quadratic p-refinement on both the finite and interface elements was sufficient due to the nature of the problem studied. Using the formulation discussed and implemented

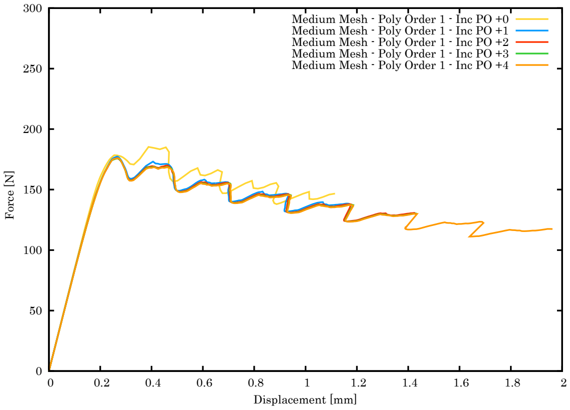

Figure 4-29: 1^{st} PO approx. of solids elements and various p-refinements at the interface in medium mesh

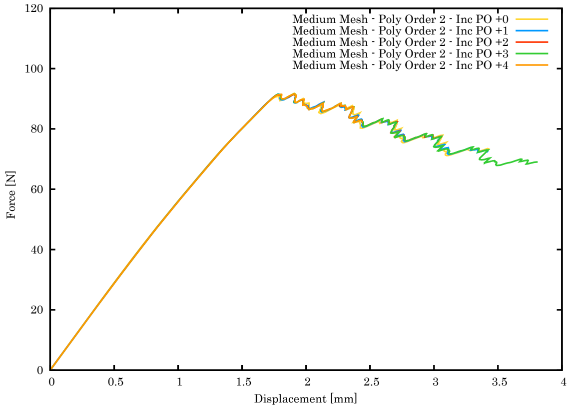

Figure 4-30: 2^{nd} PO approx. of solids elements and various p-refinements at the interface in medium mesh

according to Section 4.1 in MoFEM[110], the study shows that localised p-refinement is easy to achieve. MoFEM is a parallel multi-physics FEM C++ library that can perform h-, p- and hp-refinement[110] and take advantage of renowned libraries such as PetSc (Portable, Extensible Toolkit for Scientific Computation)[13] and MOAB (Mesh Oriented Database)[204]. At a user level, this is done by specifying the PO of approximation for every entity in the model (edges, faces and volumes). The embedded algorithm takes care of building the appropriate strain-displacement matrix that contains all the higher order DOFs which do not belong to any physically attached to physical nodes.

The following section utilises hierarchical higher order approximations to investigate an ongoing problem, where traction oscillations on the interface are evident when a singularity exists on the crack front[178].

4.2.4 Traction oscillation problem in notched models

Interface elements governed by cohesive laws are used to model fissures which propagate from notches. As discussed in Section 4.2.2, the penalty stiffness used in the elastic stage of the interface element should be large enough to prevent significant deformations at the interface. High penalty stiffness may result in undesired spurious

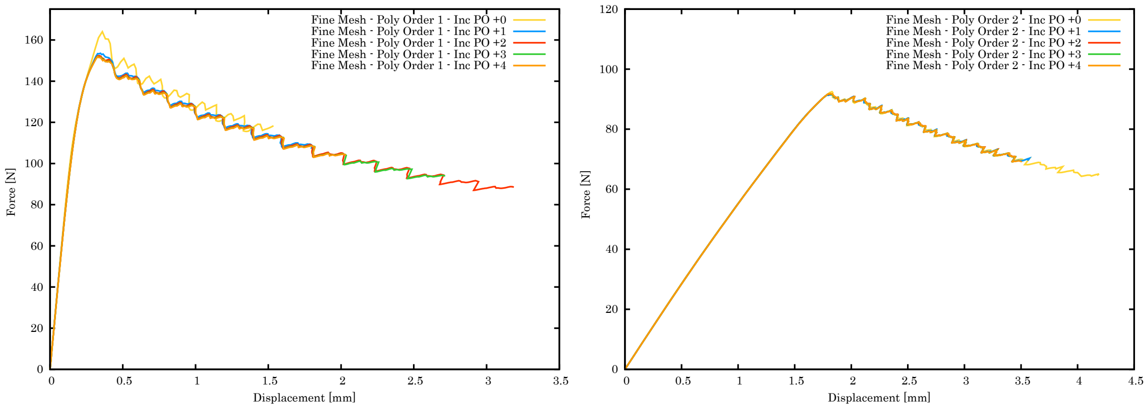

Figure 4-31: (a) 1^{st} PO approx. of solids elements and various p-refinements at the interface in fine mesh

(b) 2^{nd} PO approx. of solids elements and various p-refinements at the interface in fine mesh

Figure 4-32: De-lamination load-displacement graphs with uniform h and p-refinement of the solids and localised p-refinement of the interface

oscillations of the stresses at the interface (Figure 4-33) when the Gauss integration scheme is used. It was found that a nodal lumping scheme (the integration scheme is done over the pair of nodes of the interface rather than integration points, resulting in a diagonal stiffness matrix) or Newton-Cotes integration scheme are alternatives ways of reducing these oscillations[178].

It is here hypothesised that oscillations are the result of incompatibility between the traction distributed along the interface and dependent on the traction-separation constitutive law, and the stresses in the bulk. It is proposed that the order of approximation of the displacements in the bulk is made one order higher than for the displacements in the interface.

An identical beam to that studied by Schellekens (1993)[178] and Vignollet (2015)[213], having the same dimensions, with an initial notch and interface element at its centre is shown in Figure 4-34. A Young's Modulus of $20,000$MPa and Poisson's ratio of 0.2 was used for the solids. While Schellekens (1993)[178] use three different stiffness for the interface (10^3, 10^4 and 10^5 MPa) in this research, a high value of elastic stiffness $E_o = 20 \times 10^6$MPa was used. The 3D structured mesh finite element beam was subjected to a four-point bending test. Two sets of numerical experiments were

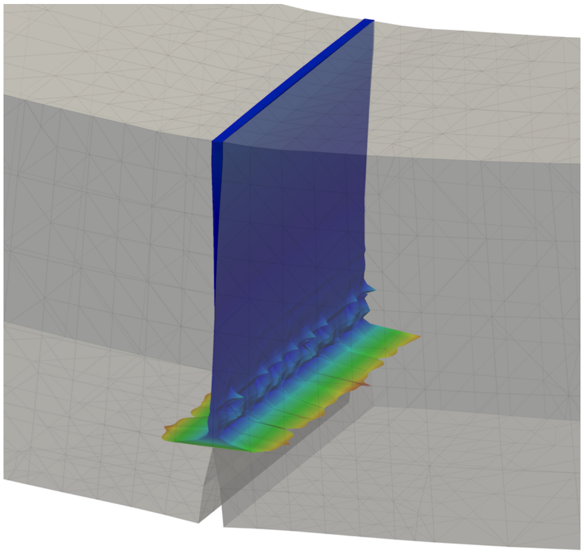

Figure 4-33: Stress concentration at the notch

conducted, the first set having uniform PO varying from 2^{nd} to 4^{th}, and the second set having a PO less on the interface (localised p-refinement). A load controlled Newton-Raphson method with arc length and basic line search control was used.

As part of the post-processing, stresses on elements were determined from the computed displacements. To observe the stress variation in every finite element, these were interpolated on a finer mesh using the hierarchical higher order shape functions. Paraview was then used to visualise the interpolated stress on the interface surface, with the aim of visualising stress oscillations. This problem was solved using MPI parallelisation and a SuperLU parallelised pre-conditioner on Intel® Xeon® CPU E7-4830 (2.13GHz) processors. 409,080 DOFs were solved in 114 seconds parallelised on eight processors. Computational efficiency was achieved by using hierarchical p-refinement rather than h-refinement, because a narrower bandwidth is obtained in the sparse stiffness matrix. It is hence much easier to pre-condition and solve the linear system of equations using a Krylov solver.

Spurious traction oscillations were not completely removed when displacements at the interface were approximated using a polynomial order less that than of the solid domain. This was demonstrated by comparing the models which used 2^{nd}, 3^{rd} and 4^{th} PO at the bulk, and 1^{st}, 2^{nd} and 3^{rd} PO at the interface (Figures 4-36, 4-38 and

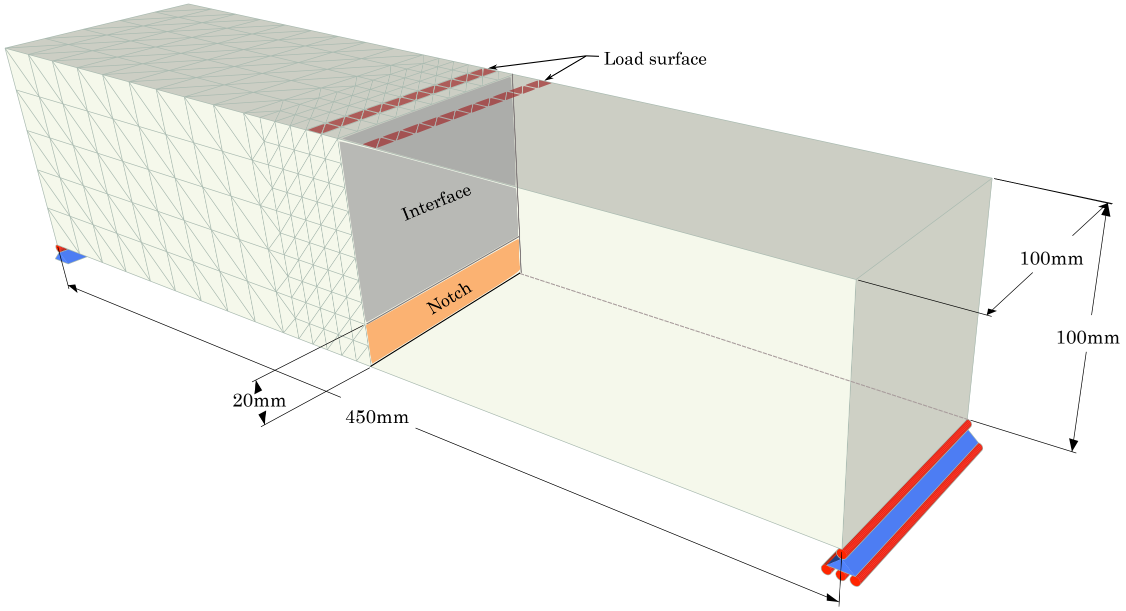

Figure 4-34: Diagram of notch beam

4-40 respectively), with those having uniform PO in the bulk and interface (2^{nd}, 3^{rd} and 4^{th} in Figures 4-35, 4-37 and 4-39 respectively). It is worthwhile noting that oscillations are not clearly visible in Figure 4-36 due to the linear approximation of displacement field at the interface.

Further localised p-refinement by increasing and reducing the PO at the interface was investigated, but showed no further improvement in the reduction or removal of traction oscillations at the interface. Understanding why Gauss quadrature leads to

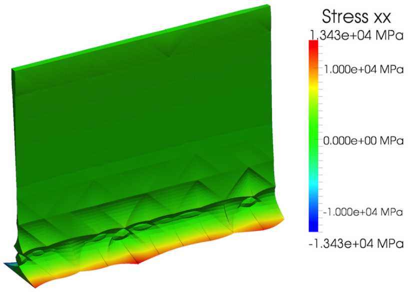

Figure 4-35: 2^{nd} PO approx. for solids and interface

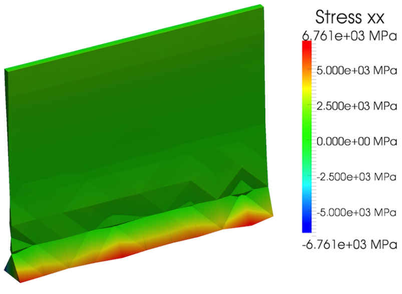

Figure 4-36: 2^{nd} PO approx. for solids, 1^{st}PO approx. for interface

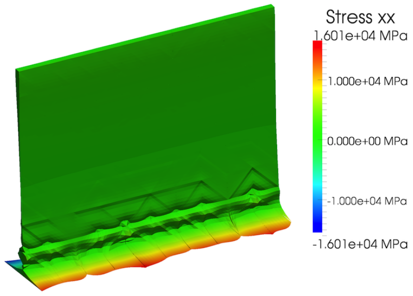

Figure 4-37: 3rd PO approx. for solids and interface

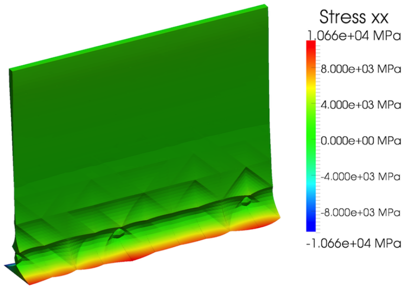

Figure 4-38: 3rd PO approx. for solids, 2ndPO approx. for interface

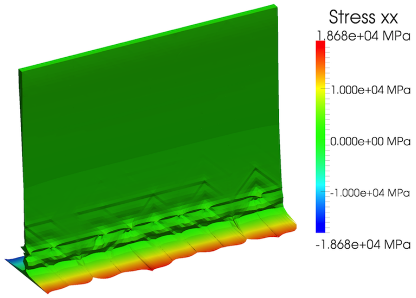

Figure 4-39: 4th PO approx. for solids and interface

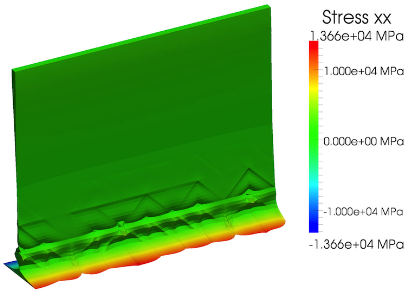

Figure 4-40: 4th PO approx. for solids, 3rdPO approx. for interface

Traction oscillations at interface

spurious traction oscillations at the notched interfaces is yet unclear, and further studies are necessary to determine why and how to solve this problem without changing the integration scheme.

4.3 Conclusion

In this chapter, a methodology for localised p-refinement at the interface was proposed using hierarchical higher order approximation[2]. This was beneficial when the interface element experienced non-linear behaviour due to damaging and large deformation. While h-refinement can be used, it is an inefficient approach, and uniform p-refinement using higher order interface elements constrains the possibility of having localised p-refinement to improve computational efficiency.

Hierarchical higher-order approximation is obtained by increasing the polynomial order of entities (edge, face and volume) of a finite element where eventually, higher order virtual DOFs (not related to physical nodes) are added into the system of equations. These higher order DOFs require higher order shape functions which are formulated according to Section 4.1, where conformity of shape functions of shared entities is enforced when integrating over the finite elements to obtain uniform approximation in between. Using a Gauss quadrature integration scheme requires an automated system by which enough base points and weight functions are generated for the polynomial degree in use. This eventually improves the computational efficiency because the correct number of Gauss points are used.

Section 4.2 discussed the formulation of a hierarchical higher order interface element. Following a standard interface formulation, the variation is only in the strain-displacement matrix **B** which is modified to account for the higher-order DOFs. The fact that linear interface elements are used, and the higher order DOFs have no physical connection to any node on the interface, means the rotational matrix **R** is computed considering only the vertex nodes of the interface. This formulation can be increased/decreased in a hierarchical way, depending on the polynomial order assigned to every entity is essential to conduct localised p-refinement on the interface.

A classic de-lamination problem using a 3D finite element method was used to test the implementation of hierarchical higher order approximation at the interface. Results were verified with a 2D numerical investigation conducted by Alfano and Crisfield[5] and an experimental investigation by Robinson and Song[167]. Uniform h, p and hp-refinement using hierarchical HO approximation provided accurate results, but not as computationally efficient as as the localised refinement. The Newton-Raphson controlled by arc-length method in which the load increment is controlled by the gap-opening of the interface is a numerically efficient method to achieve a good rate of convergence, while oscillations in the 3D de-lamination reduced the rate of convergence. As theory suggests[11;54], an exponential rate of convergence could be achieved by a combination of localised h and p-refinements. In this series of tests, the convergence rate was improved when uniform hp-refinement was used. While localised p-refinement was conducted on the entire interface, improvement in convergence was not achieved on such a problem because quadratic approximation with some mesh refinement was sufficient for good convergence. In complex problems with sophisticated damage laws to represent the interface elements, localised hp-refinement on the interface is essential in order to achieve good convergence and computational efficiency.

Localised p-refinement on the interface was used to investigate an ongoing problem of traction oscillation on the interface elements when the interface is very stiff compared to the solid, where a notch is located on the crack front while using the Gauss-Legendre quadrature integration scheme. This problem has been investigated since 1993 by Schellekens[178], whose solution was to adopt a Newton-Cotes/Lobatto integration scheme. In this research, a hypothesis to reduce the order of approximation on the interface due to the fact that tractions are one order less than the forces and displacements was tested by using performing localised p-refinement. This was only possible due to the implementation of hierarchical higher order approximation for interface elements. Although traction oscillations are reduced when the interface was approximated as one PO less than the bulk, some oscillations were still visible. This hypothesis was not therefore fully confirmed. This example was also used to demonstrate the improvement in computational efficiency when p-refinement is used, generating a sparse matrix with a narrow bandwidth, unlike h-refinement which requires extensive node renumbering to narrow the bandwidth.

Chapter 5

Modelling of braided fibres

The numerical study of fibre mechanics is a relatively new topic and mainly developed to model woven textile composites rather than braided fibres. In this chapter, a numerical approach is developed and implemented in a FEM tool to investigate the mechanical behaviour of braided fibres.

The process of carrying out a FE analysis of braided fibres is divided into two main parts: the pre-processing stage and the mechanical analysis stage. In this thesis, pre-processing is divided into three stages: preparation and meshing of the braided fibres, as discussed in Section 5.1; the inclusion of zero thickness interface finite elements between strands (Section 5.4); and the determination and application of the fibre directions in order to apply transversely isotropic material as explained in Section 5.2. In the mechanical analysis, the fibres are modelled as transversely isotropic, as explained in Section 5.3, while the equations of linear momentum balance are solved using a finite deformation formulation (considering small strains and large rotations) as discussed in Section 5.5.

5.1 Braid geometry

Braided fibres consist of complex shapes so it was necessary to develop an efficient technique to generate their geometries. A script routine was written in Cubit[176] that executes a set of algorithms to form 3D braided models of various dimensions. Cubit was also used to discretize these geometries into tetrahedral meshes for finite element analysis.

The simplest form of braiding consists of three interwoven strands, forming a plait (flat braid). Four or more strands can either form a plait or a sinnet (round)[121], depending on the interweaving configuration. More complex braids such as 3D braiding can be created, most often by computer algorithms[208]. Braided profiles can be used either for decorative purpose or for cordage use. Decorative plaits/sinnets are usually made from an elaborate interweaving of various fibres to form an aesthetically pleasing profile. Simpler plaits/sinnets are often used as cords due to better mechanical performance. This chapter considers two types of braiding: a three strand plait and a twelve strand double sinnet (also used in Marlow Technora T12 ropes), both shown in Figure 5-1.

The profile structure for both the flat plait and round sinnet had to be determined accordingly. While the profile for the flat plait was easy to determine, the profile for T12 is split into two main categories: six strand turns clockwise and another six turn counter-clockwise (Figure 5-2(b)). If the first strand starts at zero pitch height, the second strand starts at a sixth of the pitch height (equivalent to a rotation of 60° about the longitudinal axis of the rope) as shown in Figure 5-2(a). This incrementation is only valid for a twelve strand double braid sinnet rope and does not apply to other types of braids.

Once the profile centre line for every strand was determined, the solid part was formed by extruding the strand's cross-section along the same centre line. In reality, this cross section geometry varies along the braid. Here, though, a uniform circular cross-section was used to simplify the methodology. The model's cross-section diameter

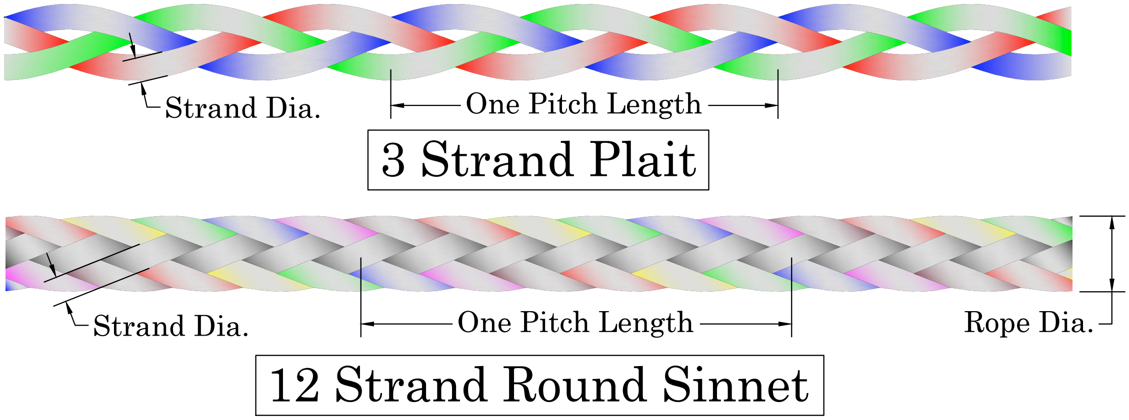

Figure 5-1: Representation of 3 strand plait and 12 strand round sinnet

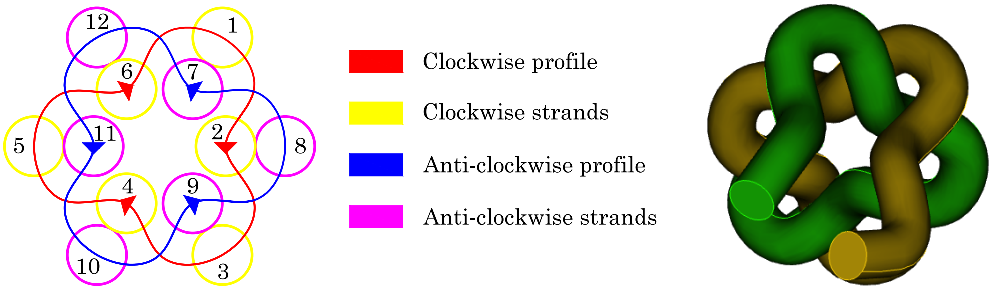

(a) Sinnet pattern of 12 strand round sinnet (T12)

(b) Example of left and right strand in 3D T12

Figure 5-2: Pattern recognition for T12 cord was increased to 15% of the actual diameter to achieve a degree of overlap between strands. By trimming one strand from the neighbouring one, common surfaces were created, where zero thickness interface elements were inserted. To determine the fibre directions (necessary to model the anisotropy of the material properties), a potential flow problem was analysed for every strand, where the fibre directions were found by assuming that the potential flow gradient is equivalent to the fibre directions. Interface elements were also used to allow free sliding between strands in contact and constrain inter-penetration. The overall procedure to generate the geometry and mesh for a T12 sinnet rope (Figure 5-3) is summarised in Algorithm 1. The execution duration to generate a single pitch length of cord was 82 seconds on a single 2.4GHz Intel Core i5 processor machine. Of this, 78 seconds were due to the trimming process. This represents an efficient way to produce an ACIS geometry and a tetrahedral mesh of a double braid sinnet rope of any dimension in a relatively short period of time.

Common faces between strands were denoted as sidesets in Cubit database, and such a database was used in MoFEM to enable an easy way of inserting interface elements on these faces. Meshing in Cubit was conducted in three main steps: define the approximate size of FEs; define the finite element type (i.e. Tetrahedral elements); and execute meshing.

```
Algorithm 1: Algorithm to generate T12 round sinnet
Data: Strand radius (r); Pitch length (P); Number of pitches (nP); Tolerance (x)
      between 1st and 2nd family of strands
Initialise: Calculate the coordinate points along the centre line of every strand
w.r.t. to r, P, nP and x using the profile shown in Figure 5-2(a)
for Strand 1 to 12 do
    Draw a spline axis of every strand;
    Draw the cross-section of every strand with radius r, orthogonal to the
    respective spline axis;
    Extrude the circular face along the spline axis;
end
Initialise: Define the trimming sequence of strands to form a common interface
between the strands. Size of trim depends on the tolerance x
for Loop of the size of the trimming sequence do
    Trim the strands according to the pre-defined sequence;
end
```

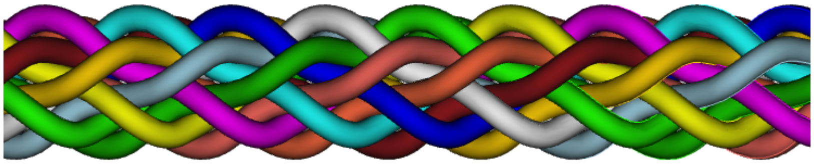

Figure 5-3: 3D ACIS geometry of 12 strand round sinnet cord

Once the FE mesh has been generated, geometrical entities representing boundary conditions and strands were classified as nodesets, sidesets, and blocksets in Cubit database and easily read by MoFEM. The next step was to determine the orientation of fibres (used to apply transverse isotropy) by solving Laplace's equation for a steady laminar incompressible potential flow problem, as discussed in the following section.

5.2 Determination of fibre directions

It is assumed that strands or yarns can be modelled using an elastic transversely isotropic constitutive model. Transverse isotropy is a subset of anisotropy, where material properties are isotropic on the transverse plane of the strands or yarns, but different along the longitudinal direction of the fibres (principal axis) (see Section 5.3).

Fibre directions for straight uniform cross-section strands can simply be determined by the geometry topology. On the contrary, it is rather difficult to use the geometry topology to determine the non-uniform fibre directions for non-uniform cross section (Figure 5-4) and/or twisted geometry (Figure 5-5).

This problem was solved by considering every strand as an individual steady laminar incompressible problem from which a potential flow gradient is computed and assumed to represent the fibre directions. If two or more neighbouring strands shared common faces, zero thickness interface elements were inserted to separate them into individual volumes (see Section 5.4). If neighbouring strands remain attached, an incorrect potential flow is computed due to flow leakage from one strand to another (see knot example in Section 5.4). Every strand was then represented as a tube, a potential

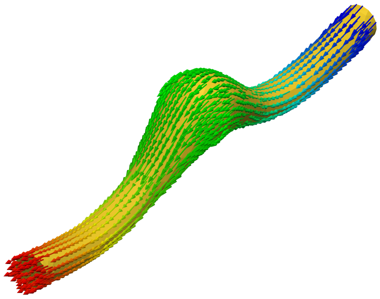

Figure 5-4: Flow in a non-uniform cross-section strand

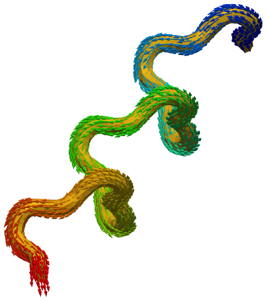

Figure 5-5: Flow in a twisted strand with uniform cross section

difference applied at both ends of each (Neumann boundary condition) and zero flux applied on the external wall of the tube (Dirichlet boundary condition). By solving Laplace's partial differential equation

$$\Delta\psi = \frac{\partial^2\psi}{\partial x^2} + \frac{\partial^2\psi}{\partial y^2} + \frac{\partial^2\psi}{\partial z^2} = 0 \tag{5.1}$$

a potential field ψ is computed. Its gradient $\nabla\psi$ represents the potential velocity $\mathbf{v}$ found. Subsequently, the potential velocity was assumed to be equivalent to the fibre directions $\mathbf{f}$. Once the fibre directions were determined at every integration point, a rotation matrix was computed (Section 5.3.2) and used to calculate the transversely isotropic stiffness matrix.

5.3 Elastic transversely isotropic material

In this thesis, bundles of fibres such as yarns and strands are represented as homogeneous transverse isotropic material, for which the material properties in the transverse plane differ from those along the fibres directions (principal axis). In fact, the stiffness in the transverse plane of a yarn is significantly smaller than the stiffness in the principal axis. This chapter will discuss the methodology adapted to model fibres as transversely isotropic materials. Simple tests in Abaqus were used to validate the implementation undertaken in MoFEM.

5.3.1 Definition

Transversely isotropic material is an anisotropic material, where the material properties are isotropic on the transverse plane. The transverse isotropic material is only defined by five parameters, unlike nine parameters required for orthotropic materials. Considering the case where the plane of isotropy lies in the x-y plane, the z-axis represents the axis of symmetry (more often referred to as the principal axis). The parameters for transverse isotropy are: E_z - the principal elastic stiffness along the z-axis; ν_{pz} - Poisson's ratio between the x-y plane and z-axis; E_p - elastic stiffness in the isotropic plane, ν_p - Poisson's ratio of the isotropic plane; and G_{zp} - the shear modulus contribution between the principal axis z-axis and plane of isotropy, as shown in Figure 5-6. These are used to construct the local transverse isotropic compliance and stiffness matrices as given in Equations 5.2 and 5.3.

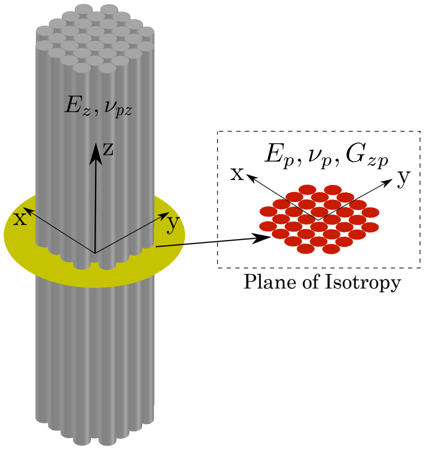

Figure 5-6: Transversely isotropic material parameters

Hooke's Equation for 3D Transversely Isotropy: $\boldsymbol{\varepsilon} = \boldsymbol{C}\boldsymbol{\sigma}$ ($\boldsymbol{\sigma} = \boldsymbol{D}\boldsymbol{\varepsilon}$), where $\boldsymbol{\varepsilon}$ and $\boldsymbol{\sigma}$ are the strain and stress vector respectively, and $\boldsymbol{C}$ and $\boldsymbol{D}$ are the compliance and stiffness matrices respectively.

$$\begin{bmatrix} \varepsilon_{xx} \\ \varepsilon_{yy} \\ \varepsilon_{zz} \\ \gamma_{xy} \\ \gamma_{yz} \\ \gamma_{zx} \end{bmatrix} = \begin{bmatrix} \frac{1}{E_p} & -\frac{\nu_p}{E_p} & -\frac{\nu_{zp}}{E_z} & 0 & 0 & 0 \\ -\frac{\nu_p}{E_p} & \frac{1}{E_p} & \frac{\nu_{zp}}{E_z} & 0 & 0 & 0 \\ -\frac{\nu_{pv}}{E_p} & -\frac{\nu_{pz}}{E_p} & \frac{1}{E_z} & 0 & 0 & 0 \\ 0 & 0 & 0 & \frac{2(1+\nu_p)}{E_p} & 0 & 0 \\ 0 & 0 & 0 & 0 & \frac{1}{G_{zp}} & 0 \\ 0 & 0 & 0 & 0 & 0 & \frac{1}{G_{zp}} \end{bmatrix} \begin{bmatrix} \sigma_{xx} \\ \sigma_{yy} \\ \sigma_{zz} \\ \sigma_{xy} \\ \sigma_{yz} \\ \sigma_{zx} \end{bmatrix} \tag{5.2}$$

$$\begin{bmatrix} \sigma_{xx} \\ \sigma_{yy} \\ \sigma_{zz} \\ \sigma_{xy} \\ \sigma_{yz} \\ \sigma_{zx} \end{bmatrix} = \begin{bmatrix} \frac{1-\nu_{pz}\nu_{zp}}{E_p E_z \Delta} & \frac{\nu_p+\nu_{zp}\nu_{pz}}{E_p E_z \Delta} & \frac{\nu_z+\nu_p\nu_{zp}}{E_p E_z \Delta} & 0 & 0 & 0 \\ \frac{\nu_p+\nu_{pz}\nu_{zp}}{E_z E_p \Delta} & \frac{1-\nu_{zp}\nu_{pz}}{E_z E_p \Delta} & \frac{\nu_{zp}+\nu_{zp}\nu_p}{E_z E_p \Delta} & 0 & 0 & 0 \\ \frac{\nu_{pz}+\nu_p\nu_{pz}}{E_p^2 \Delta} & \frac{\nu_{pz}(1+\nu p)}{E_p^2 \Delta} & \frac{1-\nu_p^2}{E_p^2 \Delta} & 0 & 0 & 0 \\ 0 & 0 & 0 & \frac{E_p}{1+\nu_p} & 0 & 0 \\ 0 & 0 & 0 & 0 & G_{zp} & 0 \\ 0 & 0 & 0 & 0 & 0 & G_{zp} \end{bmatrix} \begin{bmatrix} \varepsilon_{xx} \\ \varepsilon_{yy} \\ \varepsilon_{zz} \\ 2\varepsilon_{xy} \\ 2\varepsilon_{yz} \\ 2\varepsilon_{zx} \end{bmatrix} \tag{5.3}$$

where $\nu_{zp} = \frac{E_z \nu_{pz}}{E_p}$, $G_{zp} = \frac{E_z}{2(1+\nu_{pz})}$ and $\gamma_{ij} = \varepsilon_{ij} + \varepsilon_{ji} = 2\varepsilon_{ij}$ due to the symmetry of the stress and strain tensor.

5.3.2 Rotation of plane of isotropy

Equations 5.2 and 5.3 are described with respect to the fibre local coordinate system. In general, this is not aligned with the global coordinate system and it is necessary to rotate the stiffness matrix. Once the fibre directions are extrapolated from the potential flow velocity **v** (Section 5.2) at every Gauss quadrature point, axes and angles of rotation between the fibre directions and principal axis of transverse isotropy can be determined and rotation matrices **R** can be evaluated to rotate the local stiffness matrix at every Gauss quadrature point. A rotation matrix **R** based on axis/angle of rotation can be determined from an exponential mapping function[66] expressed as

$$\mathbf{R} = \mathbf{I} + \sin\theta\mathbf{N} + (1 - \cos\theta)\mathbf{N}^2 \tag{5.4}$$

where $\mathbf{I}$ is a 3x3 identity matrix, θ is the angle between the global z-axis and fibre direction $\mathbf{f}$, and $\mathbf{N}$ is a unit spinor. The axis-angle rotation system to compute the rotation matrix $\mathbf{R}$ for second order tensors is explained in Figure 5-7 for every integration point.

The components rotation matrix $\mathbf{R}$ is then used to form the transformation matrices $\mathbf{T}_\sigma$ as

$$\mathbf{T}_\sigma = \begin{bmatrix} R_{11}^2 & R_{21}^2 & R_{31}^2 & 2R_{21}R_{11} & 2R_{31}R_{21} & 2R_{11}R_{21} \\ R_{12}^2 & R_{22}^2 & R_{32}^2 & 2R_{22}R_{12} & 2R_{32}R_{22} & 2R_{12}R_{32} \\ R_{13}^2 & R_{23}^2 & R_{33}^2 & 2R_{23}R_{13} & 2R_{33}R_{23} & 2R_{13}R_{33} \\ R_{12}R_{11} & R_{22}R_{21} & R_{32}R_{31} & R_{22}R_{11} + R_{12}R_{21} & R_{32}R_{21} + R_{22}R_{31} & R_{12}R_{31} + R_{32}R_{11} \\ R_{13}R_{12} & R_{23}R_{22} & R_{33}R_{32} & R_{23}R_{12} + R_{13}R_{22} & R_{33}R_{22} + R_{23}R_{32} & R_{13}R_{32} + R_{33}R_{12} \\ R_{11}R_{13} & R_{21}R_{23} & R_{31}R_{33} & R_{21}R_{13} + R_{11}R_{23} & R_{31}R_{23} + R_{21}R_{33} & R_{11}R_{33} + R_{31}R_{13} \end{bmatrix} \tag{5.5}$$

and $\mathbf{T}_\varepsilon$ as

$$\mathbf{T}_\varepsilon = \begin{bmatrix} R_{11}^2 & R_{21}^2 & R_{31}^2 & R_{21}R_{11} & R_{31}R_{21} & R_{11}R_{21} \\ R_{12}^2 & R_{22}^2 & R_{32}^2 & R_{22}R_{12} & R_{32}R_{22} & R_{12}R_{32} \\ R_{13}^2 & R_{23}^2 & R_{33}^2 & R_{23}R_{13} & R_{33}R_{23} & R_{13}R_{33} \\ 2R_{12}R_{11} & 2R_{22}R_{21} & 2R_{32}R_{31} & R_{22}R_{11} + R_{12}R_{21} & R_{32}R_{21} + R_{22}R_{31} & R_{12}R_{31} + R_{32}R_{11} \\ 2R_{13}R_{12} & 2R_{23}R_{22} & 2R_{33}R_{32} & R_{23}R_{12} + R_{13}R_{22} & R_{33}R_{22} + R_{23}R_{32} & R_{13}R_{32} + R_{33}R_{12} \\ 2R_{11}R_{13} & 2R_{21}R_{23} & 2R_{31}R_{33} & R_{21}R_{13} + R_{11}R_{23} & R_{31}R_{23} + R_{21}R_{33} & R_{11}R_{33} + R_{31}R_{13} \end{bmatrix} \tag{5.6}$$

that can transform $\mathbf{C}$ using

$$\mathbf{C}^* = \mathbf{T}_\epsilon \mathbf{C} \mathbf{T}_\sigma^{-1} \tag{5.7}$$

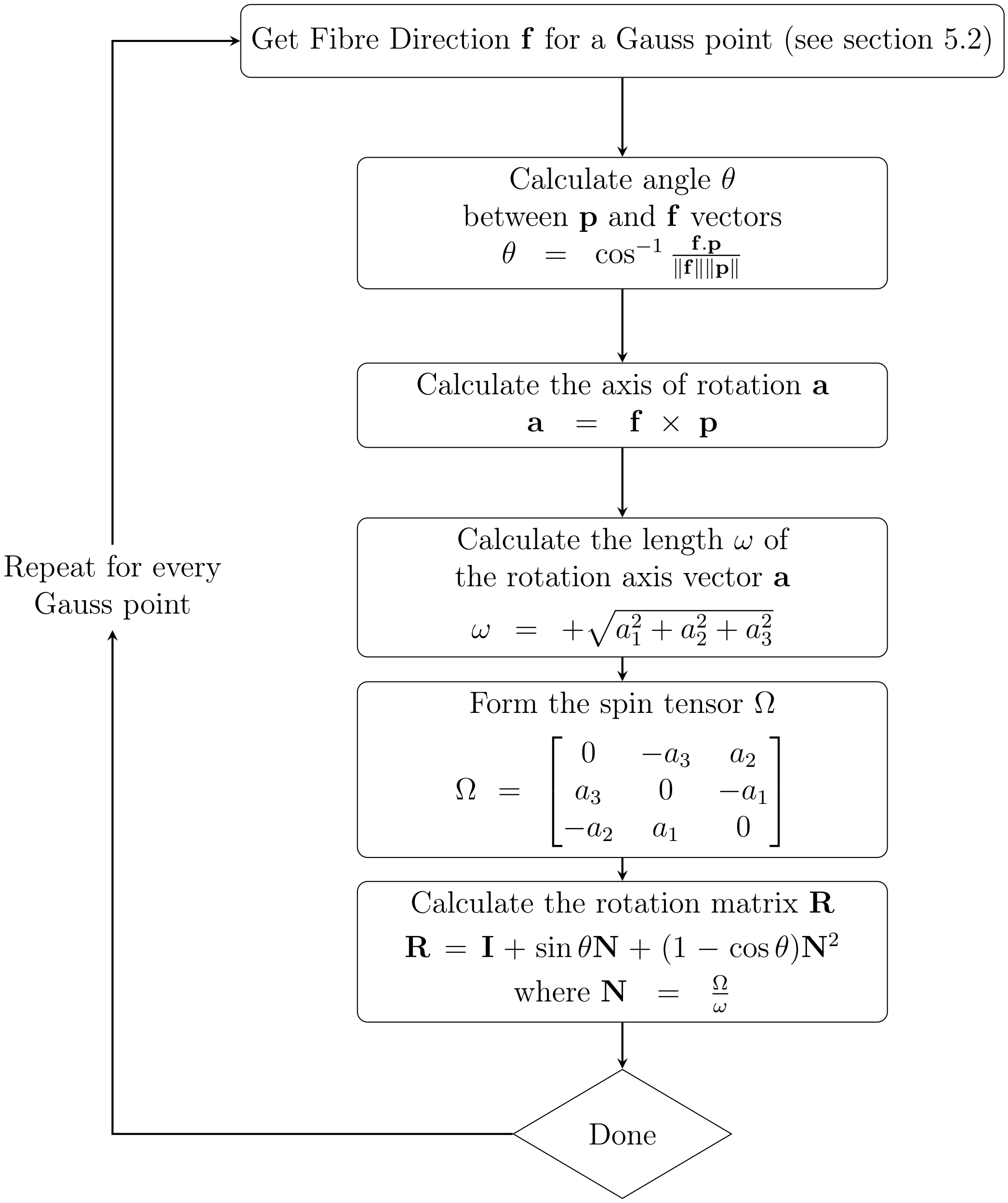

Figure 5-7: Axis-Angle Rotation Procedure

and **D** using

$$\mathbf{D}^{*} = \mathbf{T}_{\sigma}\mathbf{D}\mathbf{T}_{\epsilon}^{-1} \tag{5.8}$$

The inverse transformation $\mathbf{T}_{\sigma}^{-1}$ and $\mathbf{T}_{\epsilon}^{-1}$ are computed by determining $\mathbf{R}$ for a negative angle θ in Equation 5.4. The formulation of the rotation matrix ($\mathbf{R}$) and transformation matrices ($\mathbf{T}_{\sigma}$ and $\mathbf{T}_{\varepsilon}$) were validated in Section 5.3.3.

5.3.3 Verification of transversely isotropy

The implementation of elastic transversely isotropic material in MoFEM has been validated analytically and cross-referenced with an identical problem solved in Abaqus. A unit cube with minimal Dirichlet boundary conditions on one side and with a unit tensile pressure on the other side was used as a benchmark test. An elastic transversely isotropic material with parameters, shown in Table 5.1, was used and its principal axis $\mathbf{p}$ was aligned to the fibre direction $\mathbf{f}(0, 1, 1)$ using an appropriate rotation matrix $\mathbf{R}$ as described in Section 5.3.2. The model was analysed using small deformation theory.

Parameter	Value	Parameter	Value
E_z	1.00	ν_{pz}	0.15
E_p	1.00	G_{zp}	1.00
ν_p	0.20	$\mathbf{f}$	[0, 0.5, 0.5]

Table 5.1: Material Parameters for Benchmark Model

Numerical solution

This problem was analysed in MoFEM, approximating the displacement field linearly in every finite element. The resulting strain vector

$$\varepsilon = \left[\begin{array}{c} -0.175, 0.175, 0.675, 0.0, 0.0, 0.0 \end{array} \right]$$

corresponds exactly to the analytical solution. The equivalent displacements are shown in Figure 5-8.

The same problem was analysed using Abaqus software where the same results as those of MoFEM were obtained. Abaqus CAE environment constrains transverse isotropy direction to be defined by a vector or spatial expression in every continuum ("block" in Abaqus terminology). Meanwhile, Abaqus script subroutines allow the rotation of transverse isotropy to be achieved by a set of predefined fibre direction[92].

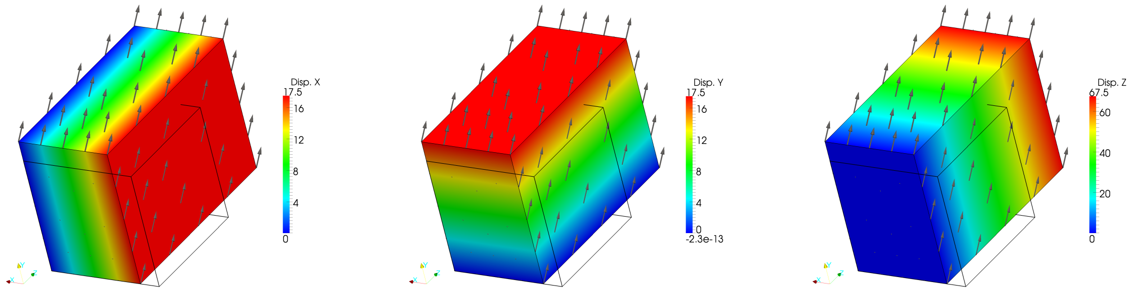

Displacement Contours in x-axis

Displacement Contours in y-axis

Displacement Contours in z-axis

Figure 5-8: MoFEM Displacement Results

5.4 Interface elements representing contacts between strands

This section focuses on a simplified approach to modelling the contact between strands. Contact interaction is developed as strands are interwoven to form braids, textile and knots. As discussed earlier in this chapter, strands must have separate mesh domains and the mechanical interaction between strands is not neglected. Frictionless sliding between strands was considered, based on the assumption that that fibres have a low coefficient of friction similar to that of carbon[87], while interpenetration of strands was constrained. Contact interaction is usually modelled using contact mechanics, which is extremely expensive for complex geometries such as braids[126].

Assuming that the contact surfaces between strands do not change significantly, this thesis proposes that interface elements are sufficient to model this interaction.

Interface elements, as discussed in Section 4.2, were used and inserted where contact exist between strands. An elastic constitutive model for interface elements was used to simulate the free sliding and penetration free interface mechanism. This was achieved by using a very low stiffness to govern Modes II and III (i.e. E_{t_1} and E_{t_2}) and a very high stiffness governing Mode I (i.e. E_n). Although E_{t_1} and E_{t_2} should be equal to zero to achieve 100% free sliding, this was not possible as the interface stiffness matrix becomes singular. Similarly, the ratio between E_n and E_{t_1} or E_{t_2} should not be very high, as this produces an ill-conditioned global stiffness matrix. Therefore a poor rate of convergence is experienced when using an iterative solver to solve the linear system of equations.

Knot example

Tightening knot was numerically analysed to illustrate how interface elements were essential in such circumstances. A large-displacement formulation (see Section 5.5) and elastic transversely isotropic material ($E_z = 135GPa, E_p = 50GPa, \nu_p = 0.4, \nu_{pz} = 0.1$ and $G_{zp} = \frac{E_z}{2(1+\nu_{pz})}$) were used. An elastic interface element with $E_{o_n} = 13500GPa$ and $E_{o_{t1}} = E_{o_{t2}} = 1GPa$ as parameters was also used. E_{o_n} is very large to mitigate penetration, while $E_{o_{t1}}$ and $E_{o_{t2}}$ are very low to provide a quasi frictionless interaction. Choosing smaller E_{o_n} can dramatically increase the condition number of the global stiffness matrix. During the geometrical modelling of the knot, it was assured that a good interface area of the ravelled knot was obtained. This was achieved by increasing the diameter of strand where solids overlapped and by trimming this overlapping. Common surfaces were created as shown in Figure 5-9(right).

After the discretisation of the knot geometry into a FE mesh, interface elements were inserted at the contact surfaces. Interface elements were also helpful to divide the finite elements between one side and the other side of the knot. This was essential to accurately identify the external wall correctly and assign zero flux condition for the

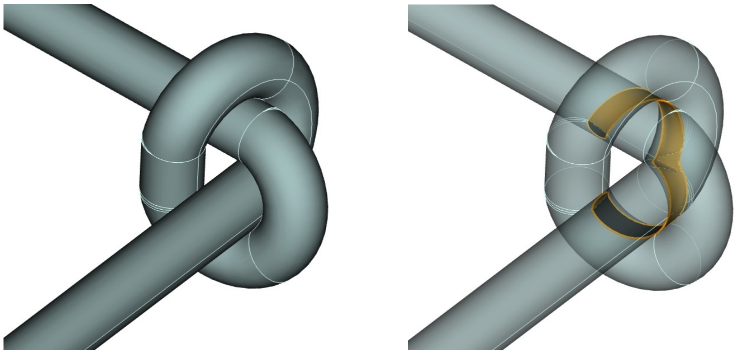

Figure 5-9: Left: knot geometry - Right: highlighted contact surface of knot

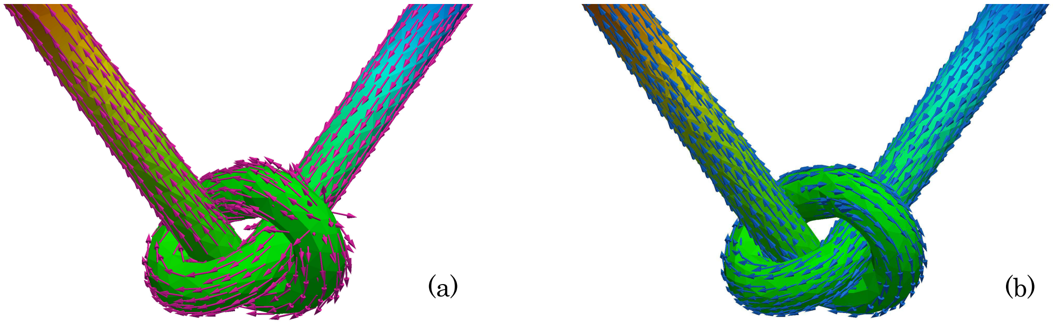

Figure 5-10: (a) leaking surface boundary - wrong flow and (b) tight surface boundary - correct flow

potential flow problem (Figure 5-10(b)). If interface elements were not inserted, the knot would have been analysed as a single solid domain and wrong directions determined (Figure 5-10(a)). Interface elements were later used to simulate the mechanical interaction between the ravelled knot as discussed earlier in this section.

After determining the fibre orientation as discussed in Section 5.2, this elastic knot was fully fixed on one end and subjected to tensile loading on the other end; a large displacement FE formulation was used. During this mechanical analysis, transverse isotropy alignment to the fibre orientation in MoFEM was automatically performed at every load step following the procedures discussed in Section 5.3. The mechanical performance is partly described in the load vs axial-displacement graph shown in Figure 5-11. This consists of an exponential stiffening of the tightening knot, followed by a geometric locking release, hence resulting in a loss in overall stiffness. This is then followed by further re-tightening and re-softening behaviour. At this stage the knot was nearly fully tightened and embedded. Using interface elements to model this interaction is restricted to certain cases and cannot be used if the deformed geometry requires a redefinition of the contact surfaces, for which contact models are required.

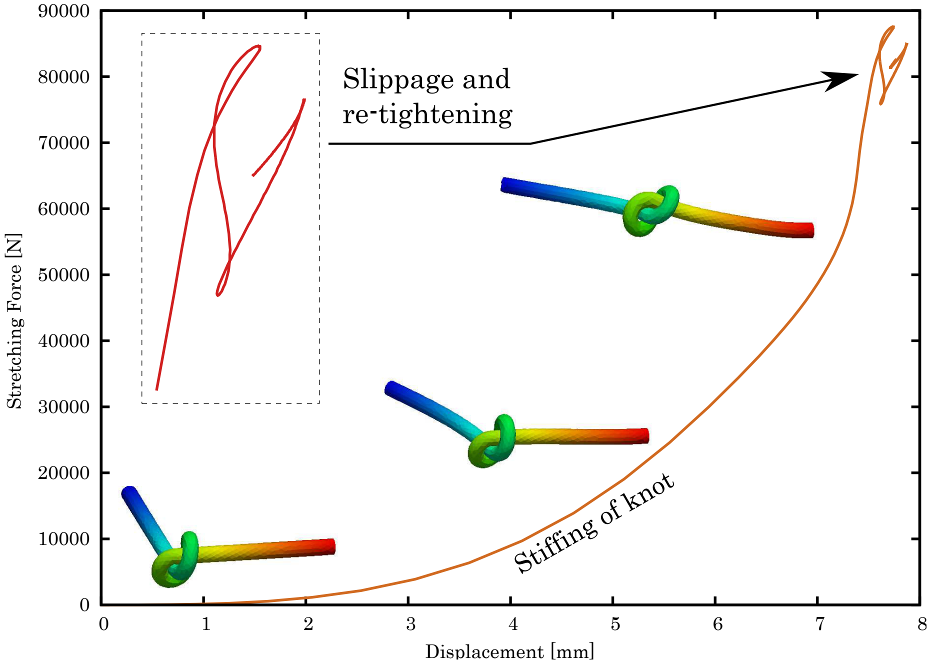

Figure 5-11: Axial load-displacement graph for stretching behaviour of knot

5.5 Large deformation modelling of fibres

The main focus of this thesis is to propose a procedure to model braided fibres. Materials such as carbon, glass and Kevlar fibres behave like elastic under tension and extend very little due to their high stiffness. Fibres are also easy to bend due to their thin and elongated geometries. The kinematics of fibres is therefore considered as hyperelastic and can be modelled in FEA using the Total Lagrangian (TL) formulation based on small strains and large rotations.

A suitable hyperelastic model is the St Venant Kirchhoff model which suits materials that exhibit small strains and large rotations. The strain energy density function for St Venant Kirchhoff model is defined as

$$\Psi = \frac{1}{2}\mathbf{E} : \mathbf{D} : \mathbf{E} \tag{5.9}$$

where **D** is the elastic stiffness matrix and **E** is the Green strain tensor, defined as

$$\mathbf{E} = \frac{1}{2}[\mathbf{F}^T\mathbf{F} - \mathbf{I}] = \frac{1}{2}[\mathbf{d} + \mathbf{d}^T] + \frac{1}{2}\mathbf{d}^T\mathbf{d} \tag{5.10}$$

$\delta\mathbf{E}$ is the change in the Green strain tensor defined as

$$\delta\mathbf{E} = \frac{1}{2}\mathbf{F}^T\delta\mathbf{d} + \frac{1}{2}\delta\mathbf{d}^T\mathbf{F} + [\frac{1}{2}\delta\mathbf{d}^T\delta\mathbf{d}] \tag{5.11}$$

and **d** is the displacement-derivative matrix given as

$$\mathbf{d} = \begin{bmatrix} \frac{\partial u_i}{\partial X_i} & \frac{\partial u_i}{\partial X_j} & \frac{\partial u_i}{\partial X_k} \\ \frac{\partial u_j}{\partial X_i} & \frac{\partial u_j}{\partial X_j} & \frac{\partial u_j}{\partial X_k} \\ \frac{\partial u_k}{\partial X_i} & \frac{\partial u_k}{\partial X_j} & \frac{\partial u_k}{\partial X_k} \end{bmatrix} \tag{5.12}$$

and **F** is deformation gradient tensor given as

$$\mathbf{F} = [\mathbf{I}_3 + \mathbf{d}] \tag{5.13}$$

This thesis proposes that the St Venant Kirchhoff model can be expanded to fibrous materials by considering $\mathbf{D}$ to be the elastic transversely isotropic stiffness matrix (see Section 5.3).

The virtual work in the Total Lagrangian (TL) formulation is expressed as

$$W = \int_{V_o} \mathbf{S} : \delta \mathbf{E} \, dV_o - W_{ext} \tag{5.14}$$

and the change in virtual work δW, from which the tangent stiffness ($\mathbf{K}_t$) can be obtained, is defined as

$$\delta W = \int_{V_o} \left[\delta \mathbf{E}^T \mathbf{C} \delta \mathbf{E} + \mathbf{S} : \delta \mathbf{d}^T \delta \mathbf{d} \right] dV_o = \delta \mathbf{u}^T \mathbf{K}_t \delta \mathbf{u} \tag{5.15}$$

where the 2^{nd} Piola-Kirchhoff stress tensor $\mathbf{S} = J\mathbf{F}^{-1}\boldsymbol{\sigma}\mathbf{F}^{-T}$, $\boldsymbol{\sigma}$ is the Cauchy 2^{nd} order stress tensor (also call stress tensor) and the J is the Jacobian ($J = \det \mathbf{F}$).

The Newton-Raphson method from PETSc's Scalable Nonlinear Equations Solvers (SNES) was chosen to solve these nonlinear problems. Furthermore, the secant line search method over the L2 norm built in with PETSc's arc-length control technique already built in MoFEM was used to improve the rate of convergence at every load step.

5.5.1 Example - transversely isotropic cantilever

In this section, the bending of a simple 3D transversely isotropic cantilever was investigated using finite deformation formulation as previously discussed. A cantilever measuring 1mm by 1mm by 20mm was fully fixed on one side and loaded on the other side, which was also constrained the out of plane direction (constrained in the x-direction). The material parameters for transversely isotropic material were, $E_p = 100$GPa, $E_z = 200$GPa, $\nu_p = \nu_{pz} = 0.3$ and $G_{zp} = \frac{E_z}{2(1+\nu_{pz})}$. Three different models with three different fibre orientations were examined, i.e. fibres oriented along the x, y and z-axis (Model Cantilever_X, Cantilever_Y and Cantilever_Z respectively).

The applied loading was constantly updated during the load steps to maintain its orthogonality to the edge of the cantilever as shown in Figure 5-12.

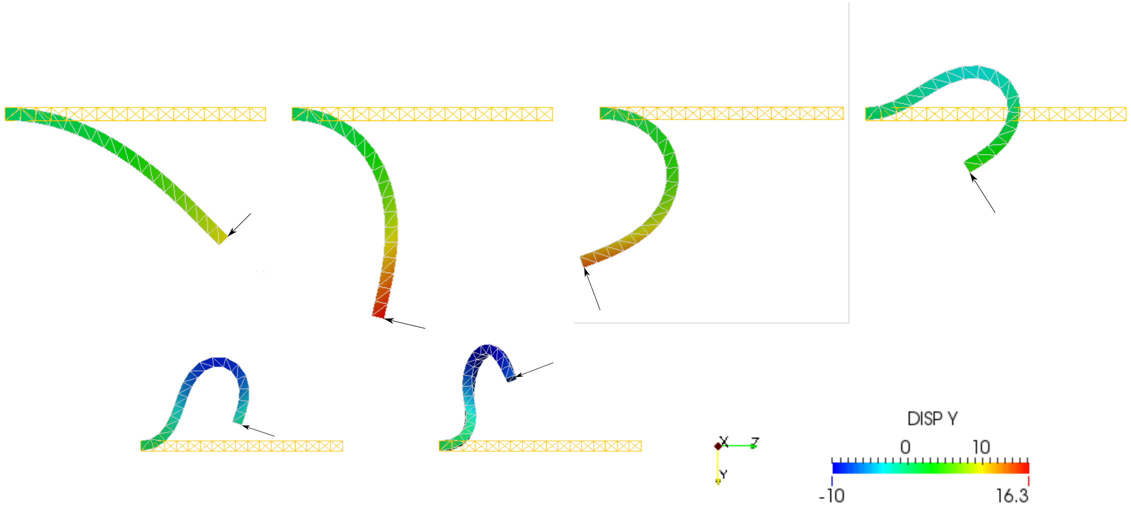

Figure 5-12: Large deformation transversely isotropic cantilever - Cantilever_X

As foreseen, Cantilever_Z behaved more rigidly than Cantilever_Y and even more than Cantilever_X (the stiffness of Cantilever_Z was nearly equivalent to a cantilever with an isotropic material of 100GPa Young's modulus) (see Figure 5-13). Unlike small deformation formulation, spurious strains in finite deformation are not an issue (Figure 5-12). Comprehensively, no numerical problems were observed where the KSP solver converged in less than 3 iterations, and the non-linear solver converged in not more than 12 iterations. In MoFEM, the load step size automatically increases by a user-defined factor unless a certain number of iterations threshold is exceeded for the convergence of the previous load step. If this is exceeded, the load step size is reduced by 90% (or any user-defined percentage) to improve the rate of convergence. This behaviour was observed in the load-displacement graph, Figure 5-13.

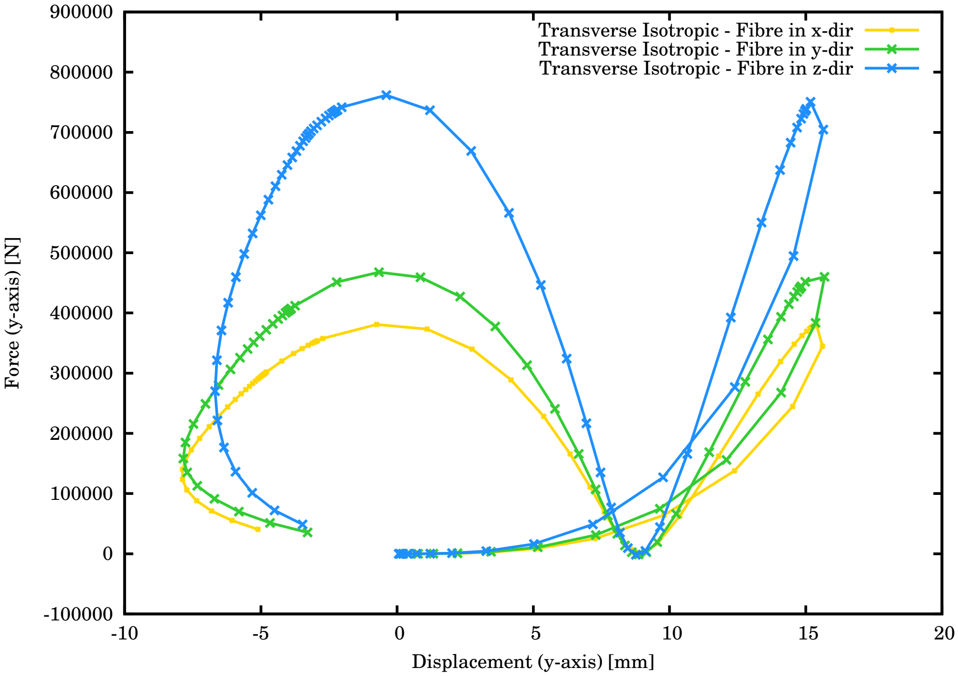

Figure 5-13: Load-displacement for three cantilevers with different fibre orientation

5.6 Numerical example

The outcome of this section is the demonstration of the importance of using finite deformation and considering fibrous materials as transversely isotropic material when modelling braided fibres. The aim of the first numerical example was to investigate the difference between a small and a large displacement formulation and the use of isotropic and transverse isotropic materials to represent the strands of a three strand plait subjected to longitudinal tension. After this study, a more advanced approach to modelling and understanding the mechanical behaviour of a T12 under tension (a type of braiding configuration of 12 strands) was undertaken.

5.6.1 Example 1: three plaited braid

A three strand plait 3D model was selected to examine the benefits of using large displacement formulation based on small strains and large rotation, and the importance of defining the material as transversely isotropic material in similar problems. After establishing the geometrical configuration of the three strand plait, a Python/APREPRO script was written, and after prescribing the geometrical parameters shown in Figure 5-14, the script was executed in Cubit to generate the corresponding 3D model and a FE mesh. Within this model, 22 common surfaces between the three strands were identified, and interface elements were inserted (Figure 5-15(top)) according to Algorithm 2 (see Section 5.4 for more details). Fibre directions in every strand were computed (Figure 5-15(bottom)) according to Algorithm 3 (see Section 5.2). During this pre-processing stage, the insertion of interface elements was the most computationally expensive, followed by the building the system of equations as shown in Table 5.2.

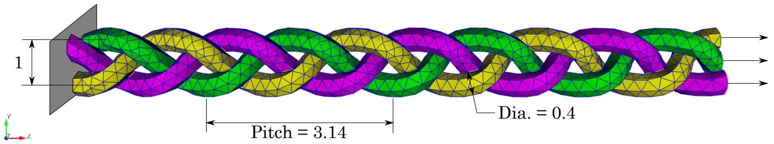

Figure 5-14: 3 Plait Braided Model

```
Algorithm 2: Pre-processing algorithm for interface insertion
Input: Load Cubit mesh having $i$ number of common interfaces between strands
were classified as sidesets named interface_$i$;
for level of h-refinements do
    For every level of refinement, every edge is divide into 2 edges, every triangle is
    divide into 4 triangles and every tetrahedron is divided into 8 tetrahedrons;
    Update cubit BC meshsets;
    The new refinement can be stored in a new mesh level or squashed with the
    previous original mesh level;
end
foreach interfaces $i$ do
    Identify the triangles in the relevant sideset;
    Split the nodes and update the adjacent triangle and tetrahedron;
    Insert prism element to represent the interface;
    Update cubit BC meshsets;
    This refinement can be inserted in a new mesh level or squashed with the
    previous original mesh level;
end
```

After inserting interface elements and finding the fibres' directions, the model was ready for study of its kinematics. The material parameters assigned for both iso-

Algorithm 3: Pre-processing algorithm for solving potential flow

```
Input: Same loaded mesh (Algorithm 2) with s number of strands having the following information:
Every individual strand was classified as a meshset named PotentialFlow_s;
A inlet and outlet surface were identified for every strand and classified as sidesets named PressureIO_s_1 and PressureIO_s_2 respectively;
A zero pressure node for every strand was categorised as nodeset named ZeroPressure_s
Initialise: Add a potential field
foreach strand s do
    Add finite element for every strand and insert their respective tetrahedrons to the finite element;
    Include every finite element to the potential field;
    Add potential problem for every strand;
    Load BCs;
end
Initialise: Build fields, finite elements, problems
Initialise: Partition every problem
foreach strand s do
    Loop of finite elements and building stiffness matrix;
    Apply loaded BCs;
    Solve the potential flow problem;
end
Finalise: Export potential field to a tag on mesh and save
```

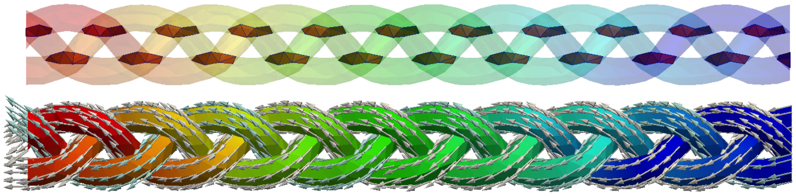

Figure 5-15: Pre-Processing - Top: Highlighted interface elements; Bottom: Fibre directions

Interface Insertion	**Building Problem**	**Partitioning**	**Solving**	**Post-processing**	**Total**
22 Interfaces (127 tri)		1 processor	8881 dofs	transferring data from field to mesh and save	
16.35	7.74	0.66	1.64	1.22	**27.61s**

Table 5.2: Duration breakdown of pre-processing

tropic and transversely isotropic models are given in Table 5.3. The model was fully restrained on one side and tensioned axially on the other side as shown in Figure 5-14.

Isotropic	**Transverse Isotropic**	**Interface**
$E = 135000$ $\nu = 0.1$	$E_z = 135000$ $E_p = 50000$ $\nu_p = 0.4$ $\nu_{pz} = 0.1$ $G_{zp} = \frac{E_z}{2(1+\nu_{pz})}$	$D_n = 13500000$ $D_{t1} = 1000$ $D_{t2} = 1000$

Table 5.3: Material and interface parameters for the three plaited braid

Elastic small deformation

The kinematics of the three plaited braid using transversely isotropic fibres were studied using infinitesimal strain theory. Using linear polynomial approximation (1^{st} order), the linear static elastic problem with 4809 DOFs was solved in 1.015s on a single 2.4GHz Intel Core i5 processor. Due to large rotation of finite elements and the use of small deformation theory, the formation of spurious strains induce unrealistic sagging deformation of the plait as observed in Figure 5-16(b).

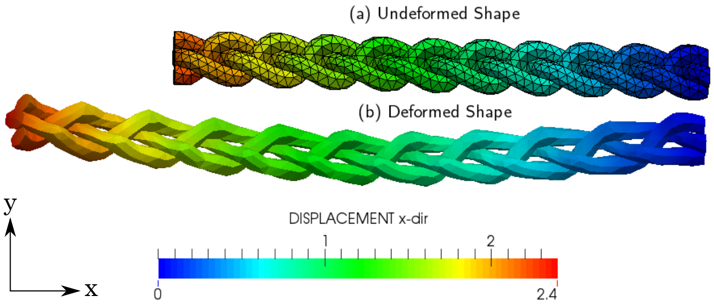

Figure 5-16: Linear geometry

Elastic large deformation

In this section, the kinematics of the three plaited braid were studied using finite deformation theory based on small strains and large rotations as discussed in Section 5.5. This study considered four models: the first model had isotropic material, while the second to fourth models had transversely isotropic material (see Table 5.3 for material parameters). The displacement field was approximated linearly in the first and the second models, while quadratic and cubic hierarchical higher order approximation was used in third and fourth models respectively (summarised in Table 5.4).

Model No.	**Material** (see Table 5.3)	**Polynomial Approximation Order**
3P_I_PO1	Isotropic	1^{st} Order
3P_TI_PO1	Transversely Isotropic	1^{st} Order
3P_TI_PO2	Transversely Isotropic	2^{nd} Order
3P_TI_PO3	Transversely Isotropic	3^{rd} Order

Table 5.4: List of 3-plait braided models analysed using large displacement formulation

From the load-displacement behaviour of the transversely isotropic model (Figure 5-17), convergence was observed among linear, quadratic and cubic approximations (p-refinement using hierarchical higher order approximation (see Chapter 4)). From the same graph, stiffening due to an embedding process was noted. Unlike Figure 5-16 (small deformation), in Figure 5-18 (large deformation) there is no artificial sagging, and the overall deformation is more realistic.

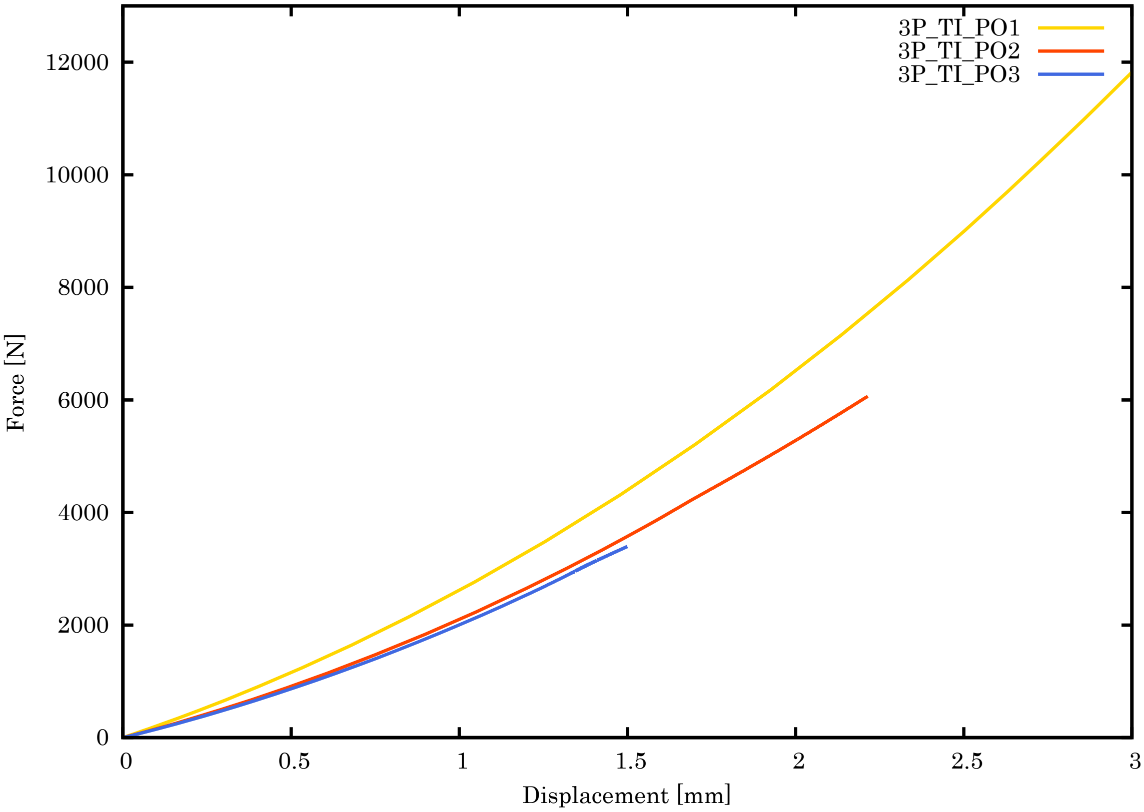

Figure 5-17: Load-displacement convergence results for three plait braided model using different degrees of polynomial

Artificial torsional twisting about the longitudinal axis was observed in the isotropic model compared to the transversely isotropic model, as shown in Figure 5-19. This was due to excessive stiffness in the transverse plane of the isotropic strands, leading to the conclusion that realistic kinematics of plaited braids are only achieved by defining the strands as transversely isotropic material.

Further research is required to understand how different parameters of the interface element and transverse isotropy influence the overall kinematics of a three plaited braid.

5.6.2 Example 2: T12 sinnet rope

From the previous example, it was concluded that numerical modelling of braided stiff fibres should be conducted under small strains and large rotations finite deformation

(a) Undeformed Shape

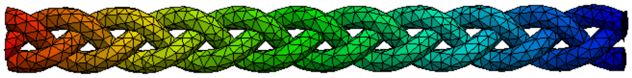

(b) Deformed Shape

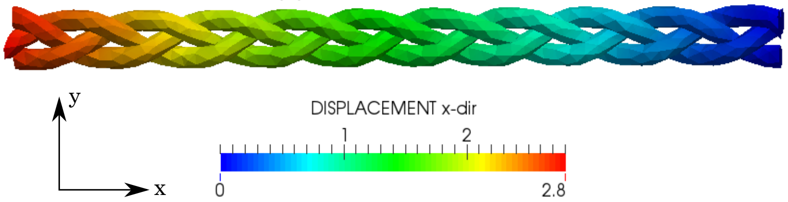

Figure 5-18: Nonlinear geometery

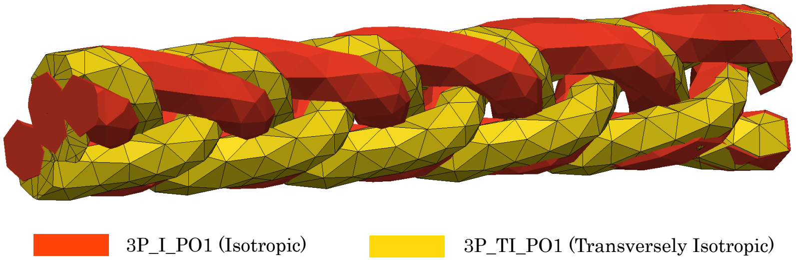

Figure 5-19: Torsional twist on the 3 plait model when using isotropic material compared to transversely isotorpic (figure represents half of the model)

theory and that fibrous materials should be considered transversely isotropic. This section discovers the challenge undertaken in examining the mechanical behaviour of T12 sinnet rope under axial tension.

A T12 sinnet rope was generated (see Section 5.1) using the dimensions given in Figure 5-20. The rope was then anchored using two steel plates on each end as shown in Figure 5-20, ensuring that all strands were evenly stretched. The bottom anchor was constrained in all directions, while the top plate was constrained in x and y-directions and loaded in the z-direction.

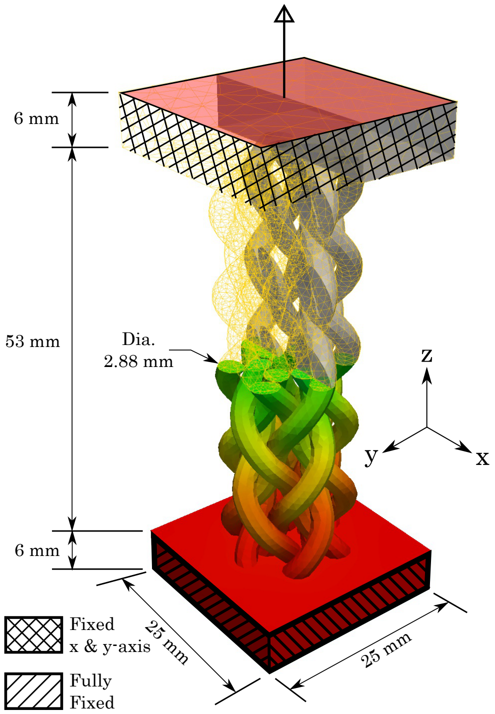

Figure 5-20: T12 sinnet rope model

Geo. Parameters	
No. of Strands	12
Pitch Length	60 mm
Strand Radius	1.44 mm
Braid Type	sinnet T12
Fibre Mat. Parameters	
E_z	135,000 MPa
E_p	50,000 MPa
ν_p	0.3
ν_{pz}	0.1
Clamp Mat. Parameters	
E	200,000 MPa
ν	0.3

Table 5.5: Geometry and Material Parameter of T12 sinnet rope

The model was meshed as shown in Figure 5-20 containing about 50,000 tetrahedral elements and 13,656 nodes. Similarly to the three plaited example, interface elements between the strands and the clamps were inserted and fibre directions were found for every strand. The material parameters are given in Table 5.5 and were saved to their respective blocksets in Cubit and automatically read in MoFEM.

As discussed earlier, a TL formulation based on small strains and large rotations was used to model braided fibres. The non-linear convergence criterion $\|\mathbf{F}\| < 1.0\, e^{-6}$ was used, where $\mathbf{F}$ is the residual force vector. An average of five iterations for every load step was necessary for the solution to converge. P-refinement was performed using 1^{st}, 2^{nd} and 3^{rd} polynomial degree (Model No: T12_PO1, T12_PO2 and T12_PO3 respectively) using hierarchical higher order approximation and their load-displacement behaviour is shown in Figure 5-22.

Contrary to the observed experimental behaviour of T12 under tension (Figure 5-21), tightening and bedding of strands in the numerical model was not observed. This

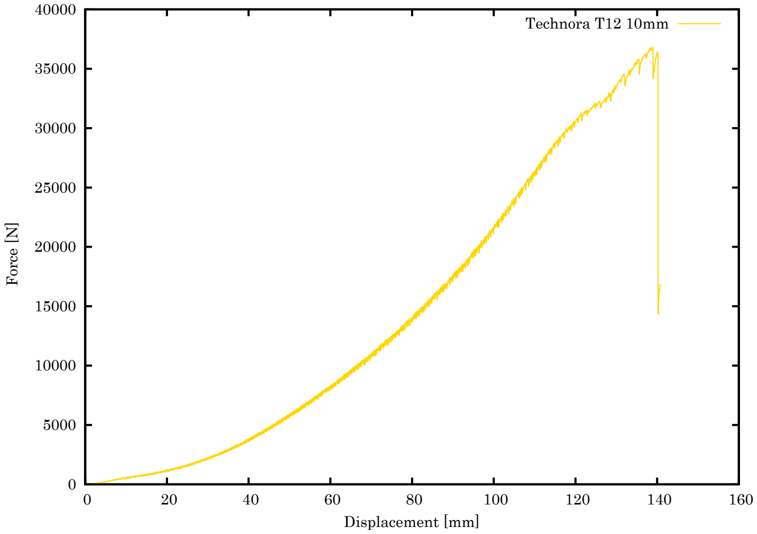

Figure 5-21: Tensile test experiment of 10mm Technora T12 sinnet rope

suggested that a geometrically rigid lattice structure was formed from the sinnet configuration and that E_p was higher than the actual transversal stiffness (this was necessary to avoid ill-conditioning). Similarly to the three plaited model, using interface elements proved an effective solution to model contact, where free sliding/rotation and penetration constraint was possible between neighbouring strand domains.

Further work is necessary to produce an effective numerical tool to simulate complex braided geometries. Braids should be modelled with tighter geometries and to look more realistic. Secondly, a solution for the ill-conditioning of transverse isotropic stiffness matrices must be found. Once the T12 braided fibres are successfully modelled numerically and their mechanical behaviour is obtained, it can be assumed that overall performance can be represented by an elastic transversely isotropic material, and such homogenisation can be used in other problems using less computational effort (example in Section 6.3.2).

Polynomial Degree	**Number of DOFs**	**Number of processors**	**Maximum extension** (mm)	**Actual solution time** (hours)
1^{st}	39,937	8	3.98	8.09
2^{nd}	255,961	16	2.98	33.54
3^{rd}	798,781	16	1.96	150.24

Table 5.6: Computational summary of large deformation analysis of T12 model

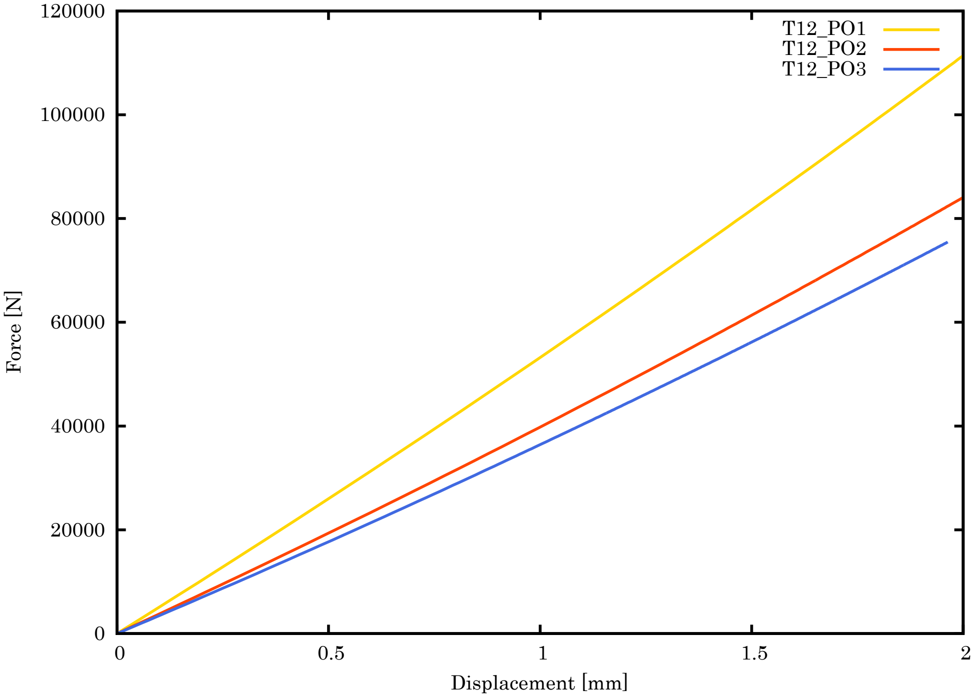

Figure 5-22: Load-displacement of finite element T12 sinnet rope model under tension

5.7 Conclusion

In this chapter, a new methodology for studying the mechanics of braided fibres using the FE technology is proposed and illustrated with various examples.

The first stage was to model braided geometries such as plaits and sinnets. This was achieved by determining how braided profiles are constructed. Subsequently dynamic algorithms were written in Cubit to generate the respective geometries of any desired dimensions. In the second stage, interface elements were inserted between the strands to allow free sliding and prevent interpenetration. Thirdly, by solving a steady-state incompressible laminar potential velocity problem for every strand, the potential flow was determined and later was assumed to be equivalent to the fibre directions. Following this, the principal axis of transverse isotropy was aligned from its global position to the fibre directions at every Gauss integration point.

In this thesis, it was demonstrated that the small deformation assumption does not suit the modelling of braided fibres, where large geometrical rotation exists. Similarly, representing fibre as an isotropic material does not provide the correct mechanical behaviour. However, using large deformation theory based on small strains and large rotations and representing fibres as transversely isotropic materials proves a reliable method of studying them.

This research raises various challenges for future studies. Transversely isotropic materials can be challenging, as singularities are formed in local and global stiffness matrices. Consequently, the global matrix is subject to ill-conditioning and poor convergence results. Modelling of braided fibres becomes more difficult as geometry becomes more complex. While the embedding process was observed in the three plaited model, this was not observed in the T12 model. It is therefore recommended that complex braided geometries are modelled as realistically as possible.

Chapter 6

Modelling of braided rope reinforced concrete

This chapter will demonstrate the techniques developed in Chapters 4 and 5 to numerically reproduce the pull-out experiments explained in Chapter 3 using finite element technology. This is categorised into three main parts. The first section provides a brief introduction highlighting the motivation behind modelling continuous fibre reinforced concrete and the second provides an appraisal of how continuous fibres embedded in concrete are modelled. In the third section, two examples are given to aid a numerical understanding of the bond behaviour between fibres and other materials, and to simulate a similar pull-out experiment of a ribbed braided rope embedded in concrete. A brief summary and suggestions for future work are given at the end of this chapter.

6.1 Introduction

One of the major goals of this research was to develop a numerical technique to model continuous fibre reinforced concrete. From Chapter 3, it was learnt that ribbed braided fibre reinforcement (RBFR) is a potential system for reinforcing structural concrete. Producing more experimental and numerical work to understand the mechanics of ribbed braided fibre reinforcement embedded in concrete is necessary to assure the feasibility, durability and reliability of such a system before its commercialisation. It is also expected that this will contribute to new research to develop fire-resistant concrete structure elements using RBFR and high-performance concrete[111].

This thesis investigated and proposed the use of hierarchical higher order (HO) interface elements to simulate de-bonding between the fibres and the concrete. As discussed in Chapter 4, localised p-refinement of the interface was made possible by using hierarchical HO interface elements, and non-linearities can be approximated accurately using the least computational power. This was studied by investigating the pull-out behaviour of a straight strand embedded in concrete (see Section 6.3.1). After understanding how hierarchical HO interface elements can be useful to model de-bonding between two different materials, all the numerical techniques developed and discussed in this thesis were brought together to simulate the pull-out behaviour of RBFR embedded in concrete. Numerical results were compared with those obtained in the experimental investigation conducted in Chapter 3.

6.2 Appraisal

This section is divided into two main parts. First, a summary of how elastic transversely isotropic materials are studied using the FE technology as discussed in Chapter 5. Second, an appraisal of how hierarchical HO an interface element using cohesive laws, as discussed in Chapter 4, was used to simulate de-bonding behaviour between fibres and concrete.

As discussed in Section 5.6 (Example 2), sinnet braided fibres can be homogenised into an elastic transversely isotropic material. This assumption was made on the basis that the overall mechanical behaviour can be represented by transverse isotropy. In MoFEM, any finite element domain representing elastic isotropic material is set up in two stages. The first is the pre-processing stage described in Algorithm 3, where the first part of this algorithm is handled by the user in Cubit, and the second part is automatically handled by a program written for MoFEM. The second stage is where

MoFEM automatically reads the fibre directions from the potential flow velocities and aligns transverse isotropy accordingly (see Section 5.3). From Chapter 5, it was learnt that the transversely isotropic stiffness matrix becomes singular as the ratio between E_p and E_z increases and the global stiffness matrix will be ill-conditioned. The consequence is a poor rate of convergence. Further studies on this numerical limitation are necessary.

It can be assumed that fibres embedded in concrete exhibit small strains and small rotations. Small deformation formulation is therefore sufficient. Although in Section 3.3.3, the concrete of RBFR pull-out experienced cracking, the first stage was to investigate the bond adhesion which the rib-shaped interface between RBFR and concrete provides during pull-out testing. Therefore, in this Chapter, concrete was assumed to be a linear elastic material. Concrete confinement action onto the bond slip resistance is thus controlled by the normal penalty stiffness of the interface element, as studied in the results of Section 6.3.2. The second stage, not covered in this thesis, would be to investigate the pull-out when considering plasticity in concrete that captures any fracturing in concrete.

The bond behaviour between fibres and concrete was simulated using cohesive elements. As explained in Section 4.2.2, cohesive elements provide traction resistance between two finite elements that are separated from each other. In this thesis, a linear damage cohesive model was used in pull-out numerical experiments to simulate the bond behaviour between fibres and concrete. Therefore the friction contribution is simplified as part of the adhesion strength and a frictionless state is achieved after full de-bonding. A linear cohesive law is governed by three parameters only: the penalty stiffness (E_o) and the maximum traction resistance (f_t) of the interface before de-bonding is initiated; and the fracture energy (G_f), which is dissipated during de-bonding. f_t and G_f are selected to represent the de-bonding mechanism between fibres and concrete. The relative gap opening between the fibres and concrete that governs the traction-separation law was computed based on Equation 4.33 (see Section 4.2.2), and $\beta = 1$ was selected. This means that both shear gap openings (Mode II and III) and normal gap opening (Mode I) will contribute to the de-bonding between fibres and concrete. In such cases, Mode I is mainly governed by the stiffness and Poisson's ratio in the transverse plane (E_p and ν_p respectively) and the normal penalty stiffness component (D_n- see matrix 4.12 in Section 4.2.1) of the interface element of the strand. To assure that the fibre domain does not interpenetrate with the concrete domain (therefore $\Delta u_n \geq 0$), D_n was a hundred times the tangential stiffness (D_{t_1} and D_{t_2}).

In both examples given in this chapter, hierarchical HO interface elements (see Chapter 4) were inserted between the different materials. A feasibility study was conducted on the use of hierarchical HO interface elements in the context of pull-out problems (see Section 6.3.1). From Section 4.2.3, it was concluded that hierarchical HO interface elements are useful when they experience complex deformations, while localised p-refinement is useful in assigning the minimum polynomial order for every interface element without mitigating the accuracy of the solution.

Once the interface elements were inserted, and the transverse isotropy and cohesive model were assigned, the equations of linear momentum were solved, and the non-linear system of equations was solved using PetSc SNES Newton solver. The arc-length method, controlled by the gap opening of the interface, was used without running into problems of convergence[5]. Numerical problems larger than 5000 DOFs were solved on multiple on Intel Xeon® CPU E7- 4830 processors. Partitioning in MoFEM was performed automatically using the ParaMETIS library for a given number of partitions. MUMPS[8] package solver was used as a parallelised pre-conditioner for sparse matrices.

6.3 Example

Two examples are given in this section. The first is a feasibility study of the use of hierarchical higher order interface elements for modelling the pull-out behaviour of fibres embedded in concrete. The second is the study of bond behaviour between a single ribbed strand embedded in concrete (similar to the RBFR developed in Chapter 3) using all the numerical techniques developed/discussed in this thesis.

6.3.1 Fibre strand embedded in concrete

A pull-out test of a simple 10mm diameter fibre strand embedded in a 100mm concrete cube (model denoted as FEIC) was investigated (Figure 6-1). The fibre strand was modelled as a transversely isotropic material and the concrete as an isotropic material (Parameters defined in Table 6.2). Full shear contribution to the damage model was assumed ($\beta = 1$ in Equation 4.33). A linear damage model with parameters give in Table 6.2 was used to describe the kinematics of the interface between fibre and concrete. During pull-out, the top face of the concrete cube was fully restrained from moving, while a pull-out force acted on the top end of the strand, and restrained laterally to allow only upward and downward movement.

Model No.	**Transversal stiffness of fibre**	**Transversal Poisson's ratio**	**Damage Model**
	E_p $[N\,mm^{-2}]$	ν_{pz}	G_f $[N\,mm^{-1}]$, f_t $[N\,mm^{-2}]$, E_o $[N\,mm^{-2}]$
FEIC_10k_A/_PO2	$10,000$	0.1	2.5, 5.0, 1000
FEIC_10k_B/_PO2	$10,000$	0.1	2.5, 5.0, 1000
FEIC_10k_C	$10,000$	0.1	2.5, 5.0, 1000
FEIC_25k_B	$25,000$	0.1	2.5, 5.0, 1000
FEIC_50k_B	$50,000$	0.1	2.5, 5.0, 1000
FEIC_135k_B	$135,000$	0.1	2.5, 5.0, 1000
FEIC_1k_B_1	$1,000$	0.1	2.5, 5.0, 25
FEIC_10k_B_1	$10,000$	0.1	2.5, 5.0, 100
FEIC_1k_B_2	$1,000$	0.3	2.5, 5.0, 25
FEIC_10k_B_2	$10,000$	0.3	2.5, 5.0, 100
FEIC_135k_B_2	$135,000$	0.3	2.5, 5.0, 100

Table 6.1: List of the FEIC models

To reduce the computational effort, a quarter of the model shown in Figure 6-1 was considered for the FE analysis. Axis-symmetric boundary conditions were used on

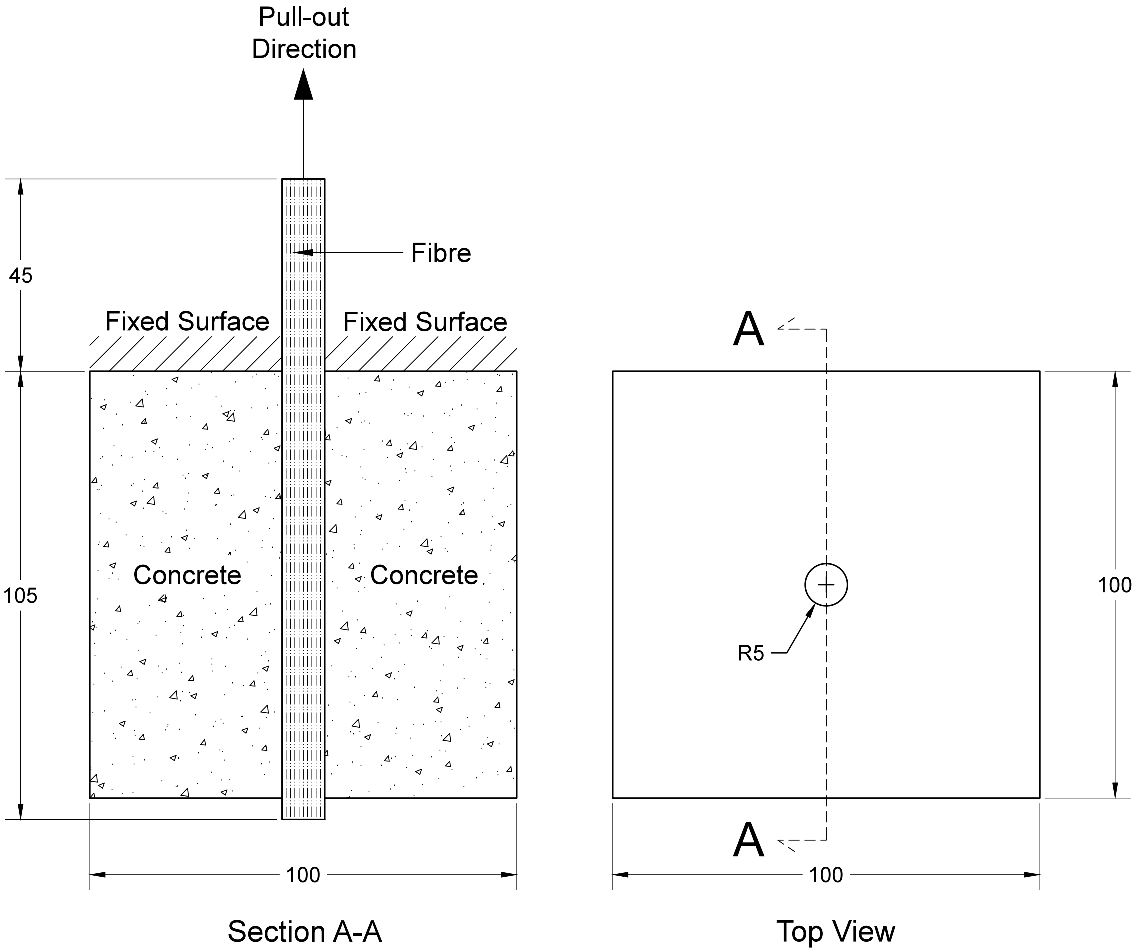

Figure 6-1: Pull-out model of fibre strand embedded in concrete

both sides of axis-symmetry of the meshed models. In the pre-processing stage, the interface elements were inserted between the strand and concrete, and fibre directions were determined. The pull-out analysis was conducted using small deformation formulation. Eleven different models (Table 6.1) were examined with various parameters as follows. Models FEIC_[10k/25k/50k/135k]_B will examine the influence of transverse plane stiffness (E_p) on the bond strength between fibres and concrete, while models FEIC_10k_A, FEIC_10k_A_PO2, FEIC_10k_B and FEIC_10k_C examine the influence of local and global enrichment (summarised in Table 6.3) on the overall pull-out behaviour. Models FEIC_1k_B_1, FEIC_10k_B_1, FEIC_1k_B_2, FEIC_10k_B_2 and FEIC_135k_A_2 will examine the influence of ν_{pz} on the pull-out behaviour. Due to the convergence problem, E_o was reduced as given in Table

Transverse Isotropy (Fibres)	**Isotropic** (Concrete)
$E_z = 135,000\,N\,mm^{-2}$	$E = 17,000\,N\,mm^{-2}$
$\nu_p = 0.4$	$\nu = 0.1$
$G_{zp} = \frac{E_z}{2(1+\nu_{pz})}$	
E_p and ν_{pz} given in Table 6.1	

Table 6.2: Material parameters for the FEIC models

6.1.

Model No.	h-refinement	p-refinement	No. of DOFs
FEIC_10k_A	none	none	1687
FEIC_10k_A_PO2	none	uniform 2nd order	10204
FEIC_[10/25/50/125k]_B	localized at interface	none	3835
FEIC_10k_B_PO2	localized at interface	uniform 2nd order	23677
FEIC_10k_C	uniform	none	10204
FEIC_1k_B_[1/2]	localized at interface	none	3835
FEIC_1k_B_1_PO2	localized at interface	uniform 2nd order	23677

Table 6.3: Local and global enrichment of FEIC models

Results

The pull-out forces obtained from all the FE analysis were multiplied by four to represent the entire model shown in Figure 6-1 and reported in Figures 6-5 and 6-7. Models FEIC_10k_B, FEIC_10k_A_PO2 and FEIC_10k_C achieved a maximum pull-out force of 14672N, 14084N and 13537N respectively, which reflects the bond strength of $f_t = 5Nmm^{-2}$ acting on the bonded area $785.4mm^2$ between fibre and concrete.

It was found out that the transversal stiffness (E_p) does not have a significant influence on Mode I de-bonding if the Poisson's ratio between the principal axis and transverse plane ν_{pz} is as small as 0.1 (see Figure 6-5). If ν_{pz} is increased to 0.3, the influence of strain in the principal axis of the fibre is more significant on the strain in the transverse plane, and therefore activates Mode I de-bonding along with Mode II/III. While the overall difference is very small when comparing FEIC_10k_B_1 and FEIC_10k_B_2 (both have $E_p = 10,000$, but with $\nu_{pz} = 0.1$ and 0.3 respectively), this will significantly change as the transverse stiffness (E_p) is reduced in

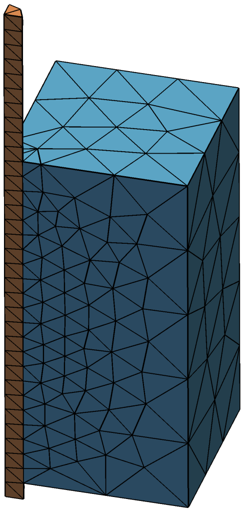

Figure 6-2: Mesh for FEIC_10k_A and FEIC_10k_A_PO2

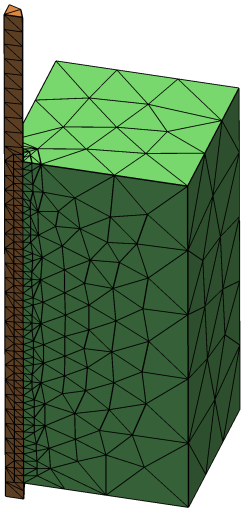

Figure 6-3: Mesh for FEIC_10k_B/_PO2 and FEIC_25k_B/ _50k_B/_135k_B (localised h-refinement)

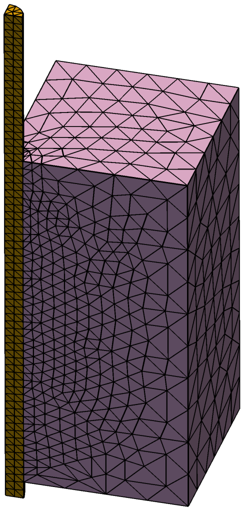

Figure 6-4: Mesh for FEIC_10k_C (uniform h-refinement)

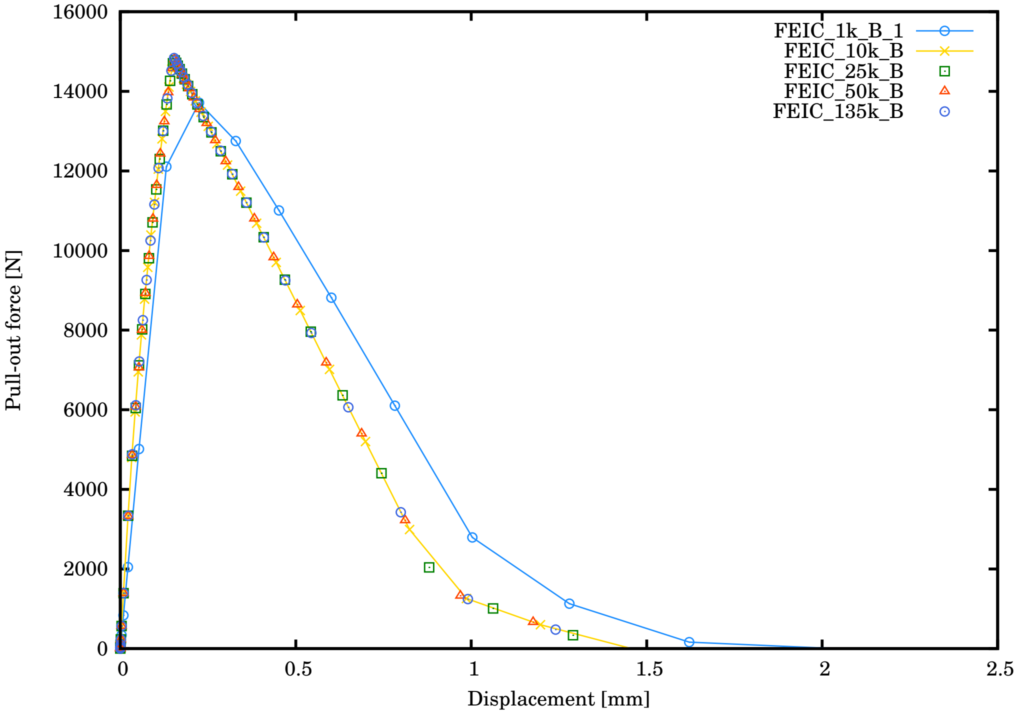

Figure 6-5: Pull-out load-displacement curve for FEIC Models varying E_p in fibre

Models FEIC_1k_B_1 and FEIC_1k_B_2 as shown in Figure 6-6. It was observed that the rate of convergence for every load step increases as E_p is reduced and ν_{pz} is increased. This is due to an increase in the conditioning number of the global stiffness matrix, resulting in ill-conditioning of the inverse matrix.

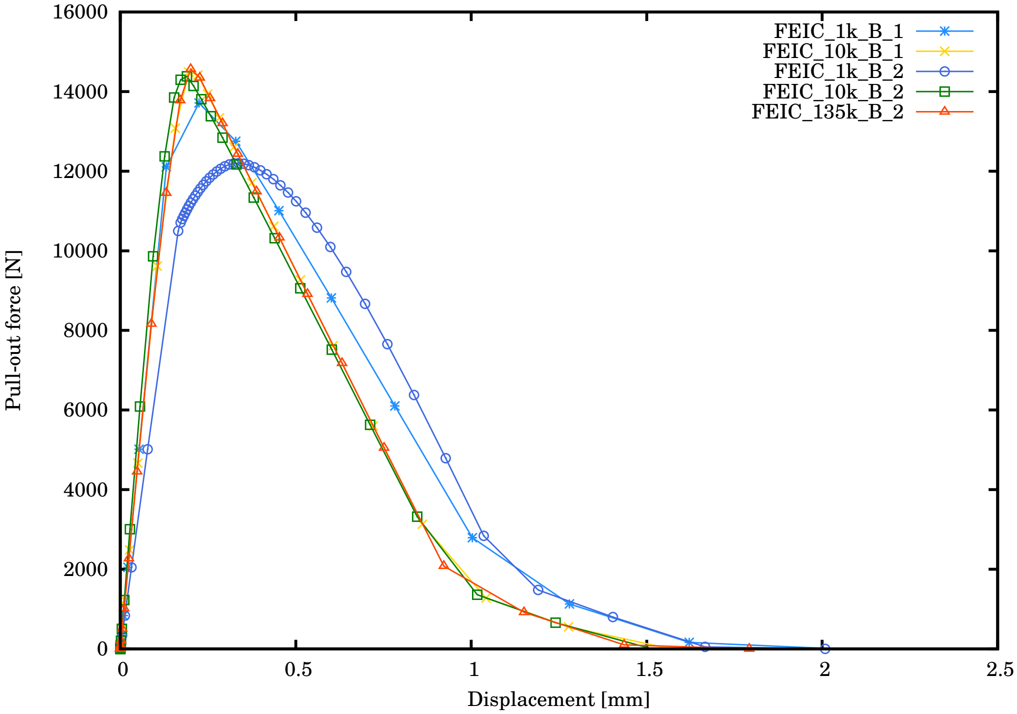

Figure 6-6: Pull-out load-displacement curve for FEIC Models with different ν_{pz} and E_p

The second part of this investigation was to determine what the benefit of h- and p-refinement on the overall pull-out behaviour is. It was found out that p-refinement did not influence the overall pull-out behaviour when E_p is larger than $10,000 Nmm^{-2}$ (FEIC_10k_A_PO2 and FEIC_10k_B_PO2). However, as E_p reduces to approximately $1000 Nmm^{-2}$, as discussed previously, Mode I starts contributing to de-bonding damage. Furthermore, p-refinement will influence the pull-out behaviour as shown between FEIC_1k_B_1 and FEIC_1k_B_1_PO2 in Figure 6-7. H-refinement was proven to be a more effective FE enrichment as the pull-out models FEIC_10k_B_PO2 and FEIC_10k_A_PO2 were subjected to localised and uniform h-refinement as shown in Figure 6-7.

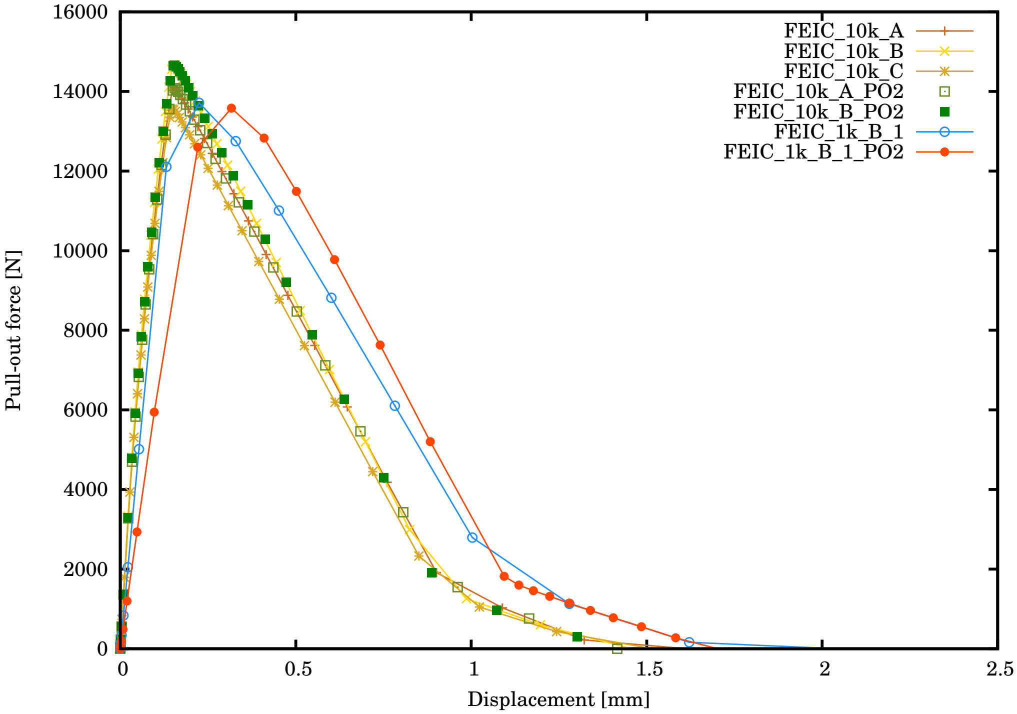

Figure 6-7: Pull-out load-displacement curve for FEIC Models having h-, p- and hp-refinement

It can thus be concluded that while h-refinement is always necessary to achieve an accurate solution, p-refinement is only necessary as Mode I starts to contribute to the damaging of the interface. Further studies are necessary to determine whether hierarchical HO enrichment is useful when fibres are made from soft material and when cohesive models representing the interface are non-linear.

6.3.2 Ribbed braided fibre embedded in concrete

The second example discussed in this chapter is a 'replica' of the pull-out experiments of the proposed and investigated RBFR (see Chapter 3). This consists of a transversely isotropic rope (replicating a homogenised sinnet rope) embedded in a concrete cylinder, with a designated bonding area between rope and concrete, measuring five times the rope's diameter in length. The rope was ribbed by placing a glass bead in the centre of the bonding area as shown in Figures 6-8 and 6-9(b).

A quarter of the aforementioned problem was meshed in Cubit (FIC Model), generat-

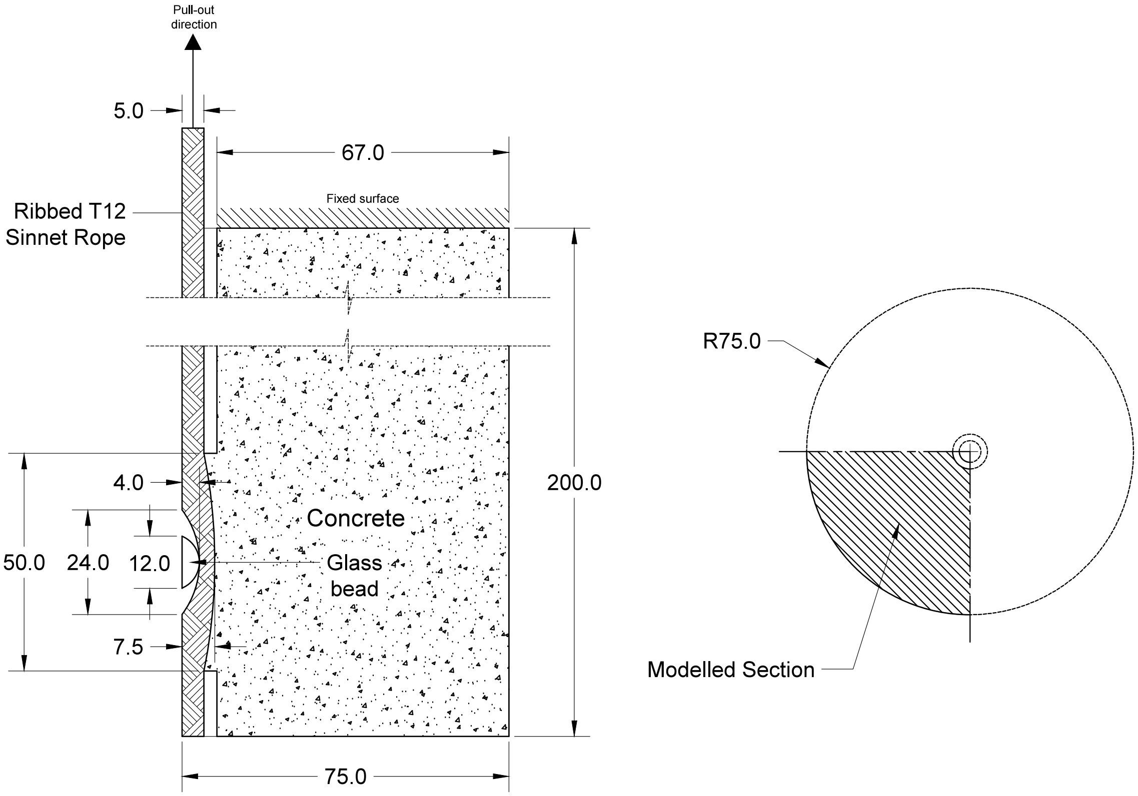

Figure 6-8: Pull-out model of the braided fibre reinforced concrete

ing 1049, 1298 and 194 of tetrahedral finite elements for the rope, concrete, and glass bead respectively. An axisymmetric boundary condition was applied to the axisymmetric planes, the top face of the concrete was fully constrained from moving, and an upward pull-out force was applied at the top end of the rope.

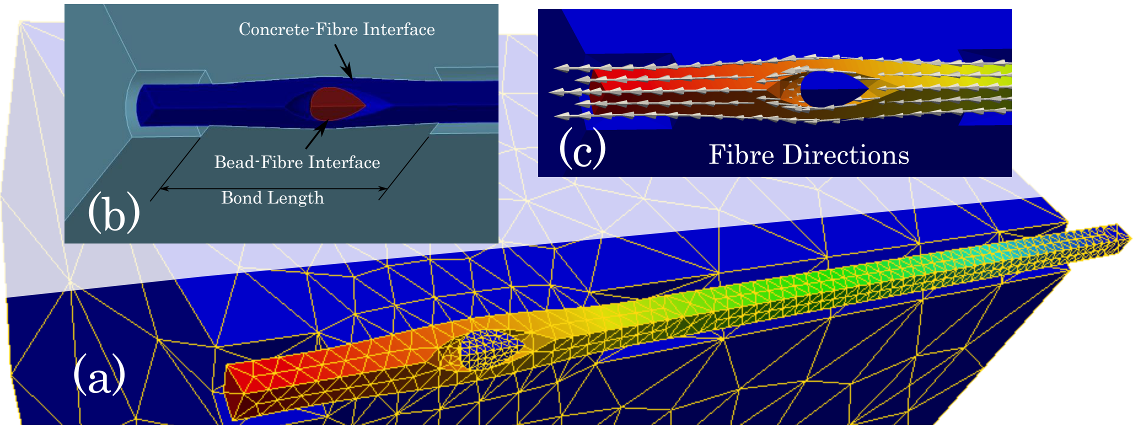

Figure 6-9: (a) Mesh representation of the FIC model; (b) detail at ribbed bond; (c) fibre directions

The rope was represented as an elastic transversely isotropic material that reflects the kinematics of a homogenised sinnet rope, as explained in Section 5.6.2. Three different transversal plane stiffness values $E_p = 1000$, 5000 and $50,000 Nmm^{-2}$ were used in models FIC_1k_50, FIC_5k_50 and FIC_50k_[05/50/50_P2/500] respectively. The concrete and glass bead were considered as elastic isotropic materials. Material parameters for the rope, concrete and glass bead are summarised in Table 6.4. Large-displacement formulation base on small strains/large rotations was used (see Section 5.5).

Interface elements were inserted between rope and concrete, and rope and glass bead (see Figure 6-9(b)). A linear constitutive damage model, with parameters given in Table 6.5, was used to represent the combined adhesion and friction contribution of the rope-concrete bond mechanism (see Section 2.2.1). The post failure friction is considered to be insignificant to the overall structural performance of ribbed braided fibre reinforced concrete. Three different normal penalty stiffness values $E_{o_n} = 5$, 50 and $500 Nmm^{-2}$ were used on models FIC_50k_05, FIC_[1k/5k/50k]_50 and FIC_50k_500 respectively to investigate how this influenced the overall pull-out strength of the model. The tangential penalty stiffness values $E_{o_{t1}}$ and $E_{o_{t2}}$ remained constant in all models. The fracture energy G_f given in Table 6.5 is approximately the bond energy dissipated in the experimental samples TR10, considering a bond stress of 7.22MPa (friction contribution is included as part of the adhesion to maintain a simple linear damage model) and assuming that the bond slip at the interface contribution for both Mode I, II and III (see Equation 4.33) is approximately 0.69mm. This is a simplified approach, which does not take into account the influence of confinement on the bond stress-slip response. This is an estimate, however, and adjustments might be required for limited experimental data.

Rope (Transversely Isotropic)	**Concrete** (Isotropic)	**Glass** (Isotropic)
E_p - varies (see Table 6.5)	$E = 17,000\, N\, mm^{-2}$	$E = 50,000\, N\, mm^{-2}$
$E_z = 135,000\, N\, mm^{-2}$	$\nu = 0.15$	$\nu = 0.1$
$\nu_p = 0.4$		
$\nu_{pz} = 0.3$		

Table 6.4: Material parameters for the FIC models

Model No.	**Transversal stiffness of fibre**	**Damage Model**
	E_p $[N\, mm^{-2}]$	G_f $[N\, mm^{-1}]$, f_t $[N\, mm^{-2}]$, $(E_{o_n}, E_{o_{t1}}, E_{o_{t2}})[N\, mm^{-2}]$
FIC_1k_50	$1,000$	2.5, 5.0, (50.0,1.0,1.0)
FIC_5k_50	$5,000$	2.5, 5.0, (50.0,1.0,1.0)
FIC_50k_05	$50,000$	2.5, 5.0, (5.0,1.0,1.0)
FIC_50k_50/_p2	$50,000$	2.5, 5.0, (50.0,1.0,1.0)
FIC_50k_500	$50,000$	2.5, 5.0, (500.0,1.0,1.0)

Table 6.5: List of the FIC models

Results

Finite element analysis of all models, given in Table 6.5, were conducted in MoFEM, while post-processing was done in ParaView. This section reports and discusses the results. The initial loading stage behaved elastically until the maximum pull-out resistance was achieved. This behaviour reflects the elastic response of both the rope and concrete. Its gradient directly depends on the selected penalty stiffness E_{o_n} as shown in the load-displacement curve in Figure 6-10. At this stage, it is worth reiterating that this behaviour is similar to the initial loading stage of the experimental pull-out investigation of TR10 models conducted in Chapter 3. This was due to the pre-stressing of braided ropes that ensured maximum embedment of the braided fibres, after which the ropes behaved elastically.

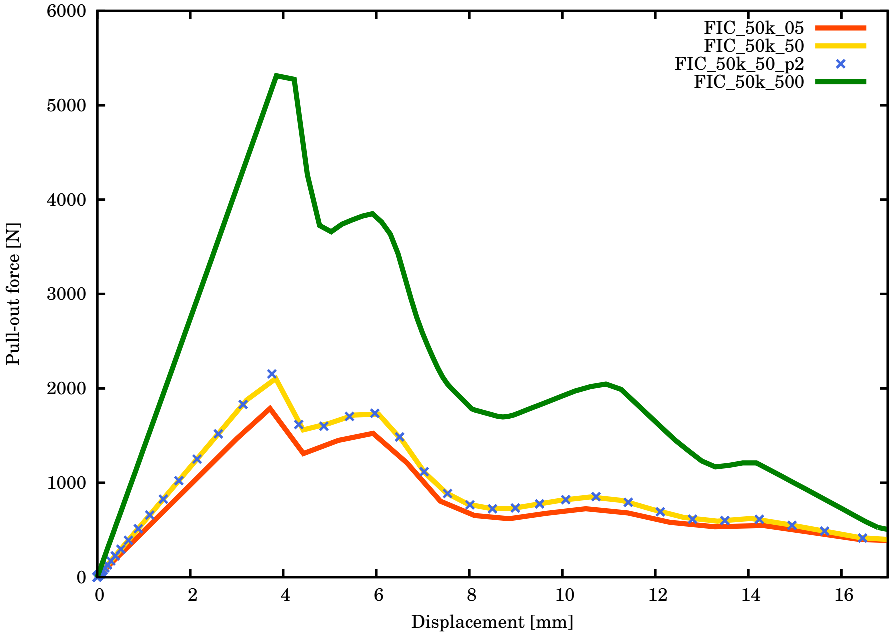

Figure 6-10: Load-displacement curve for the FIC_50k models

After the loading stage, it was noted that the de-bonding behaviour was similar in all models. After a maximum pull-out strength was obtained, cycles of softening and stiffening were observed during de-bonding of the rope from concrete. This was due to the interlocking effect generated by the presence of the glass bead. Towards the end on total de-bonding, a quasi-uniform stiffness was observed in Figure 6-10, and this is due to the permanent attachment of the interface nodes located at the bottom of the bonding area which was also recorded in the previous example given in Section 6.2.

It was discovered that the normal penalty stiffness E_{o_n} plays an important role in achieving the correct pull-out resistance and taking account of the concrete confinement contribution. If E_{o_n} is very small, as in models FIC_50k_05 and FIC_50k_50, the interface is mainly governed by Mode I separation (Figure 6-11(b)). The fibre domain penetrates into the concrete domain and pre-de-bonding failure results, resulting in smaller pull-out force. On the contrary, using high E_{o_n} constrains the interface damage to governance by Mode II and III separation (Figure 6-11(b)). This leads to a realistic representation of the contribution that concrete confinement makes to the bond strength resistance during the pull-out action of ribbed reinforcement system. It was discovered that the ratio between E_{o_n} and E_p (transversal plane stiffness of fibre) plays an important role in the bond adhesion of pull-out problems. If $\frac{E_{o_n}}{E_p} \lessapprox 1$, this would provide the wrong maximum pull-out force (e.x. models FIC_50k_05 and FIC_50k_50). Moreover, if $\frac{E_{o_n}}{E_p} \gtrapprox 1$, a correct maximum pull-out force would be achieved, but its magnitude would depend on E_p (e.x. model FIC_50k_500).

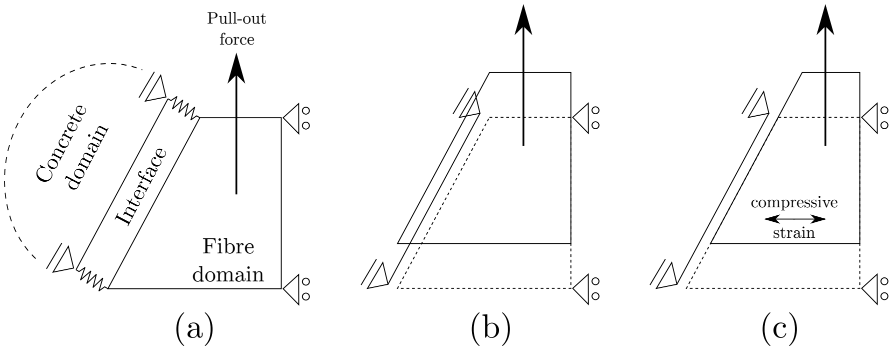

Figure 6-11: (a) Represention of the interface between fibre and concrete ; (b) Interface damage governed by Mode I (penetration of fibre and concrete domain); (c) Interface damage governed by Mode II and III

In models, FIC_1k_50, FIC_5k_50 and FIC_50k_50, where de-bonding was governed by Mode I failure, the change of the transversal stiffness E_p did not influence the maximum pull-out resistance of the de-bonding failure, as shown in Figure 6-12. While similar de-bonding behaviour was observed in all the three models, the rate of convergence reduces significantly as E_p reduces. This is due to the ill-conditioning of the global stiffness matrix as discussed in the previous example given in Section 6.2. P-refinement conducted in model FIC_50k_50_p2 did not provide any improvement in the numerical solution when compared to load-displacement curve of model FIC_50k_50 given in Figure 6-10.

Similar patterns in the pull-out behaviour of the RBFR system were visually observed between the numerical and experimental work. It is thought that a linear damage model is sufficient to replicate these types of problems, but further investigation could

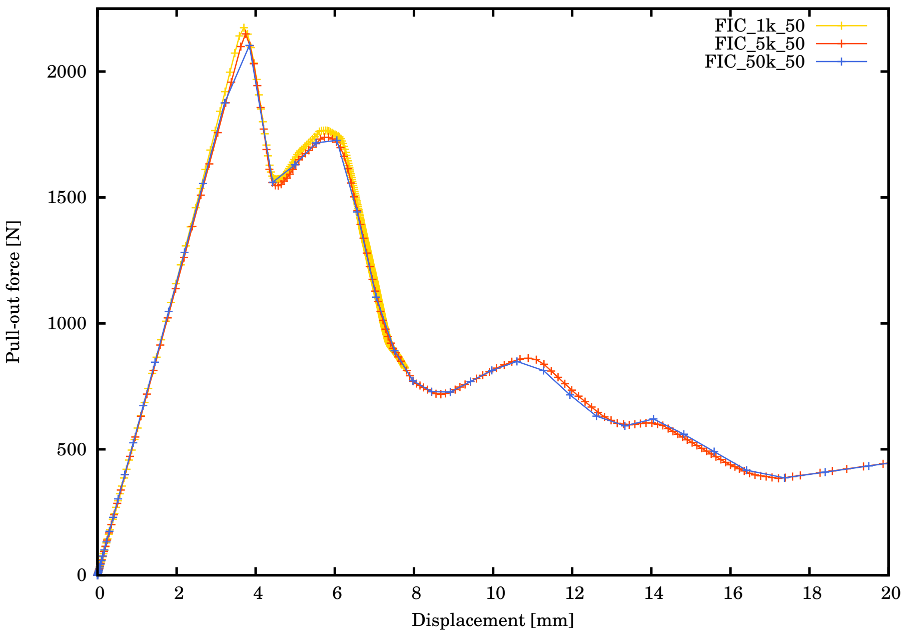

Figure 6-12: Load-displacement curve comparison between the FIC_1k, FIC_5k and FIC_50k models

use more complex damage models. In particular, the influence of confinement on the bond stress-slip response should be taken in to account.

6.4 Summary and suggestions

This chapter demonstrated how pull-out of fibres embedded in concrete can be numerically simulated. This was made possible by the methodologies developed in Chapters 4 and 5.

The first set of numerical pull-out analyses was conducted to examine the benefits of p-, h- and hp-refinement of the interface. It was found out that p-refinement of linear damaging cohesive elements using hierarchical HO interface elements was not useful in improving the numerical accuracy of pull-out problems. Further work is necessary to determine whether hierarchical HO interface elements can be useful in more complex damaging cohesive elements. On the contrary, uniform h-refinement was an effective way to provide better numerical accuracy of similar problems. Although localised h-refinement provided similar results to uniform h-refinement, computational efficiency was doubled. It was also found that the transversal stiffness E_p of fibres does not influence the bond behaviour in similar cases, but the rate of convergence reduces significantly as the ratio between E_p and E_z increases.

The second set of experiments was conducted to study numerically the pull-out behaviour RBFR system developed in Chapter 3. Similar to the first set of experiments, the bond adhesion between the fibres and concrete was represented using cohesive elements with a linear damage constitutive model. The overall numerical pull-out response has features in common with the experimental TR10 samples discussed in Chapter 3. While no direct relationship can be stated as the parameters of the linear damage model require fine tuning to achieve quantitatively similar results, it can be concluded that such a damage model can provide a good representation of the bond behaviour between the rope and concrete during pull-out. From a numerical point of view, it was observed that the normal penalty stiffness E_{o_n} of the interface element should be higher than the transversal stiffness E_p of the fibres in order to achieve a true representation of the maximum pull-out resistance. If E_{o_n} is lower than E_p, the damaging of the cohesive elements will be governed by Mode I gap opening, and pre-failure is obtained before the true de-bonding mechanism of the RBFR system.

Although a linear damage model was sufficient to represent the de-bonding of the pull-out behaviour of the RBFR system, further tests using different damage models may be conducted to achieve more alike behaviour. It is suggested that these numerical works be expanded to include problems where two or more ribs with different dimensions are used, and to determine how these different parameters influence the total pull-out behaviour of the RBFR system. To further enhance the numerical procedure, fracture modelling for concrete should be introduced to simulate the fractures obtained in experimental studies.

Chapter 7

Conclusions

This thesis proposes ribbed braided fibre reinforcement (RBFR) for concrete structures. This investigated both numerically and experimentally. These consist of carbon, Technora, and/or alkaline resistant glass fibres braided over a series of glass beads to form high strength ribbed reinforcements. Braiding is necessary to mechanically bind the fibres together, unlike fibre reinforced polymers (FRPs) where fibres are bound using a polymeric resin matrix, and ribs are necessary to enhance the reinforcement bond adhesion with concrete. These types of fibres consist only of fire and corrosion resistant materials, and can be used to produce fire resistant RBFR, unlike FRP rebars which quickly disintegrate at elevated temperatures[114;113]. It is thought that RBFR and ultrahigh performance fibre reinforced concrete (HPFRC) can produce extremely fire-resistant concrete structures. These types of fibres are also famous for their high strength to weight ratio and can produce a magnetic induction-free environment.

RBFR was experimentally tested by performing a pull-out test of a single ribbed twelve strand Technora sinnet rope embedded in a concrete cylinder. The ribbing effect was formed by inserting a glass bead into the sinnet, and then situated in the designated bonding area. These pull-out experiments were compared with similar pull-out tests using plain (no ribbing) twelve strand Technora sinnet and plain Siltex carbon fibre ropes embedded in concrete. Initial investigations demonstrated that bond strength depends on the ropes' surface texture and the compactness of braided strands. RBFR obtained 66% bond strength compared to an equivalent steel rebar, and 550% bond strength compared to a plain Technora rope embedded in concrete. The optimisation of the RBFR system, for example by adjusting different dimensions and material parameters, is essential but beyond the scope of this thesis. Therefore further studies are strongly recommended.

The mechanical behaviour of braided fibres is a poorly understood area, especially when new materials such as carbon, glass and Technora fibres are used. Moreover, when the use of ropes is modified their new mechanical behaviour needs to be investigated. This was observed in the proposal of the RBFR system, with the inclusion of beads providing new physical phenomena for exploration. Abrasion damage of RBFR with concrete was neglected on the assumption that pre-stressing of reinforcement will provide rigid bonding against concrete.

This thesis used a newly developed numerical tool to simulate braided fibres, and proposes, eventually, the RBFR system. The first challenge was to generate a finite element domain to represent braided fibres. Dynamic and efficient algorithms were written in Cubit to generate three strand plait braids and twelve strand sinnet ropes. It was thought that braided geometries can be numerically pre-stressed. Unfortunately, however, this is not possible for all geometries, as rigid lattice-like structures can form. It is recommended that braided geometries are modelled as tightly as possible. A linear elastic transverse isotropic constitutive material model based on large rotations and small strains (St Venant Kirchhoff strain energy density function) finite deformation formulation was used to study the kinematics of braided fibres. Based on the assumption that the contact area between strands does not vary significantly, cohesive elements were used to simulate the mechanical interaction between the strands. Due to the use of carbon and Technora fibres, that have very low coefficient of friction, free sliding between the strands was assumed. The efficacy of this was demonstrated by modelling a tightening of a single overhand knot.

The importance of using transverse isotropy to represent fibre materials in braided geometries is demonstrated by a finite element large deformation simulation of a three plait braid under tension. This was compared with a similar model using an isotropic material, where unrealistic deformation was observed. Other tests showed that small deformation theory is not suitable for modelling braided geometries, as spurious strains are formed and unrealistic deformations can be observed. Unfortunately, transverse isotropy can produce singular stiffness matrices when the stiffness in the transverse plane varies significantly from the stiffness in the principal axis. This leads to ill-the conditioning of the global stiffness matrix. Although robust parallelised preconditioners such as MUMPs and SuperLU were used, a poor rate of convergence was still visible in large deformation problems. Hence, transversely isotropic materials should be used with precaution and this problem remains in need of further investigation.

In this thesis, linear damaging cohesive elements were used to simulate the bond behaviour between fibres and concrete. Furthermore, it was proposed hierarchical higher order interface elements. These can be useful to conduct localised p-refinement at the interface elements, providing accurate solutions without mitigating the computational performance. The formulation and approach for the use of hierarchical higher order interface elements were reported, and its feasibility was demonstrated through investigation of a 3D de-lamination problem. Hierarchical higher order interface elements were also used in the failed attempt to remove traction oscillations from interface elements next to notches. Although it was found out that hierarchical higher order interface elements were not useful to model shear damaging interface elements with a linear damage model (i.e. pull-out of fibres embedded in concrete), these can be useful for more complex damaging models. H-refinement was more useful in such cases and computational performance was improved as localised h-refinement was used, without mitigation of accuracy. Finally, the pull-out tests of the RBFR system were successfully simulated using the interface element represented by a linear damage model, and pull-out behaviour was obtained in a similar manner to the experimental investigation. The braided reinforcement was simulated as a homogenised transversely isotropic material, while concrete and glass beads were assumed to be linear elastic materials. It was learnt that the normal penalty stiffness of the interface element, should be higher than the transversal stiffness of the fibres to obtain the correct maximum pull-out force.

This experimental and computational research project has established ribbed braided fibre as a new potential reinforcement for concrete. A numerical tool was developed to model braided fibres and RBFR embedded in concrete. Further work is necessary to improve the RBFR system and to find solutions for all the highlighted issues experienced during numerical work.

Bibliography

[1] Tokyo Rope Mfg. Co. LTD. Carbon fibre composite cable. [http://www.tokyorope.co.jp/english/products/cfcc/index.html accessed 28 March 2015].

[2] M. Ainsworth and J. Coyle. Hierarchic finite element bases on unstructured tetrahedral meshes. *International Journal for Numerical Methods in Engineering*, 58(14):2103–2130, Dec. 2003. http://dx.doi.org/10.1002/nme.847.

[3] S. Akihama, T. Suenaga, and T. Banno. The behaviour of carbon fibre reinforced cement composites in direct tension, 1984. http://dx.doi.org/10.1016/0262-5075(84)90004-6.

[4] G. Alfano and M. A. Crisfield. Finite element interface models for the delamination analysis of laminated composites: mechanical and computational issues. *International Journal for Numerical Methods in Engineering*, 50(7):1701–1736, Mar. 2001. http://dx.doi.org/10.1002/nme.93.

[5] G. Alfano and M. A. Crisfield. Solution strategies for the delamination analysis based on a combination of local-control arc-length and line searches. *International Journal for Numerical Methods in Engineering*, 58(7):999–1048, Oct. 2003. http://dx.doi.org/10.1002/nme.806.

[6] G. Alfano and E. Sacco. Combining interface damage and friction in a cohesive-zone model. *International Journal for Numerical Methods in Engineering*, 68(5):542–582, 2006. http://dx.doi.org/10.1002/nme.1728.

[7] M. A. Ali, A. J. Majumdar, and D. L. Rayment. Carbon fibre reinforcement of cement. *Cement and Concrete Research*, 2:201–212, 1972. http://dx.doi.org/10.1016/0008-8846(72)90042-7.

[8] P. R. Amestoy, I. S. Duff, and J. Y. L'Excellent. Mumps multifrontal massively parallel solver version 2.0, 1998.

[9] S. Aydin, H. Yazici, and B. Baradan. High temperature resistance of normal strength and autoclaved high strength mortars incorporated polypropylene and steel fibers. *Construction and Building Materials*, 22:504–512, 2008. http://dx.doi.org/10.1016/j.conbuildmat.2006.11.003.

[10] I. Babuška and B. Q. Guo. The h, p and hp version of the finite element method basic theory and applications. *Advances in Engineering Software*, 15(3-4):159–174, 1992. http://dx.doi.org/10.1016/0965-9978(92)90097-y.

[11] I. Babuška and M. Suri. On locking and robustness in the finite element method, May 1992. http://dx.doi.org/10.1137/0729075.

[12] A. Badanoiu and J. Holmgren. Cementitious composites reinforced with continuous carbon fibres for strengthening of concrete structures. *Cement and Concrete Composites*, 25:387–394, 2003. http://dx.doi.org/10.1016/S0958-9465(02)00054-9.

[13] S. Balay, S. Abhyankar, M. F. Adams, J. Brown, P. Brune, K. Buschelman, L. Dalcin, V. Eijkhout, W. D. Gropp, D. Kaushik, M. G. Knepley, L. C. McInnes, K. Rupp, B. F. Smith, S. Zampini, H. Zhang, and H. Zhang. PETSc users manual. Technical Report ANL-95/11 - Revision 3.7, Argonne National Laboratory, 2016.

[14] R. V. Balendran, F. P. Zhou, A. Nadeem, and A. Y. T. Leung. Influence of steel fibres on strength and ductility of normal and lightweight high strength concrete. *Building and Environment*, 37:1361–1367, 2002. http://dx.doi.org/10.1016/S0360-1323(01)00109-3.

[15] N. Banthia and J. F. Trottier. Deformed steel fiber-cementitious matrix bond under impact. *Cement and Concrete Research*, 21:158–168, 1991. http://dx.doi.org/10.1016/0008-8846(91)90042-G.

[16] K. J. Bathe and S. Ramaswamy. On three-dimensional nonlinear analysis of concrete structures. *Nuclear Engineering and Design*, 52:385–409, 1979. http://dx.doi.org/10.1016/0029-5493(79)90029-3.

[17] K. J. Bathe, J. Walczak, A. Welch, and N. Mistry. Nonlinear analysis of concrete structures. *Computers & Structures*, 32(3/4):563–590, 1989. http://dx.doi.org/10.1016/0045-7949(89)90347-7.

[18] Z. P. Bažant and B. H. Oh. Crack band theory for fracture of concrete. *Matériaux et Constructions*, 16(3):155–177, May 1983. http://dx.doi.org/10.1007/BF02486267.

[19] Z. P. Bažant. Instability, ductility and size effect in strain-softening concrete. *Journal of Engineering Mechanics Division, ASCE*, 102(2):331–344, 1976.

[20] Z. P. Bažant. Mechanics of distributed cracking. *Appl. Mech. Rev*, 39(5), 1986.

[21] Z. P. Bažant and A. A. Asghari. Constitutive law for nonlinear creep of concrete. *Journal of Engineering Mechanics Division, ASCE*, 103:113–124, 1977.

[22] Z. P. Bažant and P. Bhat. Endochronic theory of inelasticity and failure of concrete. *Journal of Engineering Mechanics Division, ASCE*, 102:701–722, 1976.

[23] Z. P. Bažant and P. Bhat. Prediction of hysteresis of reinforced concrete beams. *Journal of Structural Division, ASCE*, 103:153–167, 1977.

[24] Z. P. Bažant and B. H. Oh. Rock fracture via strain-softening finite elements. *Journal of Engineering Mechanics Division, ASCE*, 110(7):1015–1035, 1984. http://dx.doi.org/10.1061/(ASCE)0733-9399(1984)110:7(1015).

[25] Z. P. Bazžant and G. Pijaudier-Cabot. Nonlocal Continuum Damage, Localization Instability and Convergence. *Journal of Applied Mechanics*, 55(2):287–293, jun 1988. http://dx.doi.org/10.1115/1.3173674.

[26] T. Belytschko and T. Back. Pull-out processes in steel fibre reinforced cement. *International Journal for Numerical Methods in Engineering*, 45(5):601–620, 1999. http://dx.doi.org/10.1016/0010-4361(86)90266-1.

[27] E. J. Bennett, R. G. Pohto, and A. T. Mitchell. Cathodic protection system for a steel-reinforced concrete structure, 1999. http://dx.doi.org/10.1016/S0958-9465(99)90120-8.

[28] A. Bentur, S. Mindess, and S. Diamond. Pull-out processes in steel fibre reinforced cement. *International Journal of Cement Composites and Lightweight Concrete*, 7(1):29–37, 1985. http://dx.doi.org/10.1016/0262-5075(85)90024-7.

[29] A. C. Berg, L. C. Bank, M. G. Oliva, and J. S. Russell. Construction and cost analysis of an FRP reinforced concrete bridge deck. *Construction and Building Materials*, 20(8):515–526, Oct. 2006. http://dx.doi.org/10.1016/j.conbuildmat.2005.02.007.

[30] P. G. Bergan and I. Holand. Nonlinear finite element analysis of concrete structures. *Computer Methods in Applied Mechanics and Engineering*, 17/18:443–467, 1979. http://dx.doi.org/10.1016/0045-7825(79)90027-6.

[31] V. V. Bertero, E. P. Popov, and S. Viwathanatepa. Bond of reinforcing steel: Experiments and a mechanical model. In *Nonlinear behaviour of reinforced concrete spatial structures: Contributions to the IASS symposium*, Darmstadt, 1978.

[32] K. L. Biryukovich, Y. L. Biryukovich, and D. L. Biryukovich. Glass fiber reinforced cement. *Budivel'nik, Kieve, Translation by Civil Engineering Research Association*, (12), 1964.

[33] A. Briggs. Review carbon fibre-reinforced cement. *Journal of Materials Science*, 12:384–404, 1977.

[34] C. J. Brown, D. Darwin, and S. L. McCabe. Finite element fracture analysis of steel-concrete bond. Technical report, University of Kansas Center for Research, Lawrence, Kansas, 1993.

[35] J. Burkardt. Grundmann Moeller Quadrature Rules for a Simplex in M dimensions, July 2008. [http://people.sc.fsu.edu/jburkardt/c_src/simplex_gm_rule/simplex_gm_rule.html posted 15 February 2014].

[36] T. Büttner, J. Orlowsky, and M. Raupach. Textile reinforced concrete - durability issues: changes of the bond and tensile strength due to ageing. In *Brittle Matrix Composites 9*, pages 301–312, Warsaw, 2009. Woodhead Publishing Limited. http://dx.doi.org/10.1533/9781845697754.301.

[37] O. Buyukozturk. Nonlinear analysis of reinforced concrete structures. *Computers & Structures*, 7:149–156, 1977.

[38] V. Cervenka and K. H. Gerstle. Inelastic analysis of reinforced concrete panels : experimental verification and application. *IABSE publications*, 32:25–39, 1972. http://dx.doi.org/10.5169/seals-24951.

[39] P. K. Chang, Y. N. Peng, and C. L. Hwang. A design consideration for durability of high-performance concrete. *Cement and Concrete Composites*, 23:375–380, 2001. http://dx.doi.org/10.1016/S0958-9465(00)00089-5.

[40] V. Ciampi, V. V. Bertero, and E. Popov. Analytical Model tor Deformed Bar Bond under Generalized Excitations. *Proceedings IABSE Colloquium an "Advanced Mechanics in Reinforced Concrete"*, pages 53–67, 1981.

[41] V. Ciampi, R. Eligehausen, E. P. Popov, and V. V. Bertero. Analytical model for concrete anchorages of reinforcing bars under generalized excitations. Technical report, College of Engineering, University of California, Berkeley, California, 1982.

[42] A. P. Clark. Comparative bond efficiency of deformed concrete reinforcing bars. *Journal of Research of the National Bureau of Standards*, 37, Dec. 1946. http://dx.doi.org/10.14359/8754.

[43] R. W. Clough. The finite element method in plane stress analysis. In *2nd Conference on Electronic Computation, ASCE*, Pittsburgh, 1960.

[44] R. W. Clough and L. Wilson. Stress anlaysis of a gravity dam by the finite eleemnt method. In *Proceedings, Symposium on the Use of Computers in Civil Engineering*, pages 29.1–29.22, Lisbon, Portugal, 1962. Laboratorio Nacional de Engenharia Civil.

[45] R. W. Clough and L. Wilson. Stress analysis of a gravity dam by the finite element method. *Bulletin RILEM*, (19):41–54, 1963.

[46] R. Codispoti, D. V. Oliveira, R. S. Olivito, and P. B. Lourenço. Mechanical performance of natural fiber-reinforced composites for the strengthening of masonry. *Composites Part B*, 77:74–83, 2015. http://dx.doi.org/10.1016/j.compositesb.2015.03.021.

[47] E. Cosenza, G. Manfredi, and R. Realfonzo. Behavior and modeling of bond of FRP rebars to concrete. *Journal of Composites for Construction*, 1(2):40–51, 1997. http://dx.doi.org/10.1061/(ASCE)1090-0268(1997)1:2(40).

[48] A. D. Cowell, E. P. Popov, and V. V. Bertero. Effects of concrete types and loading conditions on local bond-slip relations. Technical report, College of Engineering, University of California, Berkeley, California, 1982.

[49] J. V. Cox. *Development of a plasticity bond model for reinforced concrete: theory and validation for monotonic applications*. Naval Facilities Engineering Service Center, 1994.

[50] M. A. Crisfield and G. Alfano. Adaptive hierarchical enrichment for delamination fracture using a decohesive zone model. *International Journal for Nu-*

merical Methods in Engineering, 54(9):1369–1390, 2002. http://dx.doi.org/10.1002/nme.469.

[51] P. Davies, N. Lacotte, G. Kibsgaard, R. Craig, D. Cannell, S. Francois, O. Lodeho, K. Konate, S. Mills, M. Francois, A. L. Defoy, D. Durville, D. Vu, J. Gilmore, and D. Sherman. Bend over sheave durability of fibre ropes for deep sea handling operations. In *Proceedings of the ASME 2013 32nd International Conference on Ocean*, pages 1–8.

[52] R. de Borst and P. Nauta. Non-orthogonal cracks in a smeared finite element model. *Engineering Computations*, 2(1):35–46, 1985. http://dx.doi.org/10.1108/eb023599.

[53] R. de Borst, J. C. Remmers, A. Needleman, and M. A. Abellan. Discrete vs smeared crack models for concrete fracture - Bridging the gap. *International Journal for Numerical and Analytical Methods in Geomechanics*, 28(7-8):583–607, 2004. http://dx.doi.org/10.1002/nag.374.

[54] L. Demkowicz. *Computing with hp-adaptive finite elements: Volume 1, One and two dimensional elliptic and maxwell problems*. Chapman & Hall/CRC Applied Mathematics & Nonlinear Science. CRC Press, 2006.

[55] J. A. Den Uijl and A. J. Bigaj. A bond model for ribbed bars based on concrete confinement. *Heron*, 41(3):201–226, 1996.

[56] R. Djamaluddin, S. Hino, and K. Yamaguchi. Bond capacity of grid system in unresin carbon fiber reinforcement for concrete beams. *Journal of Structural Engineering*, 50A:927–934, 2004.

[57] R. Djamaluddin, Y. Kobayashi, T. Nagahama, and T. Ohta. Application of Unresin Continuous Carbon Fibers as Flexural Reinforcement in Concrete Structures. *Doboku Gakkai Nenji Gakujutsu Koenkai Koen Gaiyoshu. 5*, 22(3):283–288, 2000.

[58] W. Dong, J. Xiao, and Y. Li. Finite element analysis of the tensile properties of 2.5d braided composites. *Materials Science and Engineering: A*, 457(1-2):199–204, may 2007. http://dx.doi.org/10.1016/j.msea.2006.12.032.

[59] A. Drach, B. Drach, and I. Tsukrov. Processing of fiber architecture data for finite element modeling of 3d woven composites. *Advances in Engineering Software*, 72:18–27, jun 2014. http://dx.doi.org/10.1016/j.advengsoft.2013.06.006.

[60] D. Durville. *Composite Reinforcements for Optimum Performance*. Elsevier, 2011. http://dx.doi.org/10.1533/9780857093714.4.461.

[61] D. Durville. Contact-friction modeling within elastic beam assemblies: an application to knot tightening. *Computational Mechanics*, 49(6):687–707, Feb. 2012. http://dx.doi.org/10.1007/s00466-012-0683-0.

[62] E. N. Dvorkin, A. M. Cuitiño, and G. Gioia. Finite elements with displacement interpolated embedded localization lines insensitive to mesh size and distortions.

International Journal for Numerical Methods in Engineering, 30(3):541–564, 1990. http://dx.doi.org/10.1002/nme.1620300311.

[63] R. Eligehausen, E. P. Popov, and V. V. Bertero. Local bond stress-slip relationships of deformed bars under generalized excitations. Technical report, College of Engineering, University of California, Berkeley, California, 1983.

[64] F. I. Faiyadh and M. A. Al-Ausi. Effect of elevated temperature on splitting tensile strength of fibre concrete. *International Journal of Cement Composites and Lightweight Concrete*, 11(3):175–178, 1989. http://dx.doi.org/10.1016/0262-5075(89)90090-0.

[65] S. Feih, E. Boiocchi, and E. Kandare. Strength degradation of glass and carbon fibres at high temperature. In *ICCM-17 Proceeding*, 2009.

[66] C. A. Felippa and B. Haugen. A unified formulation of small-strain corotational finite elements: I. Theory. *Computer Methods in Applied Mechanics and Engineering*, 194(21-24):2285–2335, June 2005. http://dx.doi.org/10.1016/j.cma.2004.07.035.

[67] P. M. Ferguson. Bond Stress-The State of the Art. *Journal of the American Concrete Insititute, ACI Committee 408*, 408:1161–1190, 1966. http://dx.doi.org/10.14359/7665.

[68] A. C. Fischer-Cripps. *Introduction to Contact Mechanics*. Springer US, 2007. http://dx.doi.org/10.1007/978-0-387-68188-7.

[69] J. R. Fried. *Polymer Science and Technology*. Prentice Hall Professional Technical Reference, 2003.

[70] H. Funke, S. Gelbrich, and A. Ehrlich. Development of a new hybrid material of textile reinforced concrete and glass fibre reinforced flastic. *Procedia Materials Science*, 2:103–110, 2013. http://dx.doi.org/10.1016/j.mspro.2013.02.013.

[71] D. Gao, D. Yan, and X. Li. Splitting strength of GGBFS concrete incorporating with steel fiber and polypropylene fiber after exposure to elevated temperatures. *Fire Safety Journal*, 54:67–73, 2012. http://dx.doi.org/10.1016/j.firesaf.2012.07.009.

[72] A. Gens, I. Carol, and E. E. Alonso. An interface element formulation for the analysis of soil-reinforcement interaction. *Computers and Geotechnics*, 7(1-2):133–151, Jan. 1988. http://dx.doi.org/10.1016/0266-352X(89)90011-6.

[73] V. T. Giner, F. J. Baeza, S. Ivorra, E. Zornoza, and O. Galao. Effect of steel and carbon fiber additions on the dynamic properties of concrete containing silica fume. *Materials and Design*, 34:332–339, 2012. http://dx.doi.org/10.1016/j.matdes.2011.07.068.

[74] Giuriani, E. Experimental investigation on the bond-slip law of deformed bars in concrete. 1981. http://dx.doi.org/10.5169/seals-26883.

[75] S. Goldfein. Plastic fibrous reinforcement for fortland cement, Technical Report No. 1757-TR. Technical report, U.S. Army Research and Development Laboratories, Fort Belvoir, 1963.

[76] C. Gonilho-Pereira, R. Fangueiro, and S. Jalali. Composite rods as a steel substitute in concrete reinforcement. In *Asia-Pacific Conference of FRP in Structures (APFIS 2007)*, pages 2–6, 2007.

[77] C. Gonilho-Pereira, R. Fangueiro, and S. Jalali. Tensile performance of braided composite rods for concrete reinforcement. In *Challenges for Civil Construction*, 2008.

[78] C. Gonilho-Pereira, R. Fangueiro, S. Jalali, M. Araújo, and P. Pina Marques. Tensile properties of braided composite rods. In *Fourth International Conference of FRP Composites in Civil Engineering (CICE 2008)*, Zurich, 2008.

[79] Y. Goto. Cracks formed in concrete around deformed tension bars. *ACI journal*, 68(4):244–251, 1971. http://dx.doi.org/10.14359/11325.

[80] C. Greer, P. Concrete Canvas, 1999. [http://www.concretecanvas.com/ accessed 28 March 2015].

[81] A. A. Griffith. The phenomena of rupture and flow in solids. *Philosophical transactions of the royal society of the Royal Society A: Mathematical, Physical and Engineering Sciences*, 1921. http://dx.doi.org/10.1098/rsta.1921.0006.

[82] H. J. Grootenboer. *Finite element analysis of two-dimensional reinforced concrete structures, taking account of non-linear physical behaviour and the developlement of discrete cracks*. PhD thesis, Delft University, 1979.

[83] A. Grundmann and H. M. Moller. Invariant integration formulas for the n-simplex by combinatorial methods. *SIAM Review*, 15(2):282–190, 1978. http://dx.doi.org/10.1137/1019132.

[84] F. Han, H. Chen, K. Jiang, W. Zhang, T. Lv, and Y. Yang. Influences of geometric patterns of 3D spacer fabric on tensile behavior of concrete canvas. *Construction and Building Materials*, 65:620–629, 2014. http://dx.doi.org/10.1016/j.conbuildmat.2014.05.041.

[85] J. Hartig, U. Häußler-Combe, and K. Schicktanz. Influence of bond properties on the tensile behaviour of Textile Reinforced Concrete. *Cement and Concrete Composites*, 30(10):898–906, 2008. http://dx.doi.org/10.1016/j.cemconcomp.2008.08.004.

[86] U. Häußler-Combe and J. Hartig. Bond and failure mechanisms of textile reinforced concrete (TRC) under uniaxial tensile loading. *Cement and Concrete Composites*, 29(4):279–289, 2007. http://dx.doi.org/10.1016/j.cemconcomp.2006.12.012.

[87] W. M. Haynes. *CRC Handbook of Chemistry and Physics, 93rd Edition*. CRC Handbook of Chemistry and Physics. Taylor & Francis, 2012.

[88] H. B. Hellweg and M. A. Crisfield. A new arc-length method for handling sharp snap-backs. *Computers & Structures*, 66(5):704–709, 1998. http://dx.doi.org/10.1016/S0045-7949(97)00077-1.

[89] C. T. Herakovich. *Mechanics of Fibrous Composites.* John Wiley & Sons, Ltd, 1998.

[90] L. R. Herrmann and J. V. Cox. Development of a plasticity bond model for reinforced concrete - Preliminary calibration and cyclic applications. Technical Report March, Naval Facilities Engineering Service Center, Port Hueneme, California, 1994.

[91] J. Hewitt, D. Brown, and R. Clarke. Modelling, evaluation and manufacture of woven composite materials. *Composites Part A: Applied Science and Manufacturing*, 27(4):295–299, jan 1996. http://dx.doi.org/10.1016/1359-835X(95)00041-Y.

[92] K. Hibbitt and Sorensen. *ABAQUS/User Subroutines Reference Guide.* Dassault Systemes Simulia Corporation, 2013.

[93] A. Hillerborg, M. Modéer, and P. E. Petersson. Analysis of crack formation and crack growth in concrete by means of fracture mechanics and finite elements. *Cement and Concrete Research*, 6(6):773–781, Nov. 1976. http://dx.doi.org/10.1016/0008-8846(76)90007-7.

[94] A. F. Horadam. Gegenbauer polynomials revisited. *Fibonacci Quart*, pages 294–299, 1985.

[95] S. Igarashi, A. Bentur, and S. Mindess. The effect of processing on the bond and interfaces in steel fiber reinforced cement composites. *Cement and Concrete Composites*, 18:313–322, 1996. http://dx.doi.org/10.1016/0958-9465(96)00022-4.

[96] C. E. Inglis. Stresses in a plate due to the presence of cracks and sharp corners. Technical report, Institution of Naval Architects, Cambridge, Mar. 1913.

[97] A. R. Ingraffea and V. E. Saouma. Numerical modeling of discrete crack propagation in reinforced and plain concrete. In *Fracture mechanics of concrete: Structural application and numerical calculation*, pages 171–225. Springer Netherlands, Dordrecht, 1985. http://dx.doi.org/10.1007/978-94-009-6152-4_4.

[98] A. C. Institute. *State-of the-Art Report on Fiber Reinforced Concrete, Reported by ACI Committee 544.* ACI, 1996.

[99] A. C. Institute. *Guide Test Methods for Fiber-Reinforced Polymers (FRPs) for Reinforcing or Strengthening Concrete Structures, Reported by ACI Committee 440.* ACI, 2004.

[100] B. S. Institution. *Eurocode 2 : Design of concrete structures, Part1-1: General rules and rules for buildings.* BSI, London, 2004.

[101] B. S. Institution. *Eurocode 2 : Design of concrete structures, Part1-2: General rules - Structural fire design*. BSI, London, 2004.

[102] B. S. Institution. *Eurocode 3 : design of steel structures, Part1-2: General rules - Structural fire design*. BSI, London, 2005.

[103] B. S. Institution. *Steel for the reinforcement of concrete. Weldable reinforcing steel. General*. BSI, London, 2005.

[104] B. S. Institution. *BS EN 12390-2:2009, Testing hardened concrete. Making and curing specimens for strength tests*. BSI, London, 2009.

[105] B. S. Institution. *BS EN 12390-3:2009, Testing hardened concrete. Compressive strength of test specimens*. BSI, London, 2009.

[106] A. International. *ASTM A944-09, Standard test method for comparing bond strength of steel reinforcing bars to concrete using beam-end specimens*. ASTM International, West Conshohocken, PA, 2004.

[107] G. R. Irwin. Fracture dynamics. *Fracturing of Metals, American Society For Metals*, pages 147–166, 1948.

[108] A. Ivanič, S. Lubej, R. Rudolf, and I. Anžel. Bond behavior of carbon-fiber yarn embedded in cement mortar. *Science and Engineering of Composite Materials*, 18(3):181–186, 2011. http://dx.doi.org/10.1515/SECM.2011.029.

[109] J. O. Jirsa. Bond and anchorage in reinforced concrete frame joints. In *Japan seminar on earthquake engineering with emphasis on the safety of reinforced concrete structures*, Berkeley, California, 1973.

[110] Kaczmarczyk, Ł., et. al. *Mesh Oriented Finite Element Method (MoFEM), Version 0.1.4*. The University of Glasgow, Glasgow, United Kingdom, 2014.

[111] P. Kalifa, G. Chene, and C. Galle. High-temperature behaviour of HPC with polypropylene fibres: From spalling to microstructure. *Cement and concrete research*, 31:1487–1499, 2001. http://dx.doi.org/10.1016/S0008-8846(01)00596-8.

[112] S. Kang and J. Kim. The relation between fiber orientation and tensile behavior in an Ultra High Performance Fiber Reinforced Cementitious Composites (UHPFRCC). *Cement and Concrete Research*, 41(10):1001–1014, 2011. http://dx.doi.org/10.1016/j.cemconres.2011.05.009.

[113] A. Katz and N. Berman. Modeling the effect of high temperature on the bond of FRP reinforcing bars to concrete. *Cement and Concrete Composites*, 22(6):433–443, Dec. 2000. http://dx.doi.org/10.1016/S0958-9465(00)00043-3.

[114] A. Katz, N. Berman, and L. C. Bank. Effect of high temperature on bond strength of FRP rebars. *Journal of Composites for Construction*, 3(2):73–81, May 1999. http://dx.doi.org10.1061/(ASCE)1090-0268(1999)3%3A2(73).

[115] O. Kayali, M. N. Haque, and B. Zhu. Some characteristics of high strength fiber reinforced lightweight aggregate concrete. *Cement and Concrete Composites*, 25:207–213, 2003. http://dx.doi.org/10.1016/S0958-9465(02)00016-1.

[116] A. Kelly. *The Optimisation of Finite Element Meshes*. PhD thesis, The University of Glasgow, 2014.

[117] E. L. Kemp and J. Wilhelm. Investigation of the parameters influencing bond cracking. *ACI JOURNAL*, page 47, 1979. http://dx.doi.org/10.14359/6936.

[118] K. Kobayashi, T. Iizuka, H. Kurachi, and K. Rokugo. Corrosion protection performance of High Performance Fiber Reinforced Cement Composites as a repair material. *Cement and Concrete Composites*, 32(6):411–420, 2010. http://dx.doi.org/10.1016/j.cemconcomp.2010.03.005.

[119] H. Krenchel and S. Shah. Applications of polypropylene fibers in Scandinavia. *Concrete International*, pages 32–34, 1985.

[120] H. G. Kwak and F. C. Filippou. Finite element analaysis of reinforced concrete structures under monotonic loads. Technical Report November, Department of Civil Engineering, University of California, Berkeley, California, 1990.

[121] Y. Kyosev. *Braiding Technology for Textiles, Principles, Design and Processes*. Woodhead Publishing Limited, 2015.

[122] K. H. Kyung and C. Meyer. Aramid fiber mesh-reinforced thin sheet response to impact loads. In H. Reinhardt and A. Naaman, editors, *High Performance Fiber Reinforced Cement Composites - HPFRCC 5*, pages 447–453, Cachan, France, 2007. RILEM Proceedings.

[123] B. J. Lahnert and K. H. Gerstle. Direct measurement of slip between steel and concrete. Technical report, University of Colorado, Boulder, 1984.

[124] B. K. Larson, L. T. Drzal, and P. Sorousian. Carbon fibre-cement adhesion in carbon fibre reinforced cement composites. *Construction and Building Materials*, 5(3):83–92, 1991. http://dx.doi.org/10.1016/0950-0618(91)90006-7.

[125] A. Lau and M. Anson. Effect of high temperatures on high performance steel fibre reinforced concrete. *Cement and Concrete Research*, 36:1698–1707, 2006. http://dx.doi.org/10.1016/j.cemconres.2006.03.024.

[126] C. P. Laurent, D. Durville, D. Mainard, J. F. Ganghoffer, and R. Rahouadj. A multilayer braided scaffold for Anterior Cruciate Ligament: mechanical modeling at the fiber scale. *Journal of the mechanical behavior of biomedical materials*, 12:184–96, Aug. 2012. http://dx.doi.org/10.1016/j.jmbbm.2012.03.005.

[127] S. Lettow and R. Eligehausen. The simulation of bond between concrete and reinforcement in nonlinear three-dimensional finite element analysis. *Civil Engineering*, pages 1–8, 2004.

[128] H. Lin, L. P. Brown, and A. C. Long. Modelling and simulating textile structures using texgen. In *Advances in Textile Engineering*, volume 331 of *Advanced*

Materials Research, pages 44–47. Trans Tech Publications, 10 2011. http://dx.doi.org/10.4028/www.scientific.net/AMR.331.44.

[129] H. Lippmann and J. Lemaitre. *A Course on Damage Mechanics*. Springer Berlin Heidelberg, 1996.

[130] A. Losberg and P. A. Olsson. Bond failure of deformed reinforcing bars based on the longitudinal splitting effect of the bars. *ACI Journal Proceedings*, 76(1), 1979. http://dx.doi.org/10.14359/6934.

[131] L. N. Lowes. A Concrete-Steel Bond Model For Use in finite Element Modeling of Reinforced Concrete Structures. *Special Publication*, 205, 2002. https://www.concrete.org/publications/internationalconcreteabstractsportal.aspx?m=details&ID=11643.

[132] L. N. Lowes, J. P. Moehle, and S. Govindjee. Concrete-Steel Bond Model for Use in Finite Element Modeling of Reinforced Concrete Structures. *ACI Journal*, 101(S50):501–511, 2004. http://dx.doi.org/10.14359/13336.

[133] C. Ltd. Fibre cement - rooted in history, 2008. [http://www.cembrit.co.uk/Fibre_cement-21715.aspx].

[134] L. A. Lutz and P. Gergely. Mechanics of bond and slip of deformed bars in concrete. *ACI Journal Proceedings*, 64(11):711–721, 1967. http://dx.doi.org/10.14359/7600.

[135] Z. I. Mahmoud. *Bond characteristics of fibre reinforced polymers prestressing reinforcement*. PhD thesis, Alexandria University, 1997.

[136] R. M. Mains. Measurement of the distribution of tensile and bond stresses along reinforcing bars. *American Concrete Institute*, 48(11):225–252, 1951. http://dx.doi.org/10.14359/11882.

[137] L. J. Malvar. Bond of reinforcement under controlled confinement. *Materials Journal*, 89(6):593–601, 1992. http://dx.doi.org/10.14359/4039.

[138] M. A. Mansur and T. Y. Lim. Torsional behaviour of reinforced fibre concrete beams, 1985. http://dx.doi.org/10.1016/0262-5075(85)90047-8.

[139] H. A. McKenna, J. W. S. Hearle, and N. O'Hear. *Handbook of Fibre Rope Technology*. Woodhead publishing in textiles. CRC Press, 2004.

[140] J. Melenk and I. BabuÅąka. The partition of unity finite element method: Basic theory and applications. *Computer Methods in Applied Mechanics and Engineering*, 139(1):289 – 314, 1996.

[141] C. A. Menzel. Some factors influencing results of pull-out bond tests. *ACI Journal Proceedings*, 35(6), 1939. http://dx.doi.org/10.14359/8507.

[142] C. Meyer. Dynamic finite element analysis of reinforced concrete structures. *IABSE reports of the working commissions*, 33:65–84, 1981. http://dx.doi.org/10.5169/seals-26264.

[143] N. Moës, J. Dolbow, and T. Belytschko. A finite element method for crack growth without remeshing. *Int. J. Numer. Meth. Engng*, 46(1):131–150, 1999. http://dx.doi.org/10.1002/(SICI)1097-0207(19990910)46:1<131::AID-NME726>3.0.CO;2-J.

[144] G. E. Monfore. A review of fiber reinforced Portland cement paste, mortar, and concrete. *Journal of Research Development Labs, Portland Cement Association*, 10(3):36–42, 1968.

[145] T. Mori, K. Saito, and T. Mura. An inclusion model for crack arrest in a composite reinforced by sliding fibers. *Mechanics of Materials*, 7:49–58, 1988. http://dx.doi.org/10.1016/0167-6636(88)90005-1.

[146] T. D. Mylrea. Bond and Anchorage. *American Concrete Institute*, 44(3):521–552, 1948. http://dx.doi.org/10.14359/12190.

[147] A. Naaman, S. Shah, and J. Throne. Some developments in polypropylene fibers for concrete. *American Concrete Institute*, SP-81:375–396, 1982.

[148] A. E. Naaman and H. Hammoud. Fatigue characteristics of high performance fiber-reinforced concrete. *Cement and Concrete Composites*, 20:353–363, 1998. http://dx.doi.org/10.1016/S0958-9465(98)00004-3.

[149] D. Ngo and A. C. Scordelis. Finite Element Analysis of Reinforced Concrete Beams. *ACI Journal Proceedings*, 64(3):152–163, 1967. http://dx.doi.org/10.14359/7551.

[150] A. H. Nilson. Nonlinear analysis of reinforced concrete by the finite element method. *ACI Journal*, 65(9):757–766, 1968. http://dx.doi.org/10.14359/7510.

[151] A. H. Nilson. Internal measurements of bond slip. *ACI Journal*, 69:439–441, 1972. http://dx.doi.org/10.14359/7170.

[152] T. Ohta, R. Djamaluddin, S. Hino, K. Yamaguchi, and K. Harada. Flexural properties of concrete beams reinforced with UCAS. *Journal of Structural Engineering*, 48A:1229–1238, 2002.

[153] T. Ohta, R. Djamaluddin, S. T. Seo, T. Sajima, and K. Harada. Evaluation of tensile strength of Unresin Continuous Carbon Fiber cables as tensile reinforcement for concrete structures. *Memoirs of the Faculty of Engineering, Kyushu University*, 62(4):179–190, 2002.

[154] T. Okamoto, S. Matsubara, M. Tanigaki, and K. Hasuo. Long-term loading test on PPC beams using braided frp rods. In *Fibre Reinforced Cement and Concrete, Proceedings of the Fourth RILEM International Symposium*, pages 1000–1014, Sheffield, 1992. E & FN Spon.

[155] J. OLIVER. Modelling strong discontinuities in solid mechanics via strain softening constitutive equations. part 1: Fundementals. *International Journal for Numerical Methods in Engineering*, 39(21):3575–3600, 1996. http://dx.doi.org/10.1002/(SICI)1097-0207(19961115)39:21<3575::AID-NME65>3.0.CO;2-E.

[156] L. Ombres and S. Verre. Structural behaviour of fabric reinforced cementitious matrix (FRCM) strengthened concrete columns under eccentric loading. *Composites Part B: Engineering*, 75:235–249, 2015. http://dx.doi.org/10.1016/j.compositesb.2015.01.042.

[157] J. Ožbolt, S. Lettow, and I. Kožar. Discrete bond element for 3d finite element analysis of reinforced concrete structures. In *Proceedings of the 3rd International Symposium: Bond in Concrete-from research to standards. Budapest: University of Technology and Economics*, page 4, 2002.

[158] S. H. Park, D. J. Kim, G. S. Ryu, and K. T. Koh. Tensile behavior of ultra high performance hybrid fiber reinforced concrete. *Cement and Concrete Composites*, 34(2):172–184, 2012. http://dx.doi.org/10.1016/j.cemconcomp.2011.09.009.

[159] A. Peled. Textiles as reinforcements for cement composites under Iimpact loading. In H. Reinhardt and A. Naaman, editors, *High Performance Fiber Reinforced Cement Composites - HPFRCC 5*, pages 455–462, Cachan, France, 2007. RILEM Proceedings.

[160] A. Poursaee and C. M. Hansson. The influence of longitudinal cracks on the corrosion protection afforded reinforcing steel in high performance concrete. *Cement and Concrete Research*, 38:1098–1105, 2008. http://dx.doi.org/10.1016/j.cemconres.2008.03.018.

[161] G. Promis, A. Gabor, G. Maddaluno, and P. Hamelin. Behaviour of beams made in textile reinforced mineral matrix composites, an experimental study. *Composite Structures*, 92(10):2565–2572, 2010. http://dx.doi.org/10.1016/j.compstruct.2010.02.003.

[162] J. A. Purkiss. Steel fibre reinforced concrete at elevated temperatures. *International Journal of Cement Composites and Lightweight Concrete*, 6(3):179–184, 1984. http://dx.doi.org/10.1016/0262-5075(84)90006-X.

[163] Y. R. Rashid. Ultimate strength analysis of prestressed concrete pressure vessels. *Nuclear Engineering and Design*, 7:334–344, 1968. http://dx.doi.org/10.1016/0029-5493(68)90066-6.

[164] G. Rehm. *Über die Grundlagen des Verbundes zwischen Stahl und Beton*. Deutscher Ausschuss für Stahlbeton. Vertrieb durch Verlag von W. Ernst, 1961.

[165] M. Richter and B. W. Zastrau. Behaviour of fiber reinforced concrete columns in fire. *Materials Science and Engineering A*, 92(5):1263–1268, 2010. http://dx.doi.org/10.1016/j.msea.2006.02.007.

[166] T. C. RILEM. *RILEM Recommendations for the Testing and Use of Constructions Materials*. 1994. http://dx.doi.org/10.1617/2351580117.080.

[167] P. Robinson and D. Q. Song. A Modified DCB Specimen for Mode I Testing of Multidirectional Laminates. *Journal of Composite Materials*, 26(11):1554–1577, Jan. 1992. http://dx.doi.org/10.1177/002199839202601101.

[168] J. P. C. Rodrigues, L. Laím, and A. M. Correia. Behaviour of fiber reinforced concrete columns in fire. *Composite Structures*, 92(5):1263–1268, 2010. http://dx.doi.org/10.1016/j.compstruct.2009.10.029.

[169] J. P. Romualdi and G. B. Batson. Mechanics of crack arrest in concrete. *Journal of Engineering Mechanics Division, ASCE*, 89(EM3):147–168, 1963.

[170] J. G. Rots. Analysis of crack propagation and fracture of concrete with DIANA, Report No. BI-83-26. Technical report, Insitute TNO for Building Materials and Building Structures, Rijswijk, The Netherlands, 1983.

[171] J. G. Rots. Prediction of dominant cracks using the smeared crack concept, Report No. BI-83-39. Technical report, Insitute TNO for Building Materials and Building Structures, Rijswijk, The Netherlands, 1983.

[172] J. G. Rots. Variabele reductiefactor voor de schuifweerstand van gescheurd beton, Report No. BI-84-33. Technical report, Insitute TNO for Building Materials and Building Structures, Rijswijk, The Netherlands, 1984.

[173] J. G. Rots. *Computational modeling of concrete frature.* PhD thesis, Delft University of Technology, 1988.

[174] J. G. Rots and R. de Borst. Analysis of mixed-mode fracture in concrete. *Journal of engineering mechanics*, 1987. http://dx.doi.org/10.1061/(ASCE)0733-9399(1987)113:11(1739).

[175] J. G. Rots, P. Nauta, G. M. A. Kusters, and J. Blaauwendraad. Smeared crack approach and fracture localization in concrete. *Heron Journal*, 30(1), 1985.

[176] Sandia Corporation. *Cubit 13.0 User Documentation.* Sandia National Laboratories, New Mexico, United States, 2011.

[177] B. V. Sankar and R. V. Marrey. A unit-cell model of textile composite beams for predicting stiffness properties. *Composites Science and Technology*, 49(1):61–69, jan 1993. http://dx.doi.org/10.1016/0266-3538(93)90022-9.

[178] J. C. J. Schellekens and R. de Borst. On the numerical integration of interface elements. *International Journal for Numerical Methods in Engineering*, 36(1):43–66, Jan. 1993. http://dx.doi.org/10.1002/nme.1620360104.

[179] F. Schladitz, M. Frenzel, D. Ehlig, and M. Curbach. Bending load capacity of reinforced concrete slabs strengthened with textile reinforced concrete. *Engineering Structures*, 40:317–326, 2012. http://dx.doi.org/10.1016/j.engstruct.2012.02.029.

[180] W. C. Schnobrich. Behavior of reinforced concrete structures predicted by the finite element method. *Computers & Structures*, 7:365–376, 1977. http://dx.doi.org/10.1016/0045-7949(77)90074-8.

[181] A. C. Scordelis. Computer models for nonlinear analysis of reinforced and prestressed concrete structures. *PCI Journal*, 29(6):116–135, 1984. http://dx.doi.org/10.15554/pcij.11011984.116.135.

[182] A. C. Scordelis, D. Ngo, and H. A. Franklin. Finite element study of reinforced concrete beams with diagonal tension cracks. *International Concrete Abstracts Portal*, 42:79–102, 1974.

[183] J. Segurado and J. LLorca. A new three-dimensional interface finite element to simulate fracture in composites. *International Journal of Solids and Structures*, 41(11-12):2977–2993, June 2004. http://dx.doi.org/10.1016/j.ijsolstr.2004.01.007.

[184] S. T. Seo and R. Djamaluddin. Experimental studies on bond capacity of grid system for UCCF cables. *KSCE Journal of Civil Engineering*, 10(1):15–19, Jan. 2006. http://dx.doi.org/10.1007/BF02829300.

[185] R. Serpieri and G. Alfano. Bond-slip analysis via a thermodynamically consistent interface model combining interlocking, damage and friction. *International Journal for Numerical Methods in Engineering*, 85(2):164–186, Jan. 2011. http://dx.doi.org/10.1002/nme.2961.

[186] R. Serpieri, L. Varricchio, E. Sacco, and G. Alfano. Bond-slip analysis via a cohesive-zone model simulating damage, friction and interlocking. *Frattura ed Integrita Strutturale*, 8(29):284–292, 2014. http://dx.doi.org/10.3221/IGF-ESIS.29.24.

[187] Z. Q. Shi and D. D. L. Chung. Improving the abrasion resistance of mortar by adding latex and carbon fibers. *Cement and Concrete Research*, 27(8):1149–1153, 1997. http://dx.doi.org/10.1016/s0008-8846(97)00097-5.

[188] A. Si Larbi, A. Agbossou, and P. Hamelin. Experimental and numerical investigations about textile-reinforced concrete and hybrid solutions for repairing and/or strengthening reinforced concrete beams. *Composite Structures*, 99:152–162, 2013. http://dx.doi.org/10.1016/j.compstruct.2012.12.005.

[189] A. Si Larbi, R. Contamine, E. Ferrier, and P. Hamelin. Shear strengthening of RC beams with textile reinforced concrete (TRC) plate. *Construction and Building Materials*, 24(10):1928–1936, 2010. http://dx.doi.org/10.1016/j.conbuildmat.2010.04.008.

[190] C. Sibagropromstroy. Проектнаја декларација на строителство жилого дома 4 от 24.05.2012 г. ONLINE, May 2012. [http://www.saps.ru/upload/files/pd_dom4.doc].

[191] K. K. Sideris, P. Manita, and E. Chaniotakis. Performance of thermally damaged fibre reinforced concretes. *Construction and Building Materials*, 23(3):1232–1239, 2009. http://dx.doi.org/10.1016/j.conbuildmat.2008.08.009.

[192] P. Solin, K. Segeth, and I. Dolezel. *Higher-order finite element methods*. Studies in Advanced Mathematics. Taylor & Francis, 2003.

[193] S. Somayaji and S. P. Shah. Bond stress versus slip relationship and cracking response of tension members. *ACI Journal Proceedings*, 78(20):217–225, May 1981. http://dx.doi.org/10.14359/6920.

[194] S. Soretz and H. Holzenbein. Influence of rib dimensions of reinforcing bars on bond and bendability. *Journal Proceedings*, 76(1), Jan. 1979. http://dx.doi.org/10.14359/6939.

[195] R. M. E. Sousa Fangueiro, C. Gonilho-Pereira, S. Jalali, and M. de Araújo. The mechanical properties of braided reinforced composites for application in concrete structures. In *37th International Symposium on novelties in Textiles*, number June, Ljubljana, Slovenia, 2006.

[196] M. Stolarska, D. l. Chopp, N. Moës, and T. Belytschko. Modelling crack growth by level sets in the extended finite element method. *International Journal for Numerical Methods in Engineering*, 51(8):943–960, 2001. http://dx.doi.org/10.1002/nme.201.

[197] F. Stoll, J. Saliba, and L. Casper. Experimental study of CFRP-prestressed high-strength concrete bridge beams. *Composite Structures*, 49(2):191–200, 2000. http://dx.doi.org/10.1016/S0263-8223(99)00134-8.

[198] M. Suidan and W. C. Schnobrich. Finite element analysis of reinforced concrete. *Journal of Structural Division, ASCE*, 99(10):2109–2122, 1973.

[199] P. Sukontasukkul, W. Pomchiengpin, and S. Songpiriyakij. Post-crack (or post-peak) flexural response and toughness of fiber reinforced concrete after exposure to high temperature. *Construction and Building Materials*, 24(10):1967–1974, 2010. http://dx.doi.org/10.1016/j.conbuildmat.2010.04.003.

[200] D. V. Swenson and A. R. Ingraffea. Modeling mixed-mode dynamic crack propagation nsing finite elements: Theory and applications. *Computational Mechanics*, 3(6):381–397, sep 1988. http://link.springer.com/10.1007/BF00301139.

[201] Z. S. Tabatabaei, J. S. Volz, J. Baird, B. P. Gliha, and D. I. Keener. Experimental and numerical analyses of long carbon fiber reinforced concrete panels exposed to blast loading. *International Journal of Impact Engineering*, 57:70–80, 2013. http://dx.doi.org/10.1016/j.ijimpeng.2013.01.006.

[202] H. Tanyildizi. Effect of temperature, carbon fibers, and silica fume on the mechanical properties of lightweight concretes. *New Carbon Materials*, 23(4):339–344, 2008. http://dx.doi.org/10.1016/S1872-5805(09)60005-6.

[203] T. J. Tautges. Canonical numbering systems for finite-element codes. *International Journal for Numerical Methods in Biomedical Engineering*, Mar. 2010. http://dx.doi.org/10.1002/cnm.1237.

[204] T. J. Tautges, R. Meyers, K. Merkley, C. Stimpson, and C. Ernst. MOAB: a mesh-oriented database. SAND2004-1592, Sandia National Laboratories, Apr. 2004. Report.

[205] ИТАР-ТАСС. Причиной пожара в 25- этажном доме в Красноярске могли стат сварочные работы , 2014. [http://itar-tass.com/sibir-news/1458401 posted 22-September-2014].

[206] Новости Мира. Восстановление поврежденной от пожара высотки в Красноярске оценили в 52 млн рублей, Oct. 2014.

[207] P. Tjiptobroto and W. Hansen. Mechanism for tensile strain hardening in high performance cement-based fiber reinforced composites. *Cement and Concrete Composites*, 13(1991):265–273, 1991. http://dx.doi.org/10.1016/0958-9465(91)90032-D.

[208] L. Tong and A. P. Mouritz. *3D Fibre reinforced polymer composites*. Elsevier Science, 2002.

[209] H. A. Toutanji, T. El-Korchi, and R. N. Katz. Strength and reliability of carbon-fiber-reinforced cement composites. *Cement and Concrete Composites*, 16:15–21, 1994. http://dx.doi.org/10.1016/0958-9465(94)90026-4.

[210] Z. Ullah, L. Kaczmarczyk, and C. J. Pearce. Multiscale computational homogenisation to predict the long-term durability of composite structures. In *23rd UK Conference of the Association for Computational Mechanics in Engineering*, number April, pages 8–11, 2015.

[211] V. V. Vasiliev and E. Morozov. *Advanced Mechanics of Composite Materials*. Elsevier Science, 2007.

[212] I. Verpoest and S. V. Lomov. Virtual textile composites software : Integration with micro-mechanical, permeability and structural analysis. *Composites Science and Technology*, 65(15-16):2563–2574, dec 2005. http://dx.doi.org/10.1016/j.compscitech.2005.05.031.

[213] J. Vignollet, S. May, and R. de Borst. On the numerical integration of isogeometric interface elements. *International Journal for Numerical Methods in Engineering*, 2015. http://dx.doi.org/10.1002/nme.4867.

[214] S. Viwathanatepa, E. P. Popov, and V. V. Bertero. Effects of generalized loading on bond of reinforced bars embedded in confined concrete blocks. Technical report, College of Engineering, University of California, Berkeley, California, 1979.

[215] T. D. Vu, D. Durville, and P. Davies. Finite element simulation of the mechanical behavior of synthetic braided ropes and validation on a tensile test. *International Journal of Solids and Structures*, 58(April):106–116, 2015. http://dx.doi.org/10.1016/j.ijsolstr.2014.12.022.

[216] G. Wells and L. Sluys. A new method for modelling cohesive cracks using finite elements. *International Journal for Numerical Methods in Engineering*, 50(12):2667–2682, 2001. http://dx.doi.org/10.1002/nme.143.

[217] J. Whitcomb, K. Srirengan, and C. Chapman. Evaluation of homogenization for global/local stress analysis of textile composites. *Composite Structures*, 31(2):137–149, jan 1995. http://dx.doi.org/10.1016/0263-8223(95)00011-9.

[218] J. Whitcomb and K. Woo. Enhanced direct stiffness method for finite element analysis of textile composites. *Composite Structures*, 28(4):385–390, jan 1994. http://dx.doi.org/10.1016/0263-8223(94)90120-1.

[219] Wikipedia. Carbon (fiber), 2015. [http://en.wikipedia.org/wiki/Carbon_%28fiber%29#Structure_and_properties accessed 28 March 2015].

[220] J. Z. Zemajtis. Role of Concrete Curing. [http://www.cement.org/for-concrete-books-learning/concrete-technology/concrete-construction/curing-in-construction accessed 15 February 2014].

[221] Q. Zheng and D. D. L. Chung. Carbon fiber reinforced cement composites improved by using chemical agents. *Cement and Concrete Research*, 19:25–41, 1989. http://dx.doi.org/10.1016/0008-8846(89)90062-8.